THE UNIVERSITY OF CHICAGO

ILLUMINATING THE ORIGINS OF PLANETS WITH SOLAR TWINS

A DISSERTATION SUBMITTED TO
THE FACULTY OF THE DIVISION OF THE PHYSICAL SCIENCES
IN CANDIDACY FOR THE DEGREE OF
DOCTOR OF PHILOSOPHY

DEPARTMENT OF ASTRONOMY AND ASTROPHYSICS

BY
MEGAN ELIZABETH BEDELL

CHICAGO, ILLINOIS
AUGUST 2017

“We can judge our progress by the courage of our questions and the depth of our answers, our willingness to embrace what is true rather than what feels good.”

— Carl Sagan

TABLE OF CONTENTS

I HUNTING FOR PLANETS AROUND SOLAR TWINS

II PRECISE STELLAR ABUNDANCES WITH SOLAR TWINS

LIST OF FIGURES

LIST OF TABLES

ACKNOWLEDGMENTS

Thanks first and foremost to my family for your endless love and support. I wouldn't be here without you.

Thanks to my advisor, Jacob Bean, for helping me see the opportunity in every challenge. I deeply appreciate your encouragement, your wisdom, and your excellent fashion sense.

Thanks also to my unofficial second advisor, Jorge Meléndez, for teaching me everything I know about equivalent widths. Without your tireless support I would be a much poorer spectroscopist (and I'd still be struggling to install MOOG).

I've been incredibly fortunate to have a grad school career full of laughter, friendship, and international travel. Thanks to Andreas, Kevin, Julian, Diana, Ben, Laura, Hannah, Lily, Adam, Greg, Leo, Megan M., and Emily for making the Bean Team such a fun place to be. Thanks also to my cohort for many mind-expanding discussions and to the scotch hour crew for always keeping my spirits up. And thanks to my partners in astronomy adventures around the world, including Simona, Judit, Steph, Marcelo, Maria, Johanna, Szymon, Paolo, and so many more. See you on the next mountaintop!

To Scotia, Winni, and Lucy: thanks for being my most loyal supporters. You're good dogs.

I gratefully acknowledge the financial backing of the National Science Foundation, the Josephine De Karman Fellowship Trust, the American Philosophical Society, the NASA Astrobiology Institute, the Illinois Space Grant Consortium, and the University of Chicago Division of the Physical Sciences.

Last but certainly not least, I am indebted to ESO and the HARPS team for building and maintaining a world-class instrument for radial velocity planet hunting. The work in this thesis is built upon decades of ground-breaking engineering efforts, without which none of this science would have been possible. Thank you to Oscar Orrego and the observatory staff for making La Silla my home halfway around the world. And thanks, Switzerland, for all the fondue.

ABSTRACT

In this dissertation we present the results of a five-year-long radial velocity planet search and a companion survey of detailed stellar abundances. The Solar Twin Planet Search is a uniquely designed observing program on the HARPS spectrograph that aims to characterize the planetary systems of 68 solar twin stars. As we demonstrate in this work, solar twins' chemical compositions can be spectroscopically determined at an unparalleled level of detail. My thesis pairs these precise stellar abundances with information about the stars' planetary systems to give new insights into the connection between stars and the planets they form.

Knowledge of stellar composition can give a glimpse into the history of planetary systems. In the HIP 11915 system, we have discovered a planet of comparable mass and orbital period to Jupiter around a star with an abundance pattern indistinguishable from the Sun's. The HIP 68468 system, on the other hand, is vastly different from our own, with two close-in planetary companions and a stellar composition that could indicate past accretion of planetary material onto the host star. In addition to these planets discovered through our Solar Twin Planet Search, we also present a new analysis of Kepler-11, whose six planets are widely regarded as the archetypal "puffy" close-in exoplanets. Contrary to previous studies, we identify Kepler-11 as a solar twin. The revised stellar properties and new analysis raise the Kepler-11 planet densities by between 20-95% per planet.

These individual systems demonstrate the power of combining stellar characterization with planet detections. The true potential of the Solar Twin Planet Search goes beyond single systems to characterize a statistically significant population of solar twins. We present photospheric abundance measurements of 17 elements in 80 solar twins using co-added HARPS spectra for precisions on order 0.01 dex ($\sim$ 2%). From this large sample of solar twins, we investigate the dependence of stellar composition on age and other characteristics. We present unprecedentedly precise galactic chemical evolution trends. We also find a much smaller dispersion in the C/O and Mg/Si abundance ratios than previously reported in non-twin-star studies and discuss the implications of this result on the compositional diversity of planets throughout the galaxy.

Finally, we demonstrate that the Sun is depleted in refractory materials relative to 92% of solar twins, hinting at an atypical history of dust condensation in the solar system. While the cause of this trend is not definitively determined, we conclude with a vision of future studies which will shed further light on the connections between detailed stellar compositions and planets.

CHAPTER 1

INTRODUCTION

Although the study of extrasolar planets is a relative newcomer to the scene of astrophysics research, beginning only in 1995 with the discovery of 51 Pegasi b, the progress made in the past 22 years is truly remarkable (Mayor & Queloz, 1995). At the time of writing this thesis, 3,499 confirmed exoplanets are known,[1] with thousands more anticipated from current and near-future missions including ESA's *Gaia* and NASA's *Transiting Exoplanet Survey Satellite (TESS)* (Perryman et al., 2014; Sullivan et al., 2015).

As the sample of exoplanets expands, a few overarching trends have emerged through statistics and have enriched our understanding of planetary systems. Unanticipated classes of planets have emerged, including hot Jupiters and super-Earths, which have no analogs in our Solar System and indicate a great diversity in the outcomes of planet formation processes. The abundance of multi-planet systems in resonant configurations has hinted at migration playing an important role in shaping the planetary systems that we see today (e.g. Mills et al., 2016). The high occurrence rate of small planets around low-mass stars has significantly altered our outlook on planet habitability and the search for "Earth 2.0" (e.g. Dressing & Charbonneau, 2013; Mulders et al., 2015).

One pivotal insight from the past decades of exoplanet studies has often been summed up with a pithy phrase: "know thy star, know thy planet." Understanding the stars that host planets helps us understand the planets themselves in more ways than one.

First and foremost, the vast majority of exoplanets have been discovered through indirect techniques, where the planet itself is never seen. Its presence is inferred through changes in the apparent brightness or motion of its host star. As a result, the measured properties of the planet depend on the host star's assumed properties. The most extreme example of this is in the transit technique: the measured transit depth is determined by the ratio of the projected stellar and planetary surface areas. The radii of the two bodies therefore depend

---

[1] from `http://exoplanetarchive.ipac.caltech.edu/`

linearly on each other. If the assumed stellar radius is incorrect, the inferred planet radius will be equally affected. As I demonstrate in Chapter 7, this dependence on stellar properties becomes even more critical in the case of systems with transiting time variations (TTVs).

Planets discovered through the radial velocity (RV) technique have a weaker dependence on the host star properties: the inferred minimum mass of the planet scales roughly as $M_\star^{2/3}$. Another aspect of the star-planet connection plays a large role in RV planet searches, though. When looking for time-variable behavior of a star as a sign of planets around it, we must necessarily also understand how the star varies in time as a result of its own internal physics. A star's apparent radial velocity changes due to many factors, including the evolution of convective features, seismic oscillations, and irregular flaring events, but the most widely studied effect is that of starspots and similar magnetic surface features like plages, commonly referred to under the umbrella term of "activity."

While an exhaustive review of stellar activity and its effects on planet searches is beyond the scope of this work, it remains one of the chief roadblocks to the discovery of small planets with the radial velocity technique, and has considerable consequences for transiting planet detection as well. The greater our understanding of the observational signatures of stellar activity, the better we will be able to pull planet signals out of the activity-dominated noise. In particular, knowledge of the stellar rotation period allows us to more effectively account for the effects of surface features like starspots (e.g. Saar & Donahue, 1997; Robertson et al., 2014; Dumusque et al., 2014). On multi-year timescales, the stellar activity cycle is a critical component of the RV behavior which can mimic the presence of Jupiter-like planets (e.g. Saar & Fischer, 2000; Lovis et al., 2011; Wright, 2016). I explore the challenges of finding planets in the presence of stellar activity in Chapters 2 and 3, and I delve deeper into the characteristic activity patterns of our solar twin sample in Chapter 4.

Last but certainly not least, the study of planet host stars can reveal extra information about the formation process and possible bulk compositions of the planets themselves. This is information that cannot be obtained in any other way for the majority of known exoplanets.

Because stars and planets form side-by-side from the same primordial nebula, we can think of the star itself as a "fossil record" of the composition of the planet-forming disk. This is most clearly illustrated in the well-known giant planet–metallicity relation, where stars with higher metallicities have been found to host close-in gas giant planets at a higher occurrence rate (Gonzalez, 1997; Fischer & Valenti, 2005). This result has been widely interpreted as evidence for the core-accretion model of planet formation: systems with high primordial levels of metals will be able to form metallic planet cores more rapidly. These cores will have time to accrete substantial amounts of gas before the planet-forming disk dissipates, thereby creating gas giant planets around these metal-rich stars. The core-accretion interpretation also predicts that a metallicity dependence should not exist for the occurrence rate of smaller planets, a result which is debatably seen in the Kepler small-planet sample (see e.g. Buchhave et al., 2012; Mulders et al., 2016).

The iron abundance or metallicity of a star is the easiest aspect of its composition to measure due to the profusion of strong, unblended iron absorption lines in the spectrum of an FGK star. The discovery of a link between this fundamental property of a star and its planetary system is exciting and informative, but it also provides encouragement to go further. Dozens of other elements also produce measurable spectral absorption features, and the question of how these elements may link with planets is a compelling one. The Mg/Si, and Si/Fe ratios of host stars are regarded as especially useful diagnostics of their planets' compositions, as they govern the compounds which make up the planet interiors (see e.g. Sotin et al., 2007; Carter-Bond et al., 2012). In the case of a transiting planet with a detectable atmosphere, the C/O ratio becomes important, as it may even be possible to draw information about the planet's location and time of formation by comparing the planetary C/O with that of its host star (e.g. Madhusudhan, 2012).

The preceding examples rely on using a star's photospheric composition as a direct proxy for the composition of the disk from which planets formed. It is also possible, however, that the star's present-day composition has been altered from its primordial state as a consequence of planet formation. From theoretical models and from solar system observations like age-dating of the calcium-aluminum-rich inclusions in meteorites, it appears that gas giant and planetesimal formation proceed rapidly within a couple Myr of the star's birth (Roberge & Kamp, 2010, and references therein). Meanwhile, massive disks of gas and dust remain around sun-like stars for ∼2-10 Myr (e.g. Mamajek, 2009; Pfalzner et al., 2014). Some portion of this disk is accreted onto the star, potentially carrying with it signatures of the planets that formed from it during the earliest stages of the system's life.

One proposed observable marker of past planet formation is a depletion in the photospheric lithium abundance (King et al., 1997). While lithium is naturally consumed over the main-sequence lifetime of Sun-like stars, its depletion can be accelerated by an enhancement in the differential rotation between the star's radiative core and convective envelope Bouvier (2008). If star-disk interactions during the planet formation process slow the surface rotation of the star, we would expect to see a systematically lower lithium abundance in planet-hosting stars. Several authors have found such a trend in samples of hundreds of stars with and without planets (Israelian et al., 2009; Gonzalez et al., 2010a; Delgado Mena et al., 2014; Figueira et al., 2014). Others, however, find that this trend is no longer present after accounting for stellar age and other systematic effects (Baumann et al., 2010; Ghezzi et al., 2010; Ramírez et al., 2012a). The reality of this lithium-planet connection remains under debate.

Another potential signature of planet formation is a characteristic trend in chemical abundances with condensation temperature ($T_{\rm C}$). Rocky materials like the Earth and the chondritic meteorites display an elemental abundance pattern that correlates with the temperature at which those elements condense under the typical temperature-pressure conditions of a protoplanetary disk (Lodders, 2003). We might expect to see such patterns in the photospheric abundances of host stars, either as a result of late-stage planet engulfment (resulting in a photospheric overabundance of refractory materials) or from the preferential cleansing of rocky materials from the system as they become locked up in planetesimals (resulting in a deficit of refractory materials in the accreted outer layers of the star). Early works did not find such trends (Gonzalez, 1997). With advances in spectroscopic techniques and in planet-finding, though, T_C-dependent patterns began to emerge. Meléndez et al. (2009) were the first to find a plausible connection between T_C trends and planets when they showed that the Sun is refractory-poor relative to eleven solar twins. As with the planet-lithium connection, this result has been hotly debated, with some studies finding that planet-hosting stars have negative abundance-T_C trends like the Sun (e.g. Ramírez et al., 2009; Gonzalez et al., 2010b) and others refuting this result (e.g. González Hernández et al., 2010; Schuler et al., 2015).

In any of these cases, the imprint of planets on their host stars is likely to be quite small. The solar T_C trend found by Meléndez et al. (2009) corresponds to a depletion of just 4 Earth masses of rocky material within the vast solar convective envelope (Chambers, 2010). It is little wonder that detections of such tiny signals are controversial in the literature. To maximize our chances of successfully resolving these planet signatures, we turn to a specific class of stars: solar twins.

1.1 The Power of Solar Twins

When inferring photospheric abundances from an observed stellar spectrum, one must rely at some level on theoretical models of the stellar atmosphere. Absorption lines are shaped not only by the underlying abundances but also by the temperature and pressure conditions under which the atoms and molecules undergo their transitions, and by perturbing factors like local turbulence and magnetic features (for an in-depth overview of these effects, see Gray, 2005). For this reason, our ability to accurately extract abundances is only as good as our models of the physics within the stellar photosphere.

There is plenty of reason to believe that current models of stellar atmospheres are flawed. The model grids used in most FGK dwarf analyses use unrealistic approximations like one-dimensionality and perfect local thermal equilibrium (e.g. Castelli & Kurucz, 2004; Gustafs-

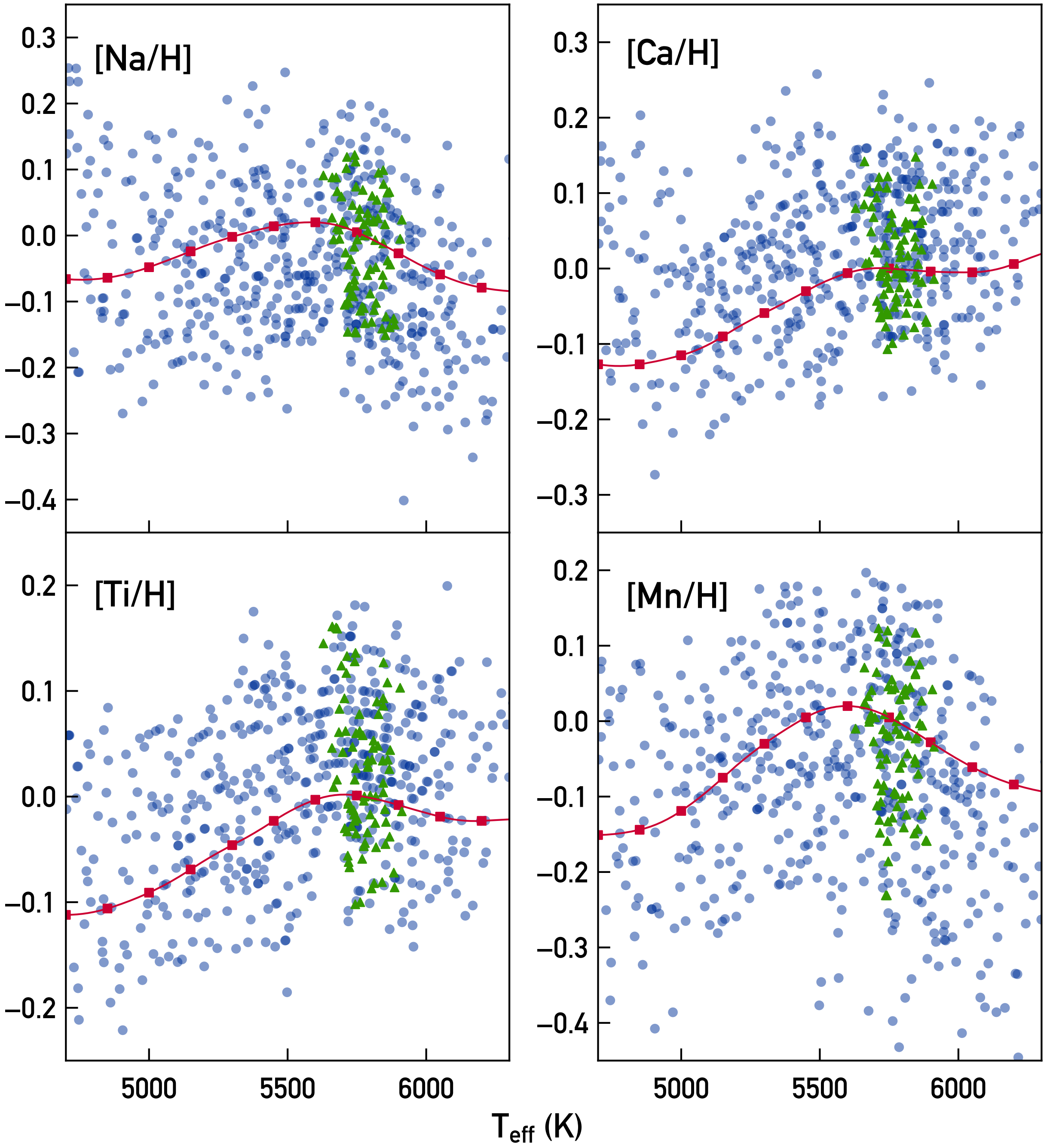

Figure 1.1 Model-induced systematic abundance errors as a function of stellar temperature in the Brewer et al. (2016) sample. Uncorrected abundances from Brewer et al. (2016) for stars with approximately solar $\log g$ and [Fe/H] are shown as blue circles. The systematic corrections applied by Brewer et al. (2016) are overplotted as red squares with quadratic interpolation. Results from solar twins in this work (Chapter 6) are plotted as green triangles. By restricting our sample to a narrow range of $T_{\rm eff}$, $\log g$, and [Fe/H], we minimize the systematic offsets introduced by the use of a wide range of stellar model atmospheres.

son et al., 2008). It is estimated that these limitations lead to abundance errors on the order of 0.3 dex (a factor of ~2) or more (Asplund, 2005).

To some extent, the dependence on theoretical models can be mitigated by measuring abundances of a target star differentially with respect to a reference star, often taken to be the Sun. If the target star and reference star use the same model atmosphere, the abundance errors introduced by the model will cancel out, resulting in limited *accuracy* but high differential *precision*. However, as the two stars become more physically dissimilar, errors are introduced. Abundance studies of large samples of host stars show this effect in the form of systematic abundance trends with stellar parameters (e.g. Valenti & Fischer, 2005; Sousa et al., 2011; Brewer et al., 2016). Figure 1.1 illustrates these systematic errors in Sun-like stars from the Brewer et al. (2016) sample.

In theory, then, the best possible precision should be achieved by a *strictly differential* analysis of the Sun and another star that shares the same fundamental parameters (temperature $T_{\rm eff}$, surface gravity $\log g$, metallicity [Fe/H], and microturbulence v_t). In Chapter 5 I demonstrate that we can indeed obtain abundance measurements to 0.01 dex (~2%) precision with this method given sufficiently high-quality spectra and line lists.

This differential twin-star technique was used by Meléndez et al. (2009) to uncover the previously discussed small-scale $T_{\rm C}$ trend in the solar abundance pattern. The comparison sample used consisted solely of solar twins, defined in this work as stars with $\Delta T_{\rm eff} < 100$ K, $\Delta\log g < 0.1$ dex, and Δ[Fe/H]< 0.1 dex of the Sun.

In the pioneering work of Meléndez et al. (2009), the rarity of the solar abundance pattern compared to its twins was suggested to be a result of the Sun's history of rocky planet formation. This conclusion was limited chiefly by our lack of knowledge about the other solar twins' planetary systems (or lack thereof). What planet formation or ingestion events may have shaped these other stars' photospheric abundances? This question was the main driver behind the RV planet search program reported in this thesis.

1.2 The Solar Twin Planet Search Program

Our RV program, dubbed the "Solar Twin Planet Search," consisted of 100 nights of observations using the High Accuracy Radial velocity Planet Searcher (HARPS) instrument located at ESO's La Silla Observatory (Mayor et al., 2003). HARPS is an echelle spectrograph with very high resolving power (R=115,000) and extreme environmental stability designed for the express purpose of obtaining precise radial velocities of bright stars. It has been in continuous operation since 2003 and has demonstrated long-term RV stability at the level of 80 cm s^{-1} (Lo Curto et al., 2010). The instrument utilizes the simultaneous reference method of RVs, meaning that for every stellar spectrum observed, a spectrum from a reference source (typically a ThAr lamp) is simultaneously taken. The RVs of star and reference are both extracted through cross-correlation with a quasi-binary mask (Baranne et al., 1979; Lovis & Pepe, 2007). The effective RV drift of the reference source is then subtracted from the stellar RV to compensate for short-term instrumental changes. Since HARPS is so well-stabilized, this drift is typically at or below the 1 m s^{-1} level.

Stars for this program were selected from a variety of sources including color-based dedicated solar twin searches (Meléndez et al., 2007; Ramírez et al., 2009; Meléndez et al., 2009) as well as solar twins identified in publicly available spectral databases (Valenti & Fischer, 2005; Baumann et al., 2010; Bensby et al., 2014). From this pool of likely twins, we selected the stars with relatively low activity levels ($\log(R'_{HK}) \leq -4.5$) which were not being observed as part of any other ongoing HARPS campaign. The resulting sample consisted of approximately 70 bright, nearby stars.

The on-sky distribution of STPS targets is shown in Figure 1.2. As expected for a sample of solar neighborhood stars, there is no apparent correlation between metallicity and projected distance from the galactic disk. We can therefore consider the compositions and planetary systems of these stars to be a typical representation of the local stellar population.

After our HARPS survey commenced, we did measure the precise fundamental properties of the full sample using first MIKE spectra (Ramírez et al., 2011) and later stacked HARPS

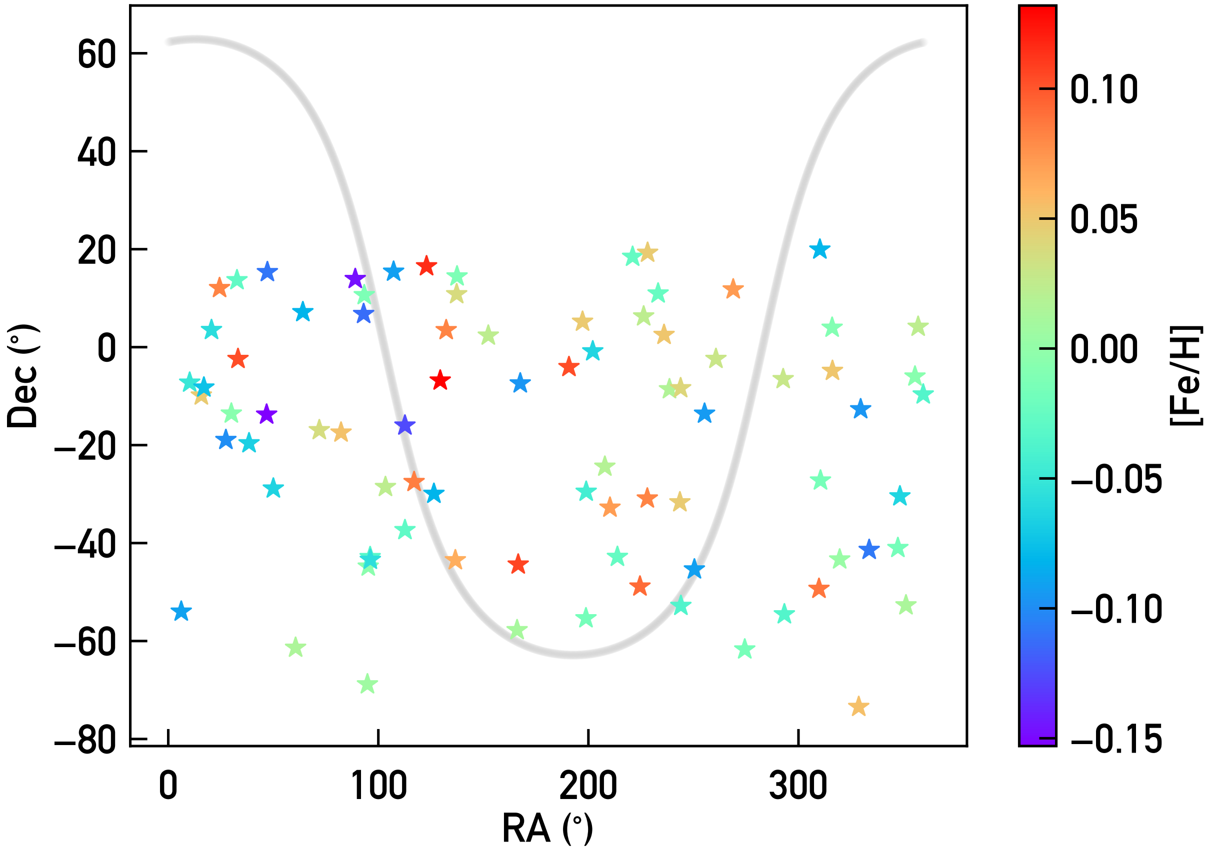

Figure 1.2 Solar twins from the abundance analysis sample plotted on sky. The grey line corresponds to the galactic plane.

spectra (see Chapter 6). The resulting parameters have a slightly broader distribution than our narrow definition of "solar twin," but all are within "solar analog" territory and are expected to yield relatively precise abundance measurements (Figure 1.3). An especially interesting feature of the sample distribution is the wide variety of stellar ages represented. This strength of our sample allows us to probe the effects of age on abundances, planets, and stellar activity within a small bin of metallicity space.

Generally speaking, we made an effort to observe all targets equally with our program time. Each RV observation consisted of one or more exposures (depending on target brightness) totaling 15-20 minutes. A minimum threshold of 15 minutes was required to average over multiple cycles of the asteroseismic p-mode oscillations, which have a typical cycle period

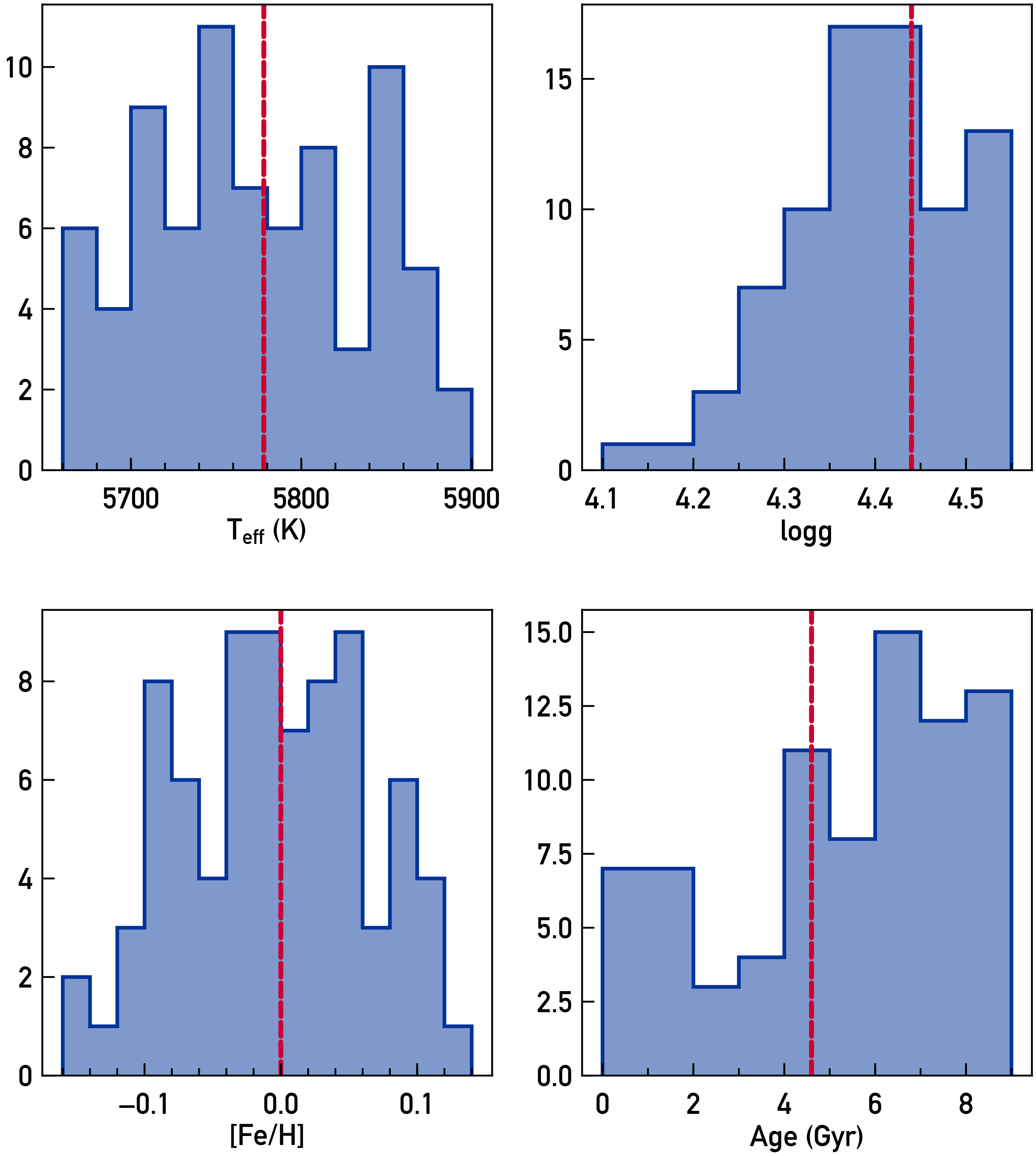

Figure 1.3 Fundamental parameters $T_{\rm eff}$, $\log g$, [Fe/H], and isochrone-based age estimates for all targets in the abundance analysis sample. Solar values are represented by dashed vertical lines.

of around five minutes and an RV amplitude on order 1 m s^{-1} for Sun-like stars (see Dumusque et al., 2011a, and references therein). Since all of our targets are bright ($m_V < 9.5$), we were able to achieve SNR > 100 pix^{-1} at 600 nm for each spectrum, ensuring that photon noise contributed well under 1 m s^{-1} to the overall RV uncertainty.

Our assigned observing schedule each semester typically consisted of one seven-night run and one four-night run, spaced at one per quarter. Every visible target was observed once per night so that the majority of program stars received $\sim$ 11 observations each year. While necessary from a practical standpoint, the grouping of observations in discrete observing run windows means that we are not particularly sensitive to signals at $\sim$ 3 month periods in addition to the unavoidable 24-hour and one-year windows imposed by observability. During the final year of observing we received only twelve nights, but our time coverage was better spaced thanks to our time-sharing agreements with other HARPS users during these semesters.

The net result of our STPS HARPS program was a superb set of several dozen high-resolution, high-signal-to-noise, ultra-stabilized spectra for each of 68 extremely Sun-like stars. These spectra are useful not only for their precise time series RVs, but also for their ability to monitor stellar activity and other time-dependent spectral changes. Furthermore, by co-adding all available HARPS spectra for each target (including both the STPS targets and those additional twins observed by other HARPS programs) we can achieve SNR on order of 1000, enabling unprecedentedly high precision abundance analysis of these solar twins.

In this thesis, I will present the results of the STPS planet search and accompanying abundance analysis for 80 solar twins. Section I focuses on the radial velocity results and analysis, while Section II turns to the topic of stellar abundances. I conclude in Chapter 8 with a summary of the insights gained on solar twins and planet formation from this work, and a view of what may come from future endeavors.

Part I

Hunting for Planets Around Solar Twins

CHAPTER 2

HIP11915: A SOLAR SYSTEM ANALOG

In this chapter we present our first detection from the planet search program: a Jupiter twin around the solar twin HIP11915.[1]

HIP11915 was previously established as a solar twin in Ramírez et al. (2014b) based on its fundamental properties (T_{eff} = 5760 ± 4 K, log g = 4.46 ± 0.01, and [Fe/H] = -0.059 ± 0.004). Its age, estimated from isochrone fitting to be 4.0 ± 0.6 Gyr, is also in keeping with the solar value (Ramírez et al., 2014b). HIP11915 is a bright (m_V = 8.6) star with relatively low activity (log(R'_{HK})< -4.8), making it an excellent target for high-precision RV monitoring. Based on a Keplerian signal in our HARPS RVs, we determine the planet candidate's orbital parameters. We also investigate the influence of stellar activity on our RV measurements.

2.1 Data

All of the RV data used in this paper were obtained with the HARPS spectrograph on the ESO 3.6 m telescope at La Silla Observatory and were processed with the dedicated HARPS pipeline. Forty-three data points spanning a time range from October 2009 to January 2015 came from our HARPS large program dedicated to solar twin stars (program ID 188.C-0265). An additional 13 measurements were taken from the publicly available archive data and span a time range from October 2003 to November 2013 (program IDs 072.C-0488, 089.C-0732, 091.C-0034, 092.C-0721, and 183.C-0972).

For the 43 measurements taken through our program, the star was observed in high-accuracy mode with the ThAr lamp as a simultaneous reference source. Each observation used a 900-second exposure time to minimize potential RV noise from the five-minute p-mode oscillations of solar-type stars. To obtain a radial velocity measurement, we selected

---

[1] This chapter is adapted from Bedell et al. (2015).

a binary mask based on the G2 spectral type for cross-correlation by the pipeline. Owing to their generally high signal-to-noise ratios (median S/N over the spectral range on the order of 100), the pipeline-produced RV error estimates were generally below 1 m s^{-1}. We expect the actual uncertainties to be somewhat higher owing to stellar noise and potential undiagnosed instrumental effects. To account for these factors, we added the pipeline-estimated errors in quadrature with a baseline error level of 1 m s^{-1}, following Dumusque et al. (2011b) and in accordance with the scatter in our own HARPS survey's quietest stars.

The 13 archive measurements have exposure times ranging from 120 to 900 seconds. All were taken in high-accuracy mode without a source on the simultaneous reference fiber, so that even the low S/N measurements are not in danger of spectral contamination by the simultaneous reference source. The data were processed by the pipeline and we modified the error estimates as described above. An additional 1.1 m s^{-1} was added in quadrature to the errors on all exposures under 15 minutes, based on the expected p-mode signal for a solar twin (Bazot et al., 2011).

We analyzed all of the reduced HARPS spectra to measure the Ca II H&K activity indices S_{HK} and $\log(R'_{HK})$at each observation epoch. This was done according to the methods of Lovis et al. (2011). Errors on S_{HK} were estimated from photon noise.

2.2 Analysis and results

The RMS of the RVs is 6.5 m s^{-1}, indicating the presence of a signal stronger than the predicted stellar jitter of 2.1 m s^{-1} (Wright, 2005). Visual inspection and a periodogram analysis of the data clearly show a long-period trend in the stellar radial velocities. We ran a grid search across a range of periods from 0 to 10,000 days and found that the minimum chi-squared value lies near 3600 days.

We inspected the data for signs of stellar activity manifesting in the RVs. A strong correlation between radial velocity and the activity index S_{HK} is seen in the measurements from recent years, although there is no correlation in the archival data. Similar RV-correlated behavior is seen for other activity indicators including the bisector inverse slope (BIS), FWHM, V_{span}, and the biGaussian fit differential (as defined by Queloz et al., 2001; Boisse et al., 2011; Figueira et al., 2013). Doing a weighted linear least-squares fit and removing the trend with any of these activity indicators from the RVs results in reducing the correlations while preserving the long-period planet signal with high significance in a periodogram analysis. We additionally attempted the prescribed method of Dumusque et al. (2011b) of fitting a long-period Keplerian first to an activity diagnostic and then (with period and phase fixed) the RVs. This method failed to remove the long-period power from the RVs regardless of whether S_{HK} , BIS, or FWHM was used as the diagnostic. The failure of these methods to successfully "clean" the data of its long-period signal suggests that the signal originates from a true Doppler shift rather than stellar activity, although activity is also present in the data.

2.2.1 Best model: Keplerian signal + S_{HK} correlation

In the results presented here, we account for stellar activity by fitting a linear trend between RV and S_{HK} simultaneously with the Keplerian signal. This way the strength of the correlation between activity indicator and RV is free to change as the scatter induced by the Keplerian signal is removed. We use S_{HK} as the primary tracer of activity owing to the unreliability of the BIS diagnostic for slow-rotating stars and the demonstrated efficiency of S_{HK} in removing activity cycle signals (Boisse et al., 2011; Meunier & Lagrange, 2013). Other potential diagnostics and alternative model choices are explored in Section 2.2.2.

We ran a Markov chain Monte Carlo (MCMC) analysis to fit the radial velocity data to a model consisting of three components: a Keplerian signal, a linear correlation term with the S_{HK} values, and an offset term. This gives seven free parameters: the Keplerian parameters (P, K, e, $\omega + M_0$, ω - M_0), where P is the orbital period, K is the RV semi-amplitude, e is eccentricity, ω is the argument of periastron, and M_0 is the mean anomaly at reference date $t_0 = 2457000.0$; a slope parameter α which relates the activity-induced change in RV to the corresponding change in S_{HK} ; and an offset parameter, C. We include an eighth free parameter, σ_J, representing the jitter that must be added in quadrature with the estimated RV error to make the measurement uncertainties consistent with the scatter in the residuals. This jitter physically corresponds to unknown Gaussian error that may arise from stellar noise or undiagnosed instrumental variations. When inputting the data, we subtracted a sigma-clipped median value from RV, S_{HK} , BIS, and FWHM for simplicity. This means that the offset parameter C is partially set by the difference between the median RV of the data set and the systemic RV of the star, but also includes the RV offset in the linear fit with the median-subtracted S_{HK} values (or any other correlations used in the model; see Section 2.2.2).

All of the fit parameters were given uniform priors except for P and K, which were sampled in log-space with a log-uniform prior. We ran five parallel chains and used the requirement of a Gelman-Rubin test statistic below 1.01 for all parameters to avoid non-convergence (Gelman & Rubin, 1992). The best-fit orbital solution, plotted in Figure 2.1, corresponds to an approximately Jupiter-mass planet on a 10-year orbit with eccentricity consistent with zero (see Table 2.1). As seen in the MCMC posterior distributions (Figure 2.5), the chief source of uncertainty in the period measurement is in its degeneracy with eccentricity and the associated argument of periapse, parameters that are inevitably poorly constrained when only one orbit has been observed. The best-fit jitter term is consistent with the predicted stellar jitter of 2.1 m s^{-1} from the formula of Wright (2005).

After subtracting the best-fit planet signal, we searched for additional signals in the residuals with a generalized Lomb-Scargle periodogram analysis (Zechmeister & Kürster, 2009). No significant periodicities were identified in the residuals to the planet fit or in the residuals to the planet and the fitted S_{HK} trend. We place constraints on the presence of additional planets in the system using a test based on the bootstrapping and injection of a planet signal into the residuals. For this test, we use the residuals to the planet fit only, and inflate the error bars (with jitter included) such that a flat-line fit to the residuals gives a

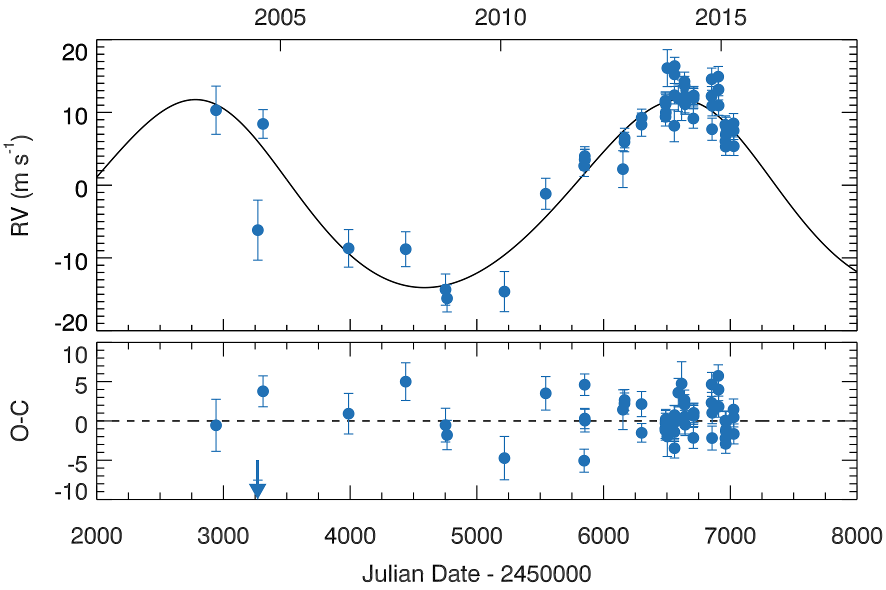

Figure 2.1 Best-fit orbital solution for HIP11915b. Data points are the observed RVs with offset and S_{HK} correlation terms subtracted. One residual point is located outside of the plot range, as denoted by the arrow.

reduced chi-squared of one. We then run a set of trials in which the RV data are resampled with replacement at the times of observation, a planet signal with period and semi-amplitude fixed and the other orbital parameters randomized is injected, and the reduced chi-squared of a flat-line fit to these simulated data is measured. If the chi-squared statistic has increased with three-sigma significance in 99 out of 100 trials at a given period and velocity semi-amplitude, we consider such a planet signal to be excluded based on its inconsistency with the scatter in the actual RVs. We run this trial until upper limits on planet presence are found for all of the periods in a log-sampled grid. The results rule out the presence of gas giants within a 1000-day orbital period, leaving open the possibility of inner terrestrial planets (Figure 2.2).

2.2.2 Alternative model choices

It is not obvious from theory that the Keplerian + S_{HK} correlation model used above should be the best model choice. Other activity indicators exist and have been used with success

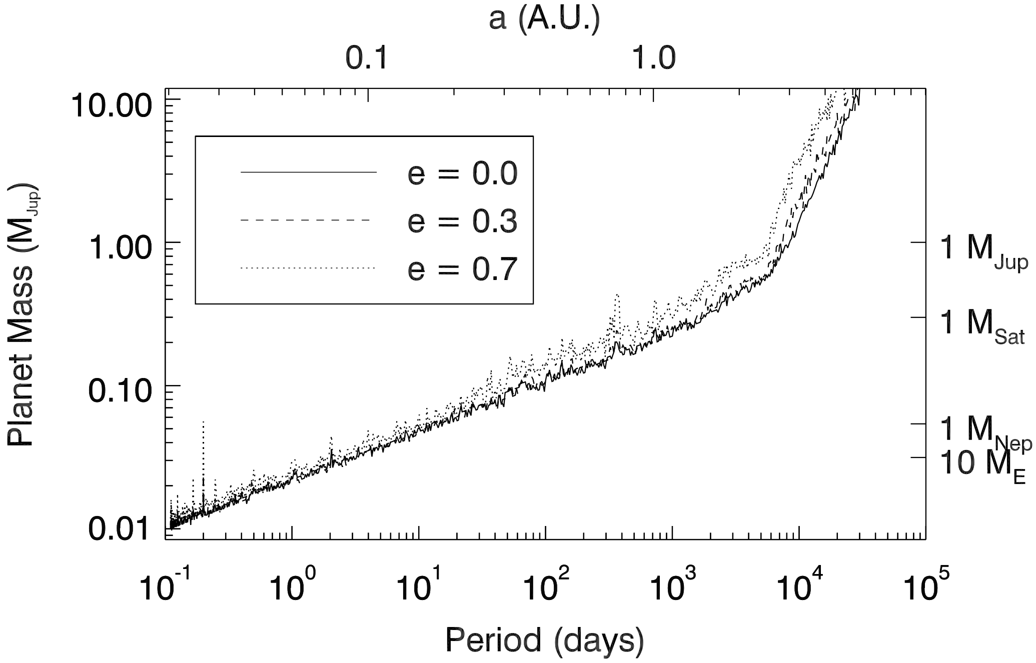

Figure 2.2 Exclusion limits on potential planets in the RV data after subtraction of the Keplerian signal. Any signal in the parameter space located above the lines plotted would have induced a larger scatter in the RV residuals with three-sigma significance if present. Potential trends with activity indicators were not removed for this test to avoid underestimating the RV scatter.

Table 2.1 Best-fit parameters and uncertainties for HIP11915b.

Parameter		Value	Uncertainty
P	[days]	3830	150
K	[m s^{-1}]	12.9	0.8
e		0.10	0.07
$\omega + M_0$	[rad]	3.0	1.3
ω - M_0	[rad]	2.4	0.1
α	[m s^{-1} (unit S_{HK})$^{-1}$]	160	60
C	[m s^{-1}]	-11.0	1.3
σ_J	[m s^{-1}]	1.8	0.4
m_p sin(i)	[M$_{\rm Jup}$]	0.99	0.06 [a]
a	[AU]	4.8	0.1 [a]
RMS	[m s^{-1}]	2.9	

---

[a] Error estimates do not include uncertainties on the stellar parameters, which were taken from Ramírez et al. (2014b).

to remove activity trends from RVs in the past. Chief among these are BIS and FWHM, both characteristics derived from the RV cross-correlation function (CCF) which measure the average spectral line asymmetry and/or broadening at the epoch of the observation (see, e.g., Queloz et al., 2001, 2009). Either BIS or FWHM could potentially be used in place of S_{HK} . Also, because these indicators arise from distortions to the rotationally broadened stellar absorption lines while S_{HK} probes chromospheric emission, we could combine S_{HK} with a CCF-derived measurement to simultaneously track two separate physical indicators of activity.

We considered several alternative models before settling on the Keplerian + S_{HK} model as the best choice. A summary of the models tried is given in Table 2.2. In all cases, the fitting was done with an MCMC as described above. The inclusion of a Keplerian signal is strongly justified, with the Keplerian + S_{HK} fit having a false alarm probability on the order of 10^{-15} compared to the best fitting activity model (S_{HK} + FWHM). While the lowest χ^2 value is obtained for the fit to a Keplerian, S_{HK} , and FWHM, the addition of the FWHM term is not fully justified by the reduction in scatter around the fit. An F-test gives a formal false alarm probability of 13% for the Keplerian + S_{HK} + FWHM model compared to the simpler Keplerian + S_{HK} model. The Keplerian + S_{HK} fit has a false alarm probability of 0.3% when compared to the Keplerian only model. Using BIS in place of S_{HK} technically gives a slightly better fit, but we chose to use S_{HK} in the main analysis because of BIS's previously noted unreliability for slow rotators. Regardless of the choice of activity indicator(s), all Keplerian fit parameters remain within the uncertainty intervals quoted in Table 2.1.

2.3 Planet or activity cycle?

The question of the role of stellar activity role in the observed radial velocities is of special importance given the proximity of the signal period to the 11-year solar magnetic cycle. The signal size is also consistent with the theoretically predicted 10-11 m s^{-1} signal for a solar

Table 2.2 Models considered for HIP11915 RVs.

Name	Degrees of Freedom	χ^2 of Fit
Keplerian only	50	162.54
Keplerian + S_{HK}	49	136.00
Keplerian + FWHM	49	145.32
Keplerian + BIS	49	133.96
Keplerian + S_{HK} + FWHM	48	129.50
S_{HK} only	54	897.78
BIS only	54	704.27
FWHM only	54	650.97
S_{HK} + BIS	53	719.28
S_{HK} + FWHM	53	639.76

activity cycle (Meunier & Lagrange, 2013). However, an activity cycle should manifest not only in the observed RVs, but also in other diagnostics. We expect a positive correlation in RV with the activity index S_{HK} as well as with other diagnostics such as BIS and the FWHM of the cross-correlation function (Lovis et al., 2011; Zechmeister et al., 2013). While such correlations are seen, they appear insufficient to fully explain the observed RVs.

For at least two other solar twins in our sample, similar Jupiter-like RV variations are seen; however, in these cases subtracting a linear fit with S_{HK} entirely removes the long-period power from a periodogram and reduces the RMS of RVs to a level consistent with the expected stellar jitter. In contrast, the RV signal inferred from the variation of S_{HK} or any other activity tracer for HIP11915 is much smaller in size than the total RV signal, so that significant power remains at long periods in the periodogram.

A large sample of stars with activity cycles have been studied with HARPS by Lovis et al. (2011), who derived empirical predictions for the expected correlation between RV and other activity indictors with R'_{HK} as a function of stellar temperature and metallicity. The correlations seen for HIP11915 are generally lower than the predicted values: $C_{RV} = 30 \pm 1$ m s^{-1} (unit $R'_{HK})^{-1}$, $C_{FWHM} = 58 \pm 2$ m s^{-1} (unit $R'_{HK})^{-1}$, and $C_{BIS} = 22.4 \pm 0.7$ m s^{-1} (unit $R'_{HK})^{-1}$ from their Equations 9-12, while the C values recovered from our data are 11, 45, and 16 respectively. This disagreement suggests that the strength of activity seen in the data is insufficient to explain the RV signal.

An alternative interpretation is that we are observing activity overlaid with a planet signal in the radial velocities. In this view, the correlation with activity indicator(s) in the RV residuals is independent of the Keplerian signal. One piece of evidence in favor of this interpretation comes from inspecting the correlation plots before and after removal of the 3800-day Keplerian signal. If this signal is truly unrelated to the stellar activity, it should add random scatter about the correlation. Indeed, subtracting the Keplerian signal from the data reduces the scatter about the best-fit trend between RV and S_{HK} from 7.7 to 3.0 m s^{-1} and has a comparable effect on the correlations with other activity indices (Figure 2.3).

Inspecting the behavior of S_{HK} with time sheds some light on the evolution of HIP11915's activity level. As depicted in Figure 2.4, the stellar activity level exhibited an incoherent scatter until mid-2013, at which point it increased from the equivalent of $\log(R'_{HK})\sim$ -4.87 to $\sim$ -4.82 by mid-2014. A concurrent rise in BIS and FWHM is also seen at this epoch. This level of variability is consistent with the behavior of the Sun, which has a mean $\log(R'_{HK})$of -4.94 and an amplitude of variation around 0.1 dex over a full activity cycle (Hall et al., 2007). Given the recent increase in Ca emission, we could then expect a corresponding increase in short-duration activity phenomena such as spots and plages to manifest in the more recent RVs. This would add power to the correlations with line asymmetry indicators.

Ideally, we would be able to remove activity phenomena such as spots and plages by averaging our measurements over the timescale of the stellar rotation period, on the order of a month. Unfortunately the sampling of the data is too uneven to average effectively over the rotation period. We average instead over an entire observing season, which is a regime in which the time coverage should be distributed evenly enough to remove activity signals at periods shorter than a cycle. The resulting data from this seasonal binning trace the 3800-day signal well, but show no statistically significant correlations with activity indicators.

In short, we have considered a variety of activity diagnostics and methods of cycle removal and the 3800-day signal remains robustly present in the data. The coincidence in phase between the rise in S_{HK} and the 3800-day signal maximum, however, calls for further

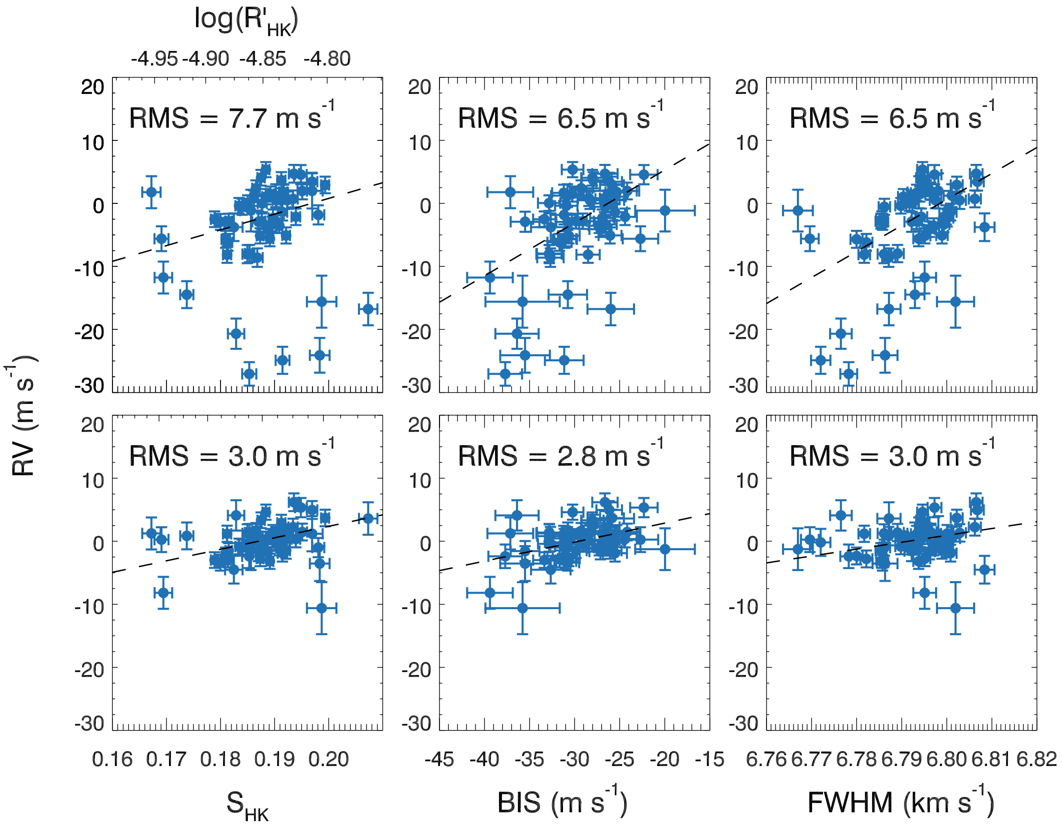

Figure 2.3 Correlations for the activity tracers S_{HK} , BIS, and FWHM with radial velocity. The upper panels shows the observed RVs. The lower panels show the residuals to the 3800-day signal fit (as presented in Section 2.2.1). Dashed lines are linear least-squares best fits to the data.

monitoring of the star before we can definitively rule out the possibility of an activity cycle inducing the RV signal.

2.4 Summary

We have detected a Keplerian signal corresponding to a gas giant planet with a 10-year orbital period, consistent with a Jupiter twin, around the solar twin HIP11915. While we cannot conclusively exclude an activity cycle interpretation, commonly employed activity tracers fail to account for the signal. If the 3800-day signal is entirely induced by an activity cycle, the failure of various techniques to remove it bodes poorly for the prospect of correcting

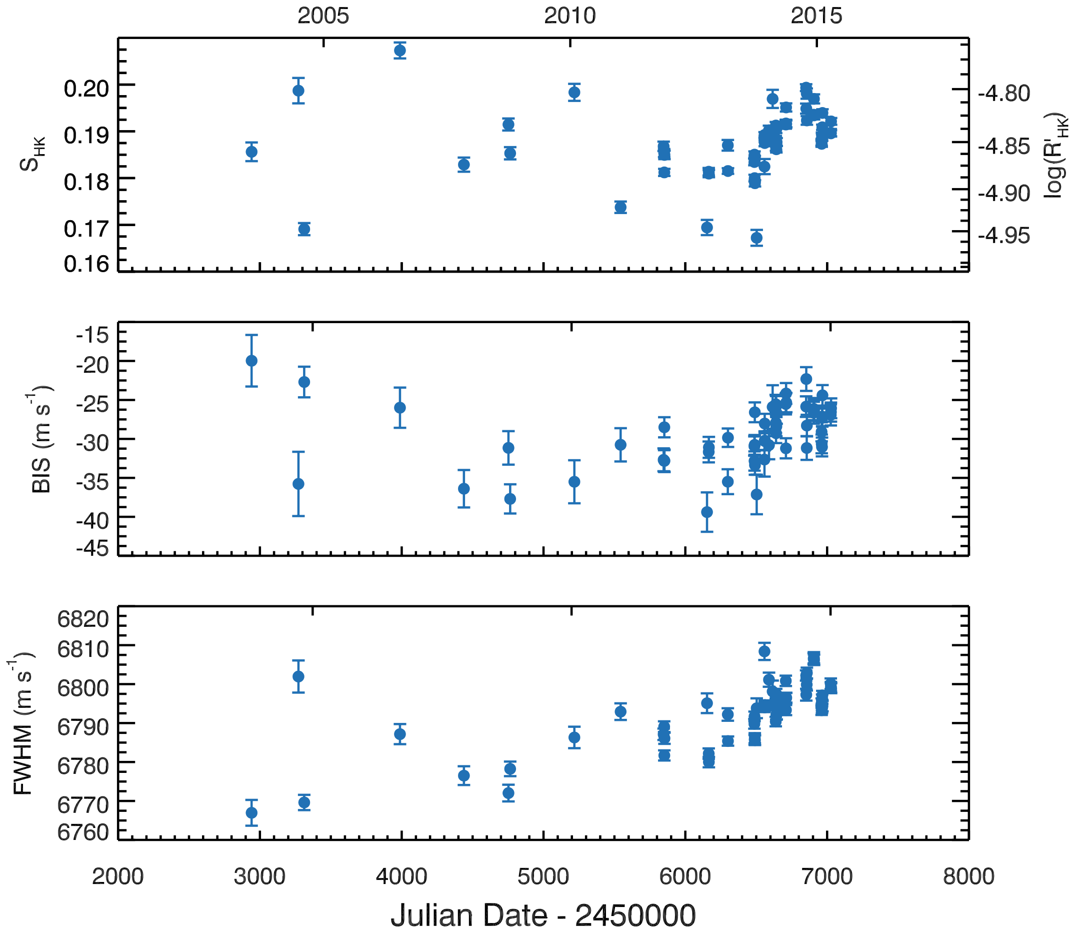

Figure 2.4 Evolution of the activity indices S_{HK} , BIS, and FWHM with time. Errors on BIS and FWHM are approximated as the errors on the RVs.

for such cycles in future long-period planet searches.

If this signal is truly planetary in origin, the HIP11915 system is a close analog to the solar system. Our analysis shows the planet HIP11915b to be a close match to Jupiter both in mass and orbital period, and its host star is extraordinarily similar to the Sun. Beyond having fundamental physical properties close to the Sun, initial spectroscopic analysis suggests that HIP11915 is also a solar twin in the sense that its detailed abundance pattern matches the solar pattern. The presence of a Jupiter twin and a solar-like composition both make HIP11915 an excellent prospect for future terrestrial planet searches.

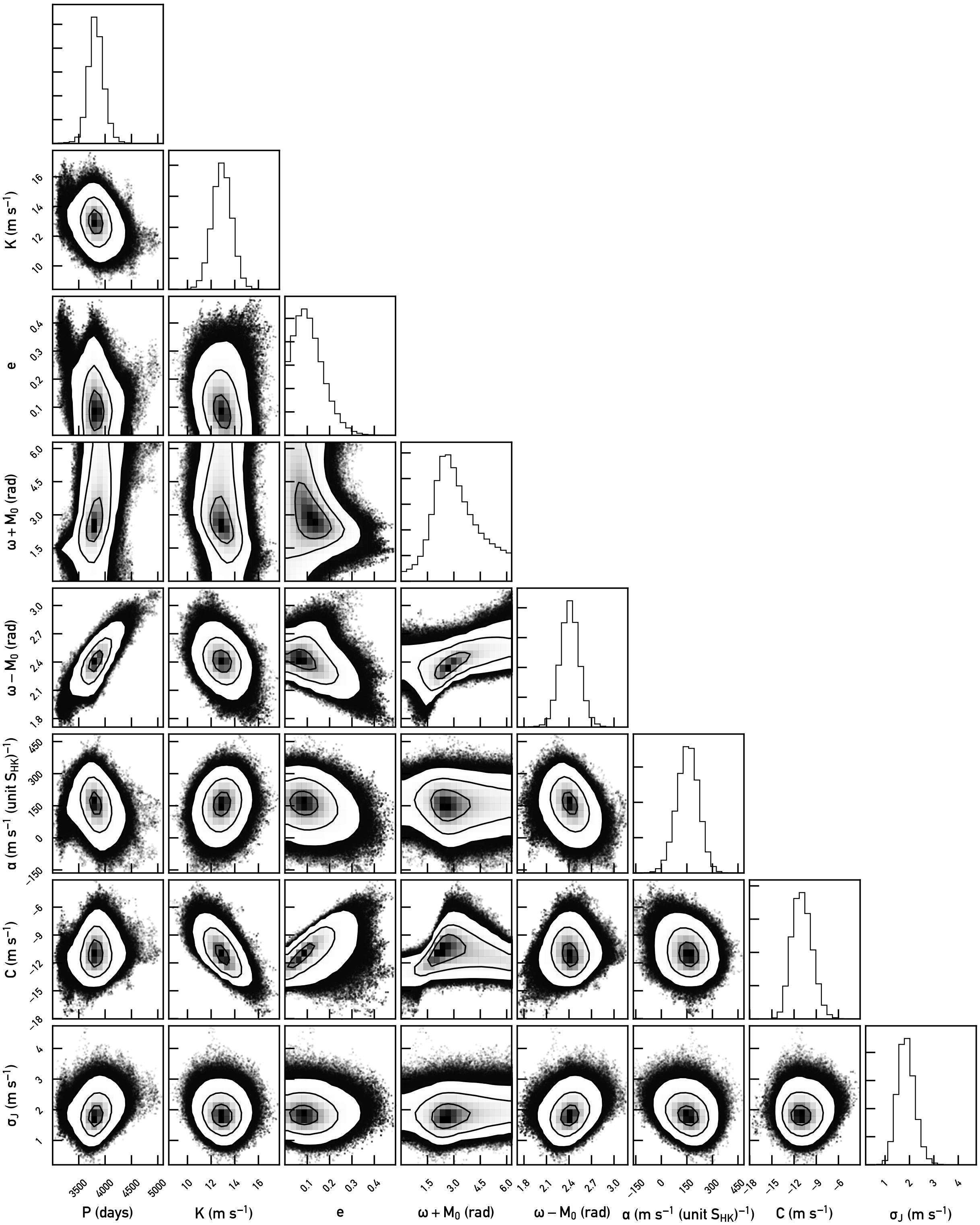

Figure 2.5 Constraints on the fit to the radial velocities from the MCMC analysis. Parameters are defined in Section 2.2. Plot made using `corner` (Foreman-Mackey, 2016).

CHAPTER 3

HIP68468: A CANNIBAL STAR?

In this chapter we present the second and third planets discovered from our dedicated solar twin planet search, and discuss how the system's planetary architecture may be related to the host star's unusual chemical abundances.[1] The system presented here consists of a solar twin of approximately Sun-like age, HIP68468, and two candidate planets: HIP68468b, a 2.9 ± 0.8 M_E planet on a very short orbital period, and HIP68468c, a 26 ± 4 M_E planet at a Venus-like distance from its host star.

3.1 Planet detection

3.1.1 Data

HIP68468 was observed with the HARPS spectrograph (Mayor et al., 2003) on the ESO 3.6 m telescope at La Silla Observatory during 43 nights between 2012-2016. These observations were carried out under our large program targeting solar twin stars (program ID 188.C-0265). Each night's observation consisted of one 1300-second exposure for this $V = 9.4$ star. This exposure time is long enough to average out *p*-mode stellar oscillations typical of solar-like stars, and to achieve a photon-limited precision of 1 m s^{-1} in typical observing conditions. On two of the observing nights, two 1300-second exposures were taken with a 2-hour time gap between them. In total, we obtained 43 RV measurements for the star.

All HARPS data were processed with version 3.8 of the dedicated HARPS pipeline, which determines radial velocities through a cross-correlation technique using a G2 binary mask. Uncertainties on the RVs came from the pipeline estimation, which accounts for photon noise in the cross-correlation. An additional 1 m s^{-1} was added in quadrature to account for the instrumental noise floor (Dumusque et al., 2011b). The Ca II H&K spectral lines

---

[1] This chapter is adapted from Meléndez, Bedell et al. (2017).

were measured by us, and the resulting S_{HK} activity indices were converted to the standard Mount Wilson $\log(R'_{HK})$ index using the relation derived by Lovis et al. (2011).

The HARPS instrument underwent an upgrade in June 2015 including the installation of new fibers and instrumental re-focusing. This upgrade altered the instrumental profile and introduced offsets in the measured RVs relative to the pre-upgrade RV zero point. We used the data for a set of ten stars in our program with relatively constant pre-upgrade RV time series (RMS ¡ 2 m s^{-1}) to characterize the offset. Although this offset is expected to have a dependence on stellar type, all stars in our program are solar twins and should therefore share the same offset. We find an offset of 15.4 ± 0.2 m s^{-1} among the constant solar twin sample. This value is in agreement with those obtained by the HARPS team using RV standard stars (Lo Curto et al., 2015). To properly account for the effect of the upgrade and its uncertainty, we include the RV offset as a free parameter in the model as described below.

3.1.2 Analysis and results

We identified candidate planet periods using a generalized Lomb-Scargle periodogram (Zechmeister & Kürster, 2009). For this initial analysis, we simply subtracted a 15.4 m s^{-1} offset from the data taken after the HARPS upgrade. Leaving aside the 1.0 and 0.5-day peaks that commonly arise from a nightly sampling cadence, the strongest periodicity in the data is at 194 days (Figure 3.1). To calculate its false alarm probability (FAP), or the probability that such a high-power peak could appear through random noise, we used a bootstrap Monte Carlo technique. The data were bootstrap sampled for 5000 trials, with the power of the highest peak recorded for each trial. The 90^{th} and 99^{th} percentiles of the resulting power distribution can be used as approximate 10% and 1% FAP thresholds. For the 194 day peak, we find that only 0.8% of the trials yielded a peak of equal or greater height by chance. The analytic FAP, using the formulation of Zechmeister & Kürster (2009), is even lower at 0.2%. Although 194 days is somewhat close to half of a year and the associated window function peak at 171 days, the phase coverage of the signal is nonetheless sufficient to fit a Keplerian robustly. No combination of significant periodicities from the window function and the data would feasibly combine to produce an alias peak at a 194-day period (Dawson & Fabrycky, 2010).

We modeled and removed the 194 day signal using a least-squares algorithm to simultaneously fit the Keplerian orbital parameters and the RV offset introduced by the HARPS upgrade (δ_{inst}). The periodogram of the residuals to this fit showed a peak at 1.84 days with a bootstrap FAP of 2%. Adding a Keplerian with a 1.84-day period to the least-squares model fit yielded a two-planet solution which substantially reduced the residuals of the one-planet fit.

After removing both 194-day and 1.84-day signals, no significant peaks remained in the residuals periodogram (Figure 3.1).

We ran a MCMC analysis using the specific implementation of Bedell et al. (2015) to obtain final confidence intervals on the two planet candidates' orbits, properly marginalizing over all uncertain parameters. Our model consisted of two Keplerian signals, a constant RV offset C relative to the instrumental zero point, an instrumental offset δ_{inst} for post-HARPS upgrade RVs, and a jitter term σ_J. The Keplerian signal was parameterized as (P, K, e, ω + M_0, ω - M_0), where P is the orbital period, K is the RV semi-amplitude, e is eccentricity, ω is the argument of periastron, and M_0 is the mean anomaly at a reference date set by the first RV measurement in the time series. All of the fit parameters were given uniform priors except for P and K, which were sampled in log-space with a log-uniform prior, and δ_{inst}, which was given a Gaussian prior with the mean and uncertainty as given in Section 3.1.1. After the MCMC run concluded, the chains were examined for non-convergence using the Gelman-Rubin statistic and any chains which had become stuck in a low-likelihood region of parameter space were removed from the posterior (Gelman & Rubin, 1992).

The resulting constraints on the two-planet fit are presented in Table 3.1. Due to strong correlations between the parameters and poorly constrained phases, taking the median values

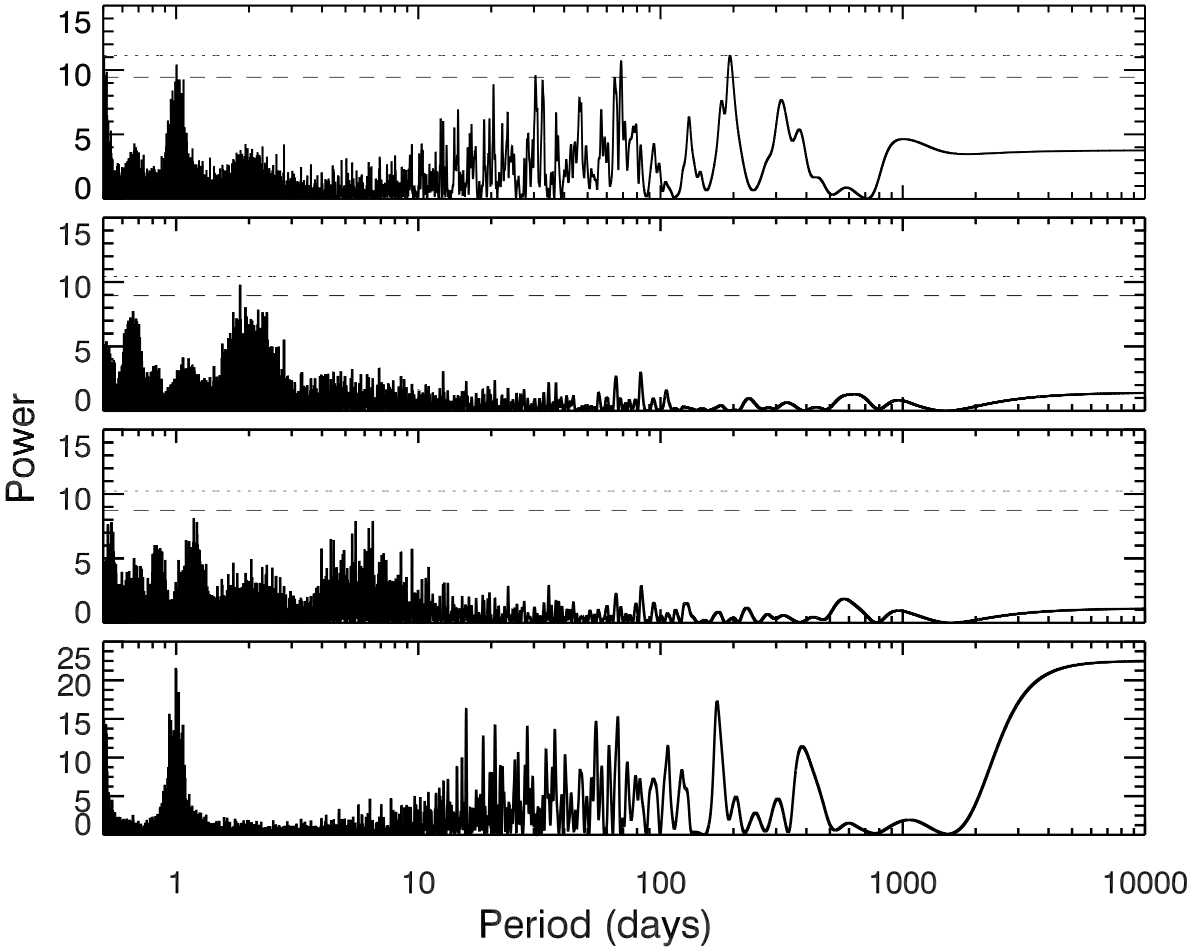

Figure 3.1 Generalized Lomb Scargle (GLS) periodograms to determine the frequencies of planet candidates. Top panel is a periodogram of the original data with instrumental upgrade offset removed. Middle panels are periodograms of the residuals to a 194-day Keplerian fit (upper middle) and a two-planet fit (lower middle). The horizontal lines represent false alarm probability levels of 10% (dashed) and 1% (dotted), as calculated from a bootstrap Monte Carlo method. Also included for comparison is the window function of the sampling (bottom panel).

from each parameter posterior does not actually result in a good fit. We quote both best-fit values from the maximum likelihood fit and MCMC median values in Table 3.1. The quoted errors are the one-sigma range, percentile-wise, from the MCMC posteriors. The orbital solutions shown in Figures 3.2 and 3.3 use the best-fit parameters.

The final solution from the MCMC corresponds to a 2.9 ± 0.8 Earth mass planet with an orbital period of 1.8374 ± 0.0003 days and a 26 ± 4 Earth mass planet with an orbital period of 194 ± 2 days. Both eccentricities are consistent with zero within 2σ. The jitter term is low (consistent with zero), indicating that HIP68468 is a relatively quiet star without much activity.

3.1.3 Model comparison

Periodograms are a useful tool for identifying signal periods of interest, but the periodogram FAP is not the most robust tool available to assess the reality of signals found. We ran multiple MCMCs to fit alternative models to the data. All models include the instrumental offset factors and a jitter term, but vary in the number of Keplerian signals included. We compared the models using the Bayesian Information Criterion (BIC, Kass & Raftery, 1995), calculated from the highest likelihoods achieved in the MCMCs for each model. The results indicate that the two-planet model including a 1.84-day super-Earth has the smallest BIC and is therefore the most likely solution of those tested (see Table 3.2). We also compared the best-fit solutions for each model as determined by a least-squares algorithm with similar results.

Evidence from the BIC and χ^2_{red} strongly support the presence of the outer planet: the Δ BIC is large at 11.5, and an F-test comparing the one-planet model to the no-planet model gives a probability of about 10^{-4} against the planet's presence. Inclusion of the super-Earth signal improved the fit further, reducing the χ^2_{red} from 1.6 to 1.0 and bringing the RMS down from 1.7 to 1.3 m s^{-1}. An F-test comparison using the best-fit chi-squared statistics gives a probability of 7×10^{-4} that the inclusion of the second planet is unwarranted.

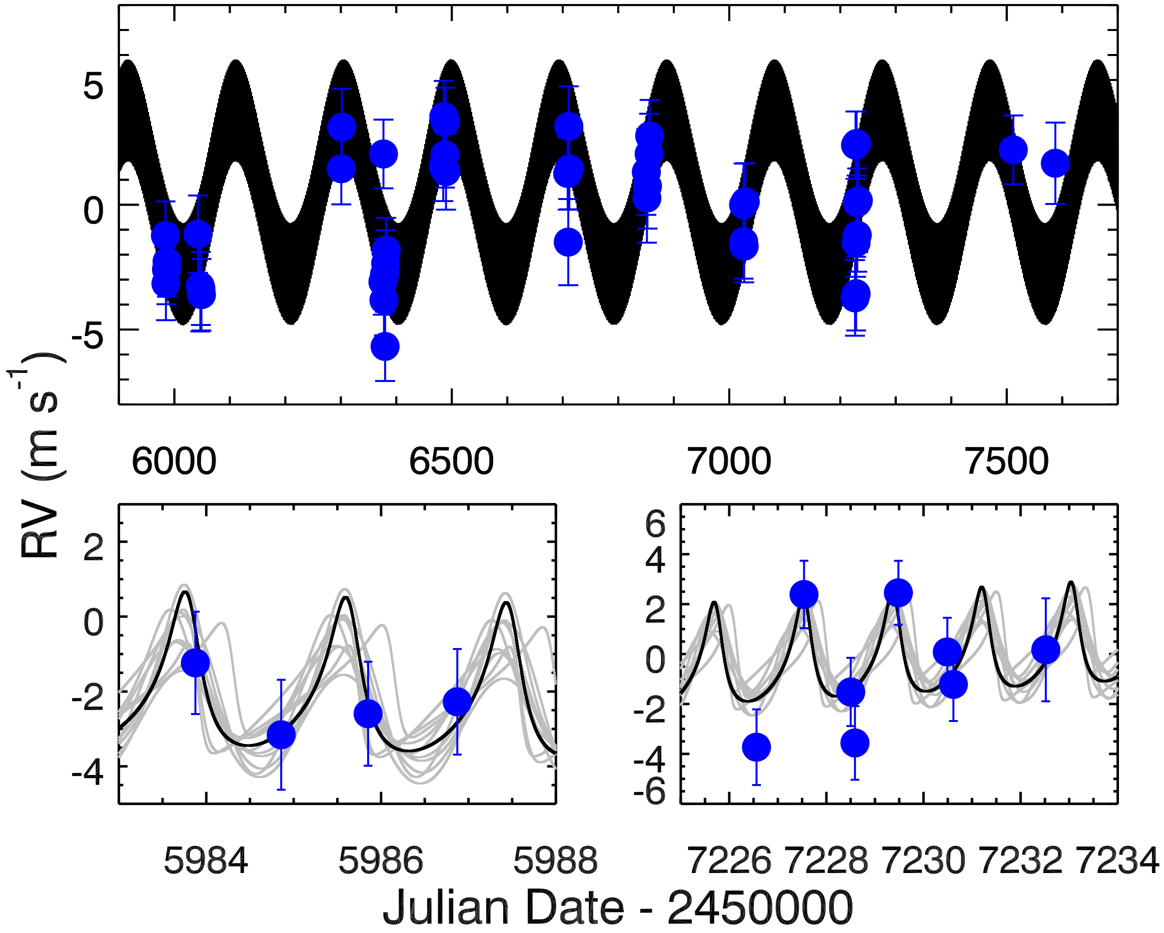

Figure 3.2 Full time series of RV data (blue) and two-planet best-fit model. The two lower panels show zoomed-in subsets of the time series. The black line is the best-fit model from a least-squares fit. The grey lines are models randomly drawn from the one-sigma range of best steps in the MCMC analysis. As illustrated by the grey models, the eccentricity of the inner planet is not well constrained.

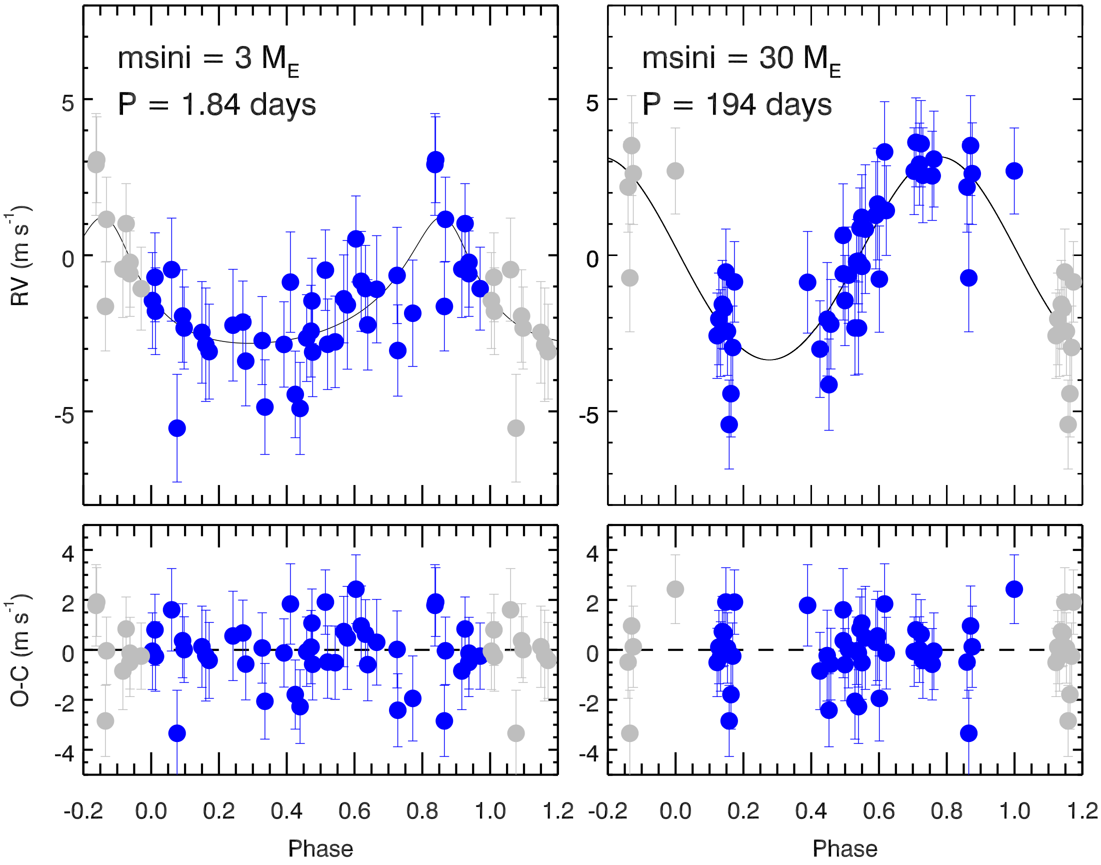

Figure 3.3 Phase-folded RV data for the two Keplerian signals. The upper panels show the RV data with the other planet and offsets removed. The best-fit Keplerian model is overplotted, with residuals in the lower panel. Grey points are duplicated observations plotted for clarity.

3.1.4 Stellar activity indicators

Although HIP68468 is a quiet star with a low log(R'$_{HK}$) value (averaging -5.05 in the HARPS spectra), we nevertheless examined the data for signs that stellar activity could be inducing a false RV signal. No statistically significant trends were found between RV and log(R'_{HK})or bisector inverse span (BIS). A marginally significant correlation was found between RV and the full width at half maximum (FWHM) of the cross-correlation function, with a p-value of 1.4% from bootstrap resampling. Subtracting this trend from the RV data does not have a noticeable effect on the shape of the periodogram; a peak around 190 days still stands out, although the significances of all peaks are reduced.

The periodogram of the FWHM shows a peak at 41 days, which may be a signature of the rotation period (Figure 3.5). We were unable to fit and subtract any quasi-periodic 41-day activity signals from the data as suggested in e.g. Dumusque et al. (2011b). This is could be due to the limitations of the time series sampling in resolving any evolving stellar activity. We instead treat the relationship between activity indicator and activity-induced RV shift as a linear trend with an unknown slope, which should be accurate as a first-order approximation (Dumusque et al., 2014).

We ran the MCMC algorithm with models incorporating a linear FWHM correlation in addition to the Keplerian signal(s). Because the FWHM measurement suffered the same unknown offset effect as the RVs after the HARPS upgrade, we accounted for this in a similar way by adding an additional $\delta_{inst,FWHM}$ term to the model with a strong prior based on the average FWHM offset among our constant stars of 15.6 ± 0.4 m s^{-1}.

Regardless of initial conditions, the strength of the FWHM correlation term consistently went to a low value (0.13 ± 0.05). All of the orbital parameters for the 2-planet solution remained well within 1 σ of the values given in Table 3.1. We therefore conclude that any stellar activity traced by the FWHM is likely independent of the Keplerian signals in the data. We chose not to include the FWHM correlation in the final fit presented based on the weak evidence for its addition to the model: a marginally higher BIC by 1 compared to the

2-planet model, and an F-test probability of 8% that the addition of a correlation term is unwarranted. We note, however, that the two-planet model remains the best fit regardless of whether or not an FWHM correlation is included (Table 3.2).

3.1.5 Orbital eccentricities

Both the MCMC and least-squares fitting yield non-zero eccentricities for both Keplerian orbits. However, as a positive definite parameter, eccentricity is prone to overestimation when an orbit is truly circular (Zakamska et al., 2011). We present the posterior distributions of several key orbital parameters, including eccentricity, in Figure 3.4. From the posteriors, it is clear that the mode of the eccentricity distribution (recommended as the least biased estimator by Zakamska et al., 2011) is within 1σ of zero for both planet candidates. Nevertheless, we chose not to fix either eccentricity to zero in the MCMC analysis because the uncertainty on eccentricity should be marginalized over when making an estimate of the errors on all parameters.

The eccentricity found for the innermost planet (HIP68468b) is remarkably high, albeit as discussed above, within the uncertainties $e = 0$. If the high eccentricity is confirmed with further RV observations, it would be a short living phenomenon, as the orbit should be circularized in a timescale $<<$ 1 Gyr. The exact timescale for tidal circularization would be better defined once a more precise eccentricity is available, and if a measurement of the planet radius is made through transit observations, so that we can estimate the planet composition. We have recently obtained observing time with the *Spitzer Space Telescope* to attempt the transit detection of HIP68468b.

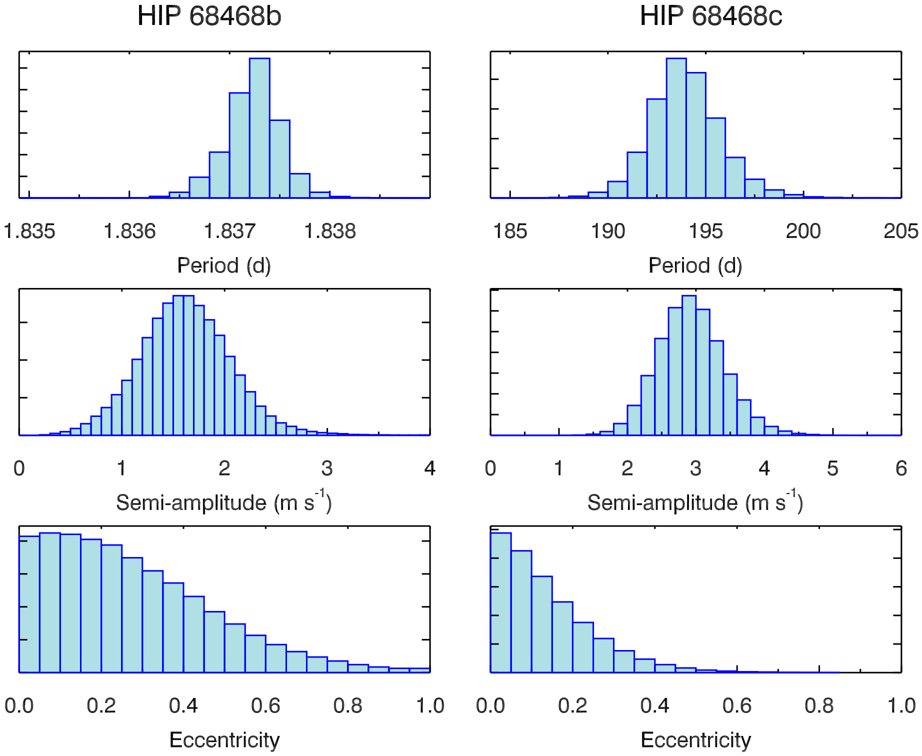

Figure 3.4 Posterior distributions of orbital period, radial velocity semi-amplitude, and eccentricity for HIP68468 b & c.

Table 3.1 Best-fit parameters and uncertainties for HIP68468 b & c.

		HIP68468 b		HIP68468 c	
Parameter		Best-Fit Value	MCMC Posterior	Best-Fit Value	MCMC Posterior
P	[days]	1.8372	1.8374 ± 0.0003	194	194 ± 2
K	[m s^{-1}]	2.0	1.5 ± 0.5	3.3	2.9 ± 0.5
e		0.41	$0.24^{+0.24}_{-0.17}$	0.04	$0.11^{+0.14}_{-0.08}$
$\omega + M_0$	[rad]	3.0	2.7 ± 1.7	0.0	$3.7^{+1.9}_{-2.5}$
ω - M_0	[rad]	2.5	$2.4^{+0.5}_{-0.4}$	1.0	$1.0^{+0.2}_{-0.3}$
$m_p \sin(i)$	[M$_{\mathrm{Earth}}$]	3.5	2.9 ± 0.8	30	26 ± 4
a [a]	[AU]	0.029743	0.029744 ± 0.000003	0.665	0.664 ± 0.004
C	[m s^{-1}]	1257.2	$1256.2^{+1.1}_{-0.8}$		
δ_{inst}	[m s^{-1}]	15.4	15.5 ± 0.2		
σ_J	[m s^{-1}]		$0.4^{+0.4}_{-0.3}$		
RMS	[m s^{-1}]	1.3			

[a] Using host star mass of 1.05 M$_\odot$ (see text); error estimates do not include uncertainty on the stellar mass.

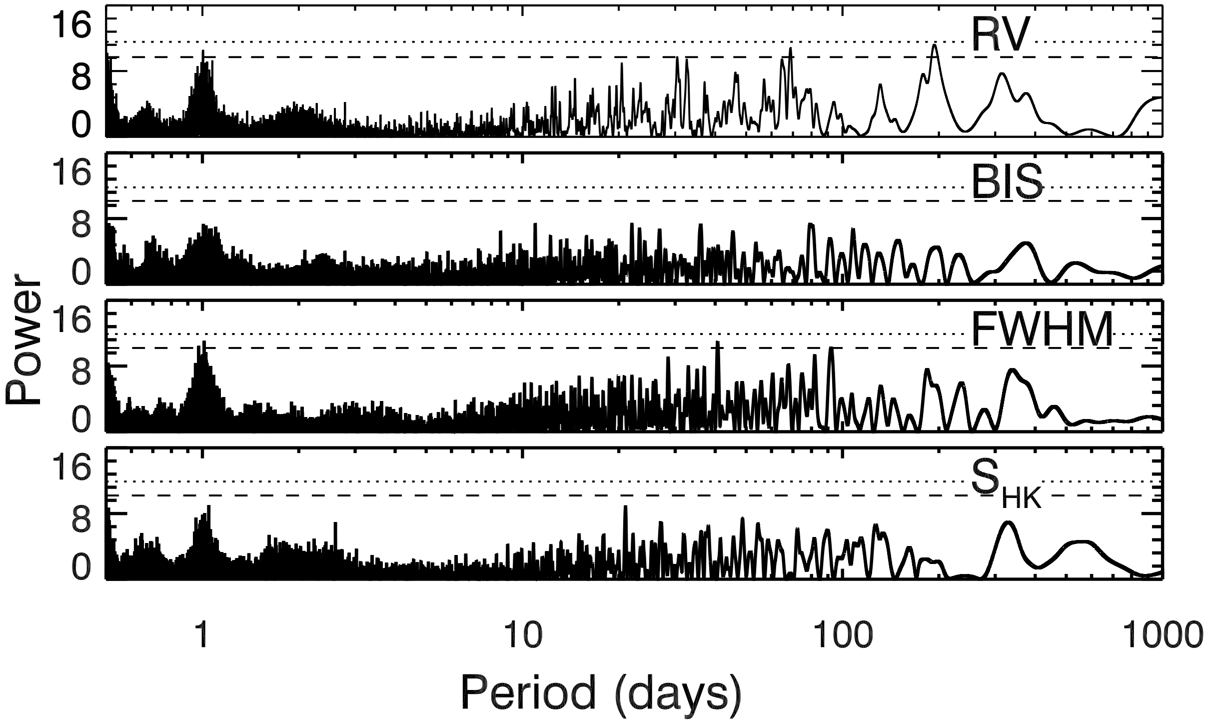

Figure 3.5 GLS periodograms of the RV data and various activity indicators for comparison. Horizontal lines correspond to false alarm probabilities of 10% (dashed) and 1% (dotted), as calculated from bootstrap Monte Carlo resampling.

Table 3.2 Models considered for HIP68468 RVs.

	BIC	χ^2_{red}	RMS [m s^{-1}]
No planets	217.8	2.9	2.4
No planets + FWHM correlation	222.8	2.6	2.3
194-d Keplerian	206.3	1.6	1.7
194-d Keplerian + FWHM correlation	211.0	1.6	1.7
194-d & 1.84-d Keplerians	199.0	1.0	1.3
194-d & 1.84-d Keplerians + FWHM correlation	200.2	0.9	1.2

3.2 Fundamental parameters and abundance analysis

3.2.1 Data and measurements

The spectra of HIP68468 and the Sun (reflected light from the asteroid Vesta) were taken using the MIKE spectrograph (Bernstein et al., 2003) at the 6.5m Clay Magellan telescope. The data were obtained with R = 65 000 in the red side (500 - 1000 nm) and R = 83 000 in the blue side (320 - 500 nm). The spectra have a signal-to-noise ratio (S/N) $\approx$ 400 per pixel at 600nm. The data were reduced using the CarnegiePython MIKE pipeline[2], and further processing (Doppler correction and continuum normalisation) was performed as described in Ramírez et al. (2014b). The MIKE data were employed to perform the equivalent width (EW) measurements used to determine stellar parameters and chemical abundances, and for spectral synthesis to determine v sin i and the lithium content.

The HARPS spectra described in Sect. 2.1 have a more limited wavelength coverage (380-690 nm) than the MIKE spectra, but they have a higher resolution (R = 120 000), hence they were used to verify through spectral synthesis both v sin i and the Li abundance. The combined HARPS spectrum of HIP68468 has S/N $\sim$750 at 600nm.

The EW were measured comparing line-by-line the spectrum of HIP68468 to the Sun in a 6 Å window, to help determine the continuum and to choose the part of the line profile that was used to fit a Gaussian profile. After the first set of measurements was obtained, 2-σ outliers were identified from the differential analysis and their EW were verified. The remeasured EW were kept, unless there was a problem, such as a contamination by a telluric line or a defect in one of the spectra.

3.2.2 Stellar parameters

The stellar parameters for our solar twin planet search sample were published in Ramírez et al. (2014b). Only three of the sample stars had revised stellar parameters based on the

---

[2] http://code.obs.carnegiescience.edu/mike

[Y/Mg] ratio, which can be used as a proxy for stellar ages (Nissen, 2015). The comparison between our isochrone ages (Ramírez et al., 2014b) and the [Y/Mg] ratio (Tucci Maia et al., 2016) shows that [Y/Mg] ages can be determined to better than 0.9 Gyr. As the isochrone age of HIP68468 determined in Ramírez et al. (2014b) was off by 1.2 Gyr relative to the age obtained from the [Y/Mg] ratio, and because the age of this star plays an important role in our interpretation, a reanalysis of HIP68468 was performed as described below.

We adopted the same line list as in Ramírez et al. (2014b). The EW measurements were used to obtain elemental abundances with the *abfind* driver of MOOG (Sneden, 1973), using Kurucz model atmospheres (Castelli & Kurucz, 2004). Then, line-by-line differential abundances were obtained.

The stellar parameters ($T_{\rm eff}$, log g, [Fe/H], v_t) of HIP68468 were determined by imposing a differential spectroscopic equilibrium of iron lines relative to the Sun (e.g. Meléndez et al., 2014b), using as initial parameters the values given in Ramírez et al. (2014b). The solar values were kept fixed at ($T_{\rm eff}$, log g, v_t) = (5777 K, 4.44 dex, 1.0 km s^{-1}). Our solution for HIP68468 gives consistent differential abundances for neutral and ionised species of different elements, and also for atomic and molecular lines, as discussed in more detail in the next section.

The errors in the stellar parameters were obtained from the uncertainties in the slope of the fits of the differential abundances versus excitation potential and reduced EW, and the errors in the differential ionisation equilibrium (based on the observational uncertainties in the differential abundances of FeI and FeII), and including also the degeneracy among the stellar parameters.

The resulting stellar parameters are $T_{\rm eff}$= 5857±8 K, log g = 4.32±0.02, [Fe/H] = 0.065±0.007, v_t = 1.14±0.01 km s^{-1}, which agree well with the previous estimate (5845±6 K, 4.37±0.02 dex, 0.054±0.005 dex, 1.13±0.01 km s^{-1}) by Ramírez et al. (2014b). The most important difference is seen in the log g value, which is reduced by 0.05 dex. This has a non-negligible effect on the derived age of the star (0.7 GYr, see below). HIP68468 is one of the most distant stars in our solar twin planet search sample, which prevents us from using its Hipparcos parallax to better constrain this important parameter. The Hipparcos parallax of HIP68468 has an error greater than 10% and the trigonometric log g value that we derive using that parallax is fully consistent with both the old and new spectroscopic parallaxes within the errors.

The mass and age of HIP68468 were determined using Y^2 isochrones (Demarque et al., 2004), as described in Meléndez et al. (2012) and Ramírez et al. (2013). With our stellar parameters and their uncertainties, we used probability distribution functions to infer a mass $M = 1.05 \pm 0.01$ $M_\odot$ and age of 5.9 ± 0.4 Gyr (Fig. 3.6), which are similar to those reported by Ramírez et al. (2014b), 1.04 ± 0.01 $M_\odot$ and $5.2^{+0.4}_{-0.5}$ Gyr.

Recently, Nissen (2015) has shown a tight correlation between [Y/Mg] and age that is corroborated by our own study (Tucci Maia et al., 2016). HIP68468 has $[Y/Mg] = -0.087 \pm 0.017$ dex, implying in an age of 6.4 ± 0.8 Gyr (using the relation by Tucci Maia et al., 2016). This age agrees well with our isochrone age (5.9 ± 0.4 Gyr). Thus, both isochrones and [Y/Mg] suggest that HIP68468 has an age of about 6 Gyr.

The post-solar age of HIP68468 is further supported by its low activity level. The HARPS spectra give an activity index $\log(R'_{HK})$ = -5.05 ± 0.02, where the error comes from the standard deviation across all spectra in the time series. Using the relationship derived by Mamajek & Hillenbrand (2008) and a stellar (B-V) of 0.68 (Høg et al., 2000), this translates into an expected age of 7.6 ± 0.4 Gyr, but we note that the activity-age relation is not well defined above 3 Gyr (Ramírez et al., 2014b), hence the above error bar is underestimated.

The projected rotational velocity of HIP68468 was estimated through spectral synthesis by dos Santos et al. (2016), taking into account both the instrumental ($\Delta\lambda = \lambda/R$) and macroturbulent broadening (using a radial-tangential macroturbulence profile; Gray, 2005).

We note that if the macroturbulence ($V_{\rm macro}$) is estimated from $V_{\rm macro}$-$T_{\rm eff}$relations (e.g., Meléndez et al., 2012), then HIP68468 seems to be rotating faster than it should for its age, when compared to other solar twins analysed with the same method. However, even for main-

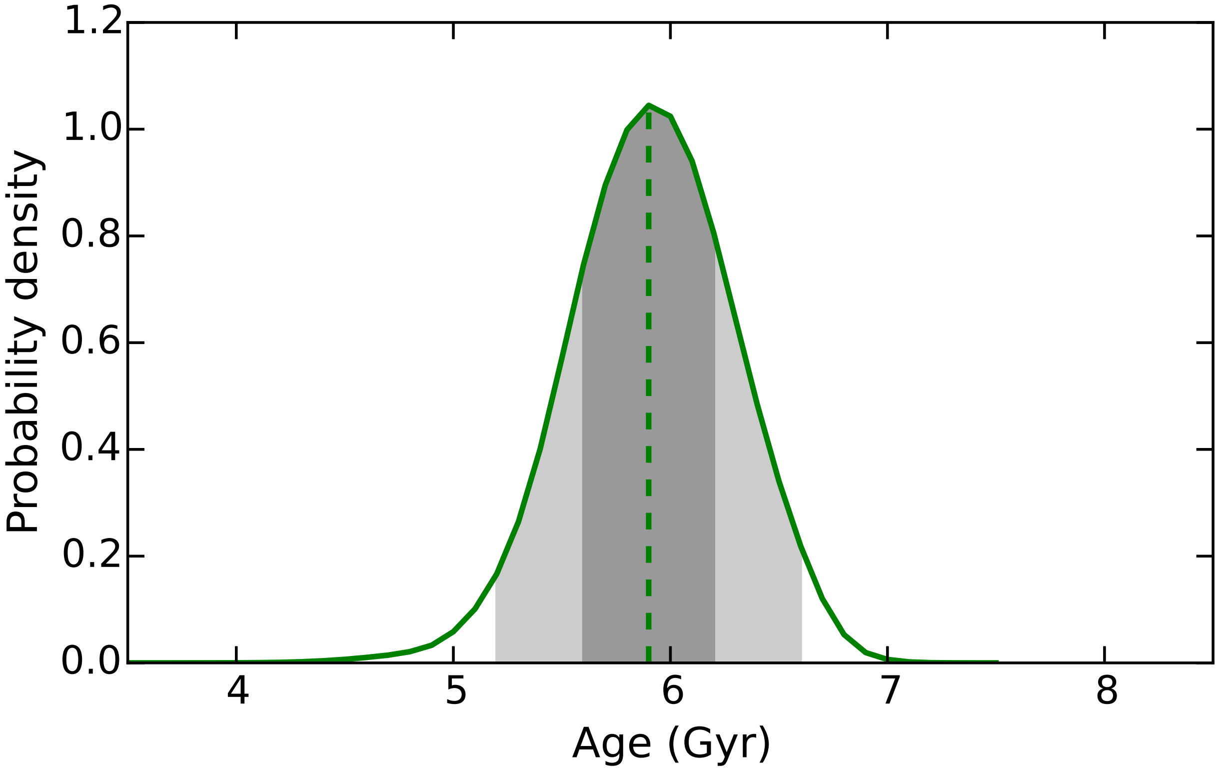

Figure 3.6 Age probability distribution of HIP68468. The dark and light areas correspond to 1σ and 2σ confidence.

sequence stars the luminosity effect on macroturbulence is not negligible (Doyle et al., 2014). dos Santos et al. (2016) provided a new macroturbulence calibration that takes the $T_{\rm eff}$ and log g dependence into account. This gives a projected rotation velocity for HIP68468 of v sin i = 1.92±0.13 km s^{-1} (dos Santos et al., 2016), which agrees within the errors with the rotation velocity predicted by the $v_{\rm rot}$-age relation by dos Santos et al. (2016) at HIP68468's age (5.9 Gyr), $v_{\rm rot}$ = 1.86 km s^{-1}.

3.2.3 Stellar abundances

The chemical composition was determined using the line list by Meléndez et al. (2014b) for atomic lines. To verify the carbon abundances obtained from permitted atomic lines, we also obtained differential abundances using the molecules CH and C_2, adopting the molecular data given in Asplund et al. (2005).

For the elements V, Mn, Co and Cu, we took hyperfine structure (HFS) into account. The differential HFS corrections are small because of the similarity between HIP68468 and the Sun. Differential NLTE corrections in solar twins are also usually small, as shown in our previous works (Meléndez et al., 2012, 2014b; Monroe et al., 2013). Still, we performed NLTE corrections for Li (Lind et al., 2009), O (Ramírez et al., 2007), Na (Lind et al., 2011), Mg, Ca (Lind et al., in prep., see appendix A), and Cu (Shi et al., 2014; Yan et al., 2015). The differential NLTE corrections are small for most elements, amounting to −0.004, −0.006, −0.004 and 0.000 dex for Na, Mg, Ca, and Cu, respectively. Only for the oxygen triplet was the differential NLTE effect strong, amounting to −0.028 dex.

The final differential abundances, after taking into account HFS and NLTE effects, are listed in Table 3.3, where LTE abundances are also shown for completeness. These abundances are plotted as a function of condensation temperature in Fig. 3.7. The upper panel) shows the excellent agreement between neutral and ionised species (shown by triangles) for the elements Cr, Fe (forced by the analysis), Ti, and Sc. The carbon abundance obtained from neutral carbon atomic lines and those obtained from CH and C_2 lines (both shown by triangles in Fig. 3.7) also agree well. This consistency supports our determination of stellar parameters, as lines from different species have different dependence on the stellar parameters.

The abundance errors are reported in Table 3.3 and are based on the measurement errors (standard error) and systematic errors due to the uncertainties in the stellar parameters. The total errors are on average 0.012 dex. This is similar to the 0.01 dex errors achieved with high-quality spectra of stellar twins (e.g. Meléndez et al., 2012; Monroe et al., 2013; Bedell et al., 2014; Ramírez et al., 2015; Teske et al., 2016a).

The lithium feature is clearly visible and deeper than in the Sun, so that a reliable lithium abundance can be estimated. The Li content was obtained using spectral synthesis in LTE, including blends by atomic and molecular (CN, C_2) lines, employing the line list of Meléndez et al. (2012). Using the MIKE spectrum, we obtain an LTE lithium abundance of

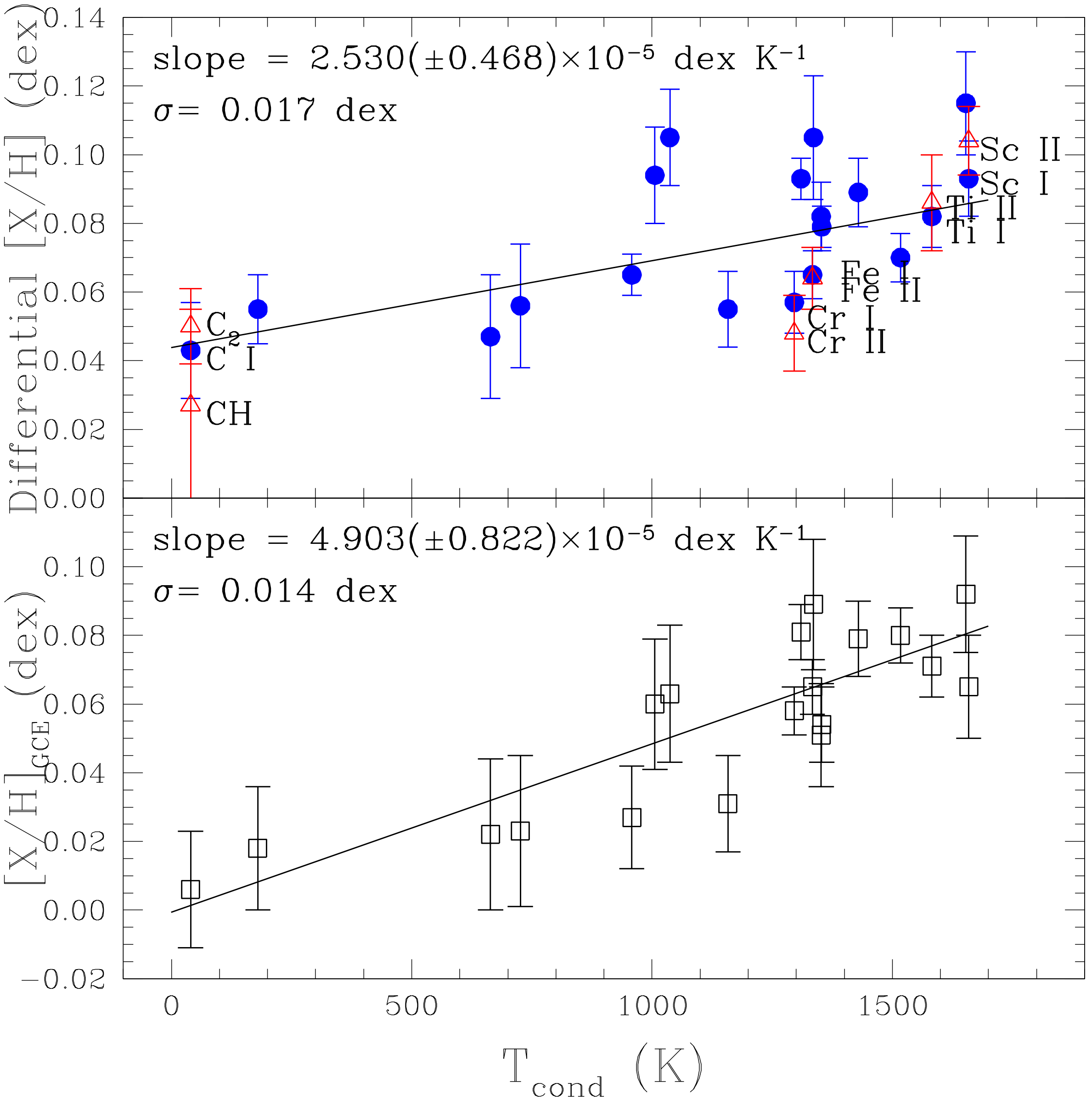

Figure 3.7 *Upper panel:*. Observed abundance pattern of HIP68468 versus condensation temperature before GCE corrections. The solid line is a fit taking into account the total error bars. It has a significance of 5.4-σ, and the element-to-element scatter from the fit is 0.017 dex, which is larger than the average error bar (0.012 dex). *Lower panel:*. Abundance pattern after GCE corrections to the solar age. The error bars also include the error of the GCE corrections, and has an average of 0.014 dex. The correlation with condensation temperature is now stronger and more significant (6.0-σ), and the element-to-element scatter about the fit (0.014 dex) is in perfect agreement with the average error bar.

A(Li) = 1.49±0.05, and our HARPS spectrum results in A(Li) = 1.47±0.04 (Fig. 3.8). We adopted an LTE abundance of A(Li) = 1.48±0.03 (weighted average), and using the NLTE corrections mentioned above (Lind et al., 2009), A(Li) = 1.52±0.03 was obtained.

The Li abundance in HIP68468 (1.52±0.03 dex) is much higher (four times; 0.6 dex) than expected for its age (Monroe et al., 2013; Meléndez et al., 2014a; Carlos et al., 2016). This is shown in Fig. 3.9, where HIP68468 is compared with solar twins analysed in our previous works (Ramírez et al., 2011; Meléndez et al., 2012, 2014b,a; Monroe et al., 2013; Carlos et al., 2016; Galarza et al., 2016b) and to solar twins in open clusters using data by Baumann et al. (2010), except for the cluster M67, where the Li abundances are from the updated results using spectrum synthesis by Castro et al. (2011). The solar twins in M67 were selected from their list of solar analogs (Table 1), considering $T_{\rm eff} = T_{\rm eff\odot} \pm 100$K and $L = 1.0 \pm 0.1\ L_\odot$. The mean LTE Li abundance in M67 solar twins is 1.25 (σ = 0.35 dex), with the scatter being due partly to the uncertain values (some are only upper limits) given in Castro et al. (2011). Nevertheless, the mean Li abundance is similar to the LTE Li abundance (1.26 dex) of the only solar twin (M67-1194) analysed at high precision in this cluster (Önehag et al., 2011). Although there might be some slight variations in Li as a result of slightly different masses and metallicities, contributing thus to the observed scatter in the Li-age correlation, the variations for our small range in mass and metallicity are small (Baumann et al., 2010; Carlos et al., 2016), hence our comparison between HIP68468 and other solar twins is valid.

The decay of lithium with age is supported by stellar evolution models including transport processes beyond merely the mixing length convection (Charbonnel & Talon, 2005; Do Nascimento et al., 2009; Xiong & Deng, 2009; Denissenkov, 2010), as shown in Fig. 3.9. Lithium is depleted and not produced in stars like the Sun, therefore the enhanced lithium abundance of HIP68468 is probably due to external pollution. Carlos et al. (2016) have also recently identified two stars with enhanced lithium abundances (open squares in Fig. 3.9) and suggested that they may have been polluted in lithium by planet ingestion, which might also be the case of 16 Cyg A (open triangle in Fig. 3.9).

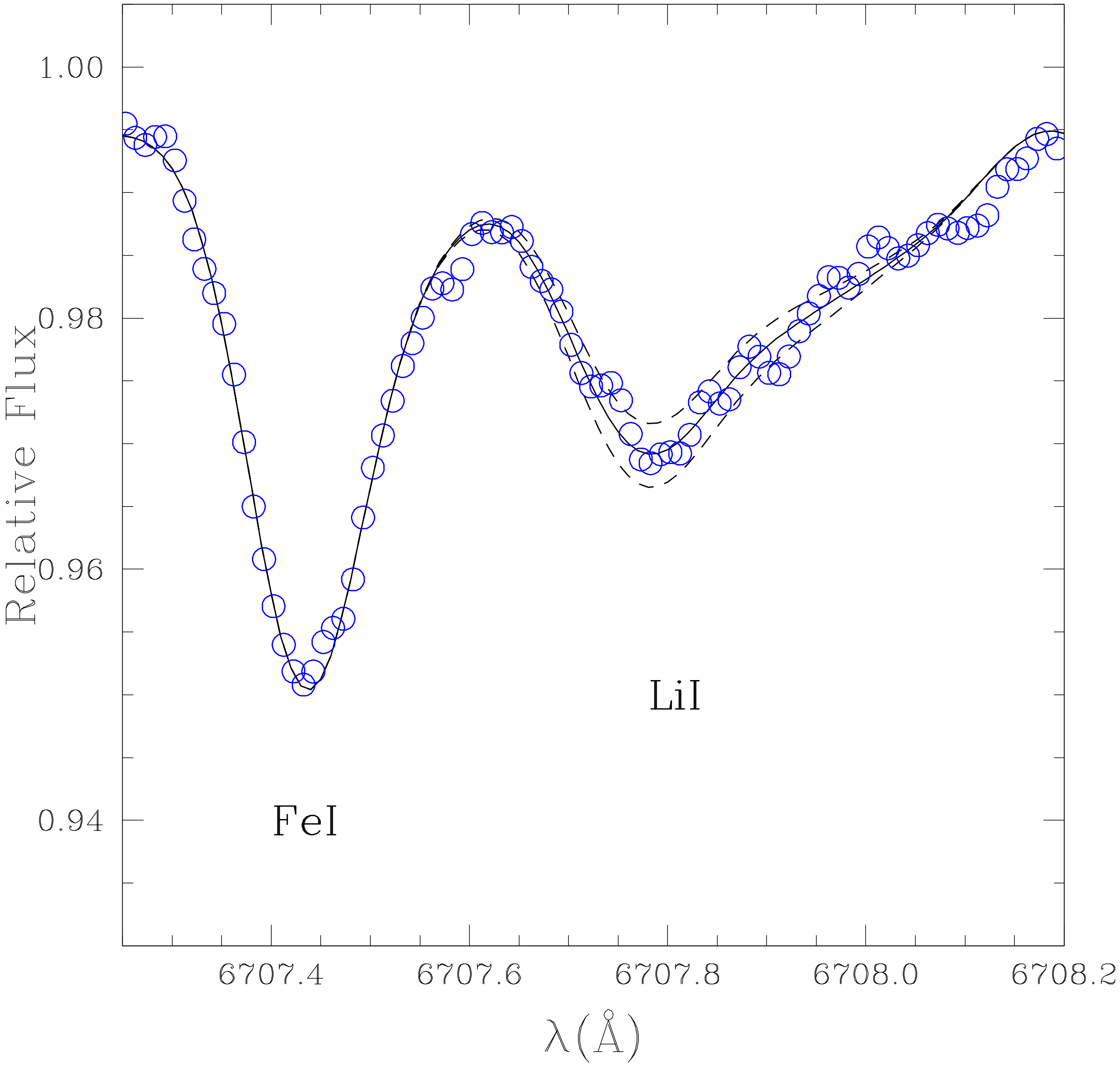

Figure 3.8 Lithium feature in the HARPS spectrum of HIP68468 (open circles) and synthetic spectrum with an LTE lithium abundance of 1.47 dex (solid line), corresponding to an NLTE abundance of A(Li) = 1.51 dex. A variation of ±0.04 dex in the Li abundance is shown by dashed lines. The variations seen in the line profile are mostly consistent with the noise in this region (S/N ∼ 500), but could also be due to distinct convective line shifts between different species.

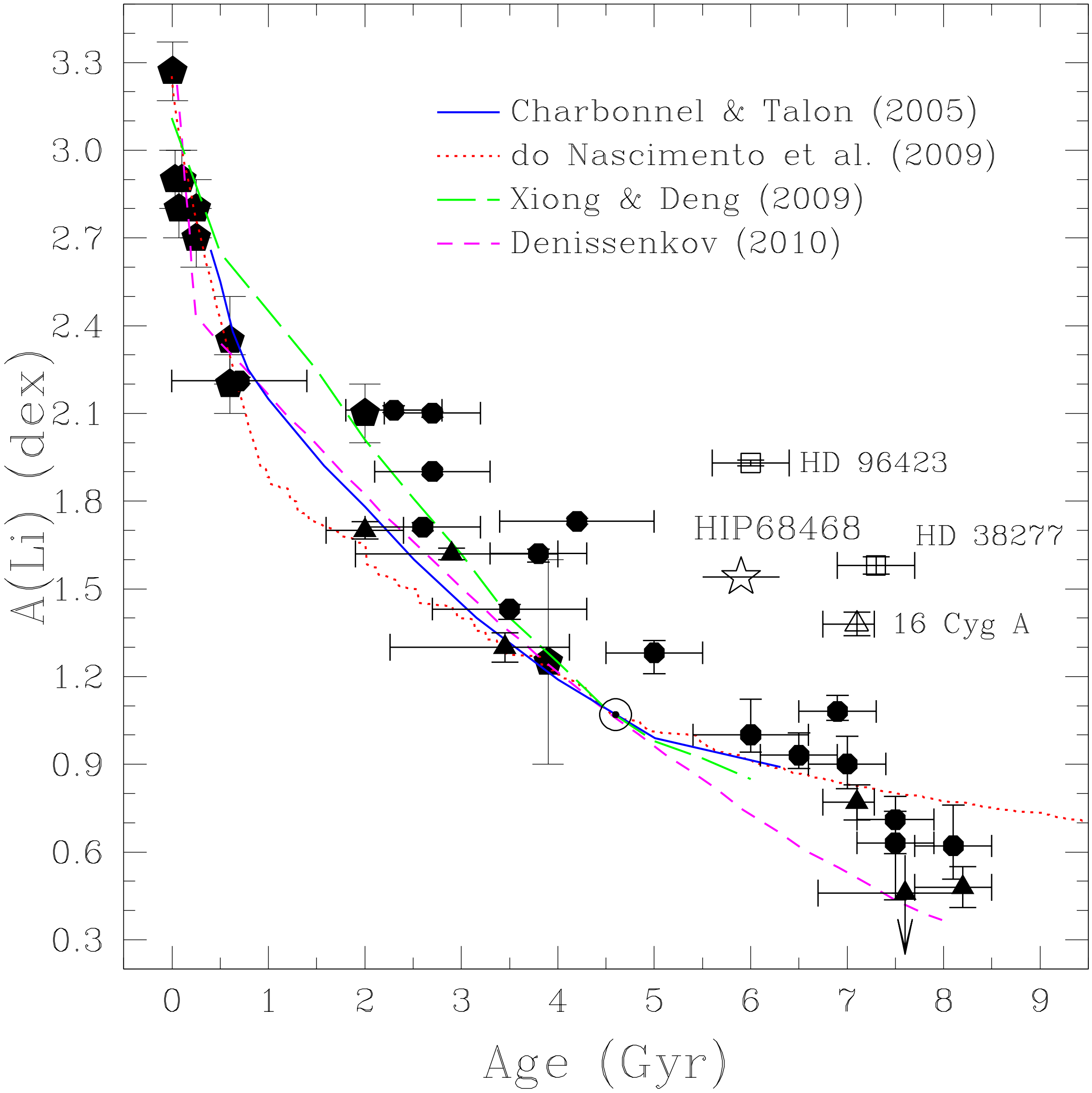

Figure 3.9 Lithium abundances versus age. The Li abundance of HIP68468 was determined in this work. For the field solar twins (circles, triangles, squares) we used the values given in our previous works (Carlos et al., 2016; Galarza et al., 2016b; Meléndez et al., 2012, 2014b,a; Monroe et al., 2013; Ramírez et al., 2011), and for the solar twins in open clusters (pentagons) we adopted the values given in Baumann et al. (2010) and Castro et al. (2011), as described in the text. We also show non-standard models of lithium depletion (Charbonnel & Talon, 2005; Do Nascimento et al., 2009; Xiong & Deng, 2009; Denissenkov, 2010), normalised to the Sun.

There are four stars with enhanced lithium abundances in the sample of 27 thin-disc solar twins shown in Fig. 3.9 (HIP68468, HD 38277, HD 96423, 16 Cyg A). Adopting a binomial distribution (see e.g. Sect. 4.4 in Ramírez et al., 2012b), the above numbers suggest that 15±2% of Sun-like stars may have visible signatures of planet ingestion.

3.3 Discussion

The presence of a giant planet and a small super-Earth in close-in orbits gives us the opportunity to study how this configuration might be related to the chemical abundance pattern in HIP68468.

In Fig. 3.7 (upper panel) we show that the abundance pattern of HIP68468 (relative to the Sun) has a correlation with condensation temperature ($T_{\rm cond}$). The fit of [X/H] vs. $T_{\rm cond}$ is represented by a solid line. This correlation is well defined, with a significance higher than 5-σ. The element-to-element scatter about the fit is 0.017 dex, which is higher than the average abundance error of 0.012 dex, but this is likely due to the scatter introduced by galactic chemical evolution (GCE), as described in recent works (Nissen, 2015; Spina et al., 2016b).

Employing the relations between age and stellar abundances obtained by Spina et al. (2016b) using solar twins, we can correct for GCE effects, which enables a more proper comparison to the Sun, which is $\Delta_{\rm age}$ = 1.3 Gyr younger than HIP68468. We subtracted the GCE effects corresponding to this age interval, resulting in abundance ratios corrected to the Sun's age,

$$[X/H]_{\rm GCE} = [X/H] - slope * \Delta_{\rm age}, \tag{3.1}$$

where the slope of the GCE corrections for the different chemical elements is taken from Table 3 of Spina et al. (2016b).

The corrected abundance ratios are shown in the bottom panel of Fig. 3.7. In this plot

Table 3.3 Differential abundances of HIP68468 relative to the Sun.

Element	[X/H]	Δ $T_{\rm eff}$	Δlog g	Δv_t	Δ[Fe/H]	param[a]	obs[b]	total[c]
		±8K	±0.02dex	±0.01 km s^{-1}	±0.01 dex			
	(dex)	(dex)	(dex)	(dex)	(dex)	(dex)	(dex)	(dex)
Li[d]	1.52[e]	0.01	0.00	0.00	0.00	0.01	0.03	0.03
C	0.043	-0.005	0.005	0.000	0.000	0.007	0.012	0.014
CH	0.027	0.006	-0.001	0.000	0.007	0.009	0.026	0.028
C_2	0.050	0.007	0.001	0.000	0.007	0.010	0.005	0.011
O[d]	0.055	-0.008	0.003	-0.001	0.002	0.009	0.005	0.010
Na[d]	0.065	0.003	-0.001	0.000	0.000	0.003	0.002	0.006
Mg[d]	0.105	0.006	-0.002	-0.003	0.000	0.007	0.017	0.018
Al	0.115	0.003	-0.002	-0.001	0.000	0.004	0.015	0.015
Si	0.093	0.001	0.001	-0.001	0.001	0.002	0.006	0.006
S	0.047	-0.004	0.005	0.000	0.001	0.006	0.017	0.018
K	0.094	0.006	-0.008	-0.002	0.001	0.010	0.009	0.014
Ca[d]	0.070	0.005	-0.003	-0.002	0.000	0.006	0.003	0.007
Sc I	0.093	0.006	0.000	0.000	-0.001	0.006	0.009	0.011
Sc II	0.104	0.000	0.007	-0.002	0.003	0.008	0.006	0.010
Ti I	0.082	0.007	0.000	-0.002	-0.001	0.007	0.006	0.009
Ti II	0.086	0.000	0.007	-0.002	0.003	0.008	0.011	0.014
V[f]	0.089	0.008	0.000	-0.001	-0.001	0.008	0.005	0.010
Cr I	0.057	0.006	-0.001	-0.002	0.000	0.006	0.006	0.009
Cr II	0.048	-0.003	0.007	-0.002	0.002	0.008	0.008	0.011
Mn[f]	0.055	0.006	-0.002	-0.003	0.000	0.007	0.008	0.011
Fe I	0.065	0.006	-0.001	-0.002	0.000	0.006	0.002	0.007
Fe II	0.064	-0.002	0.007	-0.003	0.003	0.008	0.004	0.009
Co[f]	0.082	0.006	0.002	0.000	0.000	0.006	0.008	0.010
Ni	0.079	0.005	0.000	-0.002	0.000	0.005	0.003	0.006
Cu[d,f]	0.105	0.004	0.001	-0.001	0.001	0.004	0.013	0.014
Zn	0.056	0.000	0.001	-0.003	0.002	0.004	0.018	0.018

[a] Adding errors in stellar parameters

[b] Observational errors

[c] Total error (stellar parameters and observational)

[d] NLTE effects were considered for Li, O, Na, Mg, Ca, and Cu; LTE abundances for these elements are 1.48, 0.083, 0.069, 0.099, 0.075, 0.105 dex, respectively

[e] A(Li) is reported rather than [Li/H].

[f] Abundances accounted for HFS.

the elements with different species were weight averaged, using as weights the inverse square of their error bars. The error bars now also include the error on the GCE corrections, which are due to the error on the slope of the abundance variations with age (Spina et al., 2016b) and also considering the error on the age of HIP68468. As a result, the typical error bar increased from 0.012 dex to 0.014 dex. The $[X/H]_{GCE}$ ratios now show a higher refractory enhancement and a stronger correlation with T_{cond}, at the level of 6-σ. The scatter about the fit is now 0.014 dex, identical to the typical error bar in the $[X/H]_{GCE}$ ratios.

The close-in giant planet suggests migration from an outer to the inner (≤ 1 AU) region. This migration could have driven inner planets towards its host star, leading to planet engulfment events and to changes in the abundance pattern of the convection zone (Sandquist et al., 2002). The super-Earth that we seem to have detected may also follow this fate, as it is located at only 0.03 AU from HIP68468. If HIP68468b survives, it surely would be destroyed when HIP68468 evolves from the main sequence.

Past planet accretion effects could be reflected in enhanced abundances of the refractory elements, and also an increase in the lithium abundance. As lithium is affected by stellar depletion by more than a factor of 100 at the solar age (e.g. Asplund et al., 2009; Monroe et al., 2013), it is relatively easy to increase the low photospheric Li content by planet accretion. As shown by Sandquist et al. (2002), in a planet migration scenario and further accretion to its host star, the planet material would be mixed in the stellar convection zone and would modify the surface abundances, in particular for Li (see also Tognelli et al., 2016; Murray & Chaboyer, 2002; Montalbán & Rebolo, 2002).

Using the abundance pattern of the Earth and meteorites, we can estimate the rocky mass needed to increase the refractory elements to the levels observed in HIP68468, following the procedure outlined in Chambers (2010) and Galarza et al. (2016a). We estimated a convective mass of 0.018 $M_{\odot}$, using the tracks by Siess et al. (2000). In Fig. 3.10, we show the $[X/H]_{GCE}$ ratios by red circles and the effect due to the accretion of 6 Earth masses of rocky material into the convection zone of HIP68468 by blue triangles. The best fit is provided with a mix of two and four Earth masses of meteoritic-like and Earth-like material, respectively.

The same amount of rocky material (6 Earth masses) is more than enough to explain its Li enhancement. The net lithium enhancement is hard to predict because it depends on *(i)* the initial stellar lithium content at the time of accretion, *(ii)* the stellar Li depletion since the planet accretion, *(iii)* the efficiency of thermohaline instabilities for depletion of Li that is due to the planet engulfment (Théado & Vauclair, 2012). For example, if there is no extra depletion that is due to thermohaline mixing, then we find that the planet accretion event could have occurred when the star had A(Li) $\sim$ 2 dex, corresponding to an age of about 1 Gyr. Assuming that thermohaline mixing depletes lithium by 0.5 dex or 1.0 dex, then the initial Li at the time of planet accretion was either 1.45 dex or 0.9 dex, corresponding to ages of about 3 or 6 Gyr, respectively. This means that if thermohaline mixing is very efficient, depleting Li in about 1 dex, then the planet accretion event occurred recently.

If accretion of planetary material occurred in recent times, then debris may remain around the star. The low log(R'$_{HK}$) activity index of HIP68468, while not obviously anomalous for its age group, might in part be due to absorption by dust in the chromospheric Ca II lines similar to the effect seen in WASP-12 (Haswell et al., 2012; Fossati et al., 2013). Further observations including photometric monitoring for anomalously shaped transits of dust clouds would test this hypothesis. Although the activity index might be affected by the dust, the stellar activity as traced by the RVs would not. The low RV jitter is therefore consistent with the old age and low log(R'$_{HK}$).

Meléndez et al. (2009) and Ramírez et al. (2009) argued that the Sun is deficient in refractory elements relative to the majority solar twins, probably because of the formation of terrestrial planets in the solar system. Most solar twins are therefore enhanced in refractory elements relative to the Sun, such as the solar twin HIP68468. However, it must be stressed that the refractory enhancement of most solar twins may be primordial, unlike the case of HIP68468, where the refractory enrichment seems to be due to planet accretion at least 1

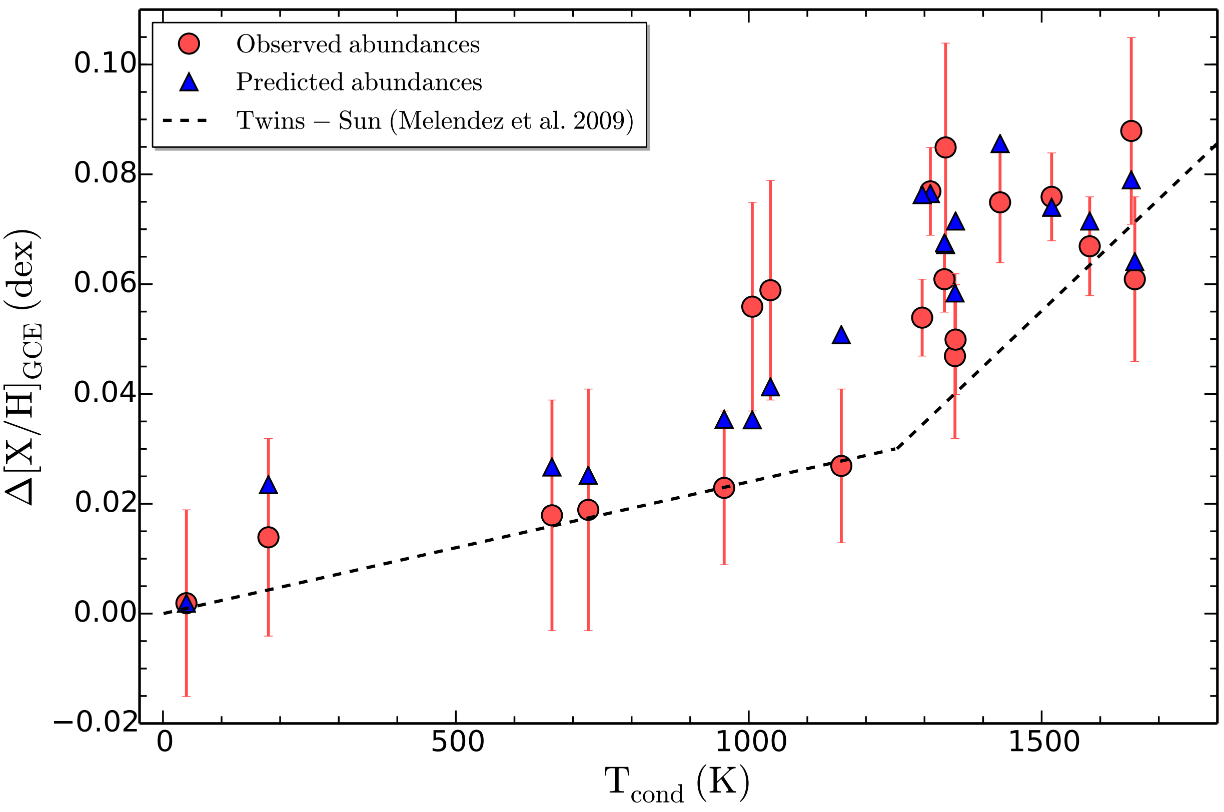

Figure 3.10 Observed abundance ratios $[X/H]_{GCE}$ in HIP68468 as a function of condensation temperature (red circles). The abundances are corrected for galactic chemical evolution to the Sun's age. Planet engulfment of 6 Earth masses of rocky material (blue triangles) can explain the enhancement of refractory elements. The mean abundance trend of 11 solar twins relative to the Sun (Meléndez et al., 2009) is shown by the dashed line.

Gyr after the star was born. This distinction can be made thanks to the enhanced lithium in HIP68468, in contrast to most solar twins, which follow a well-defined Li-age correlation.

3.4 Concluding remarks

We have discovered two strong planet candidates, a close-in (0.66 AU) planet more massive than Neptune and a close-in (0.03 AU) super-Earth, around the solar twin HIP68468. We have recently been granted *Spitzer* time to search for the transit of this super-Earth.

The host star has enhanced abundances of refractory elements relative to the Sun. After corrections for GCE to bring the [X/H] abundance ratios to the solar age, the correlation with condensation temperature is even stronger, and the element-to-element scatter about the fit with $T_{\rm cond}$ is reduced. The lithium content of HIP68468 is four times higher than expected for its age. The enhancement of Li and of the refractories can be reproduced by engulfment of a rocky planet with 6 Earth masses.

The planet configuration of HIP68468 suggests planet migration, which might have resulted in planet accretion events that left signatures on the chemical composition of the host star, as observed for HIP68468, and in agreement with the predictions by Sandquist et al. (2002).

The recent discoveries of stars showing chemical anomalies possibly related to planet engulfment episodes (Ashwell et al., 2005; Spina et al., 2015) and the exciting case of HIP68468 open the possibility to extend the search to other objects with such distinctive chemical patterns. Identifying a population of such objects will provide important indications of dynamical interactions of planets and the mechanisms that can drive the evolution of systems similar to our own.

While the detection of the two planets is formally statistically significant (see Sect. 2.3), secure detection of small planets with the radial velocity technique has typically been based on a substantially larger number of measurements given the challenges of stellar activity and reliable period determination with sparse sampling (e.g. Pepe et al., 2011). The intriguing evidence of planet accretion in the form of the enhanced refractory element and lithium abundances warrants further observations to verify the existence of the planets that are indicated by our data and to better constrain the nature of the planetary system around this unique star.

CHAPTER 4

RESULTS OF THE SOLAR TWIN PLANET SEARCH

In this chapter, we present some overarching results from the five-year-long HARPS program. Beyond the detections of new planets, our program also holds scientific value in its extensive monitoring of a large sample of solar twins. In particular, time-series analysis of the RVs and spectral activity indicators for the sample as a whole enables us to investigate the behavior and evolution of magnetic activity in Sun-like stars.

We begin with a description of the general techniques used for analyzing the HARPS RVs in Section 4.1. Section 4.2 presents some planet candidate signals from the data. In Sections 4.3 and 4.4 we turn to the stellar activity signals in the data: Section 4.3 delves into the multi-year activity cycles seen for some targets, while Section 4.4 examines the RV "jitter" due to shorter-period, often incoherent activity signals. Finally, in Section 4.5 we present a selected sub-sample of the quietest solar twins from our survey which we recommend for future follow-up planet hunting.

4.1 Bulk Sample Analysis

The previous two chapters detailed the analysis techniques used to characterize the orbital elements of planet candidates and verify their validity in the presence of stellar activity. Before these techniques can be applied, however, a considerable amount of analysis must be done to identify the candidate planet signals in the first place. The question of how best to pull planet signals out of a large RV dataset, especially when the target stars vary in observational coverage and intrinsic stellar activity levels, is not a trivial one. In this section we outline our semi-automated procedure for identifying planet candidates for follow-up analysis.

4.1.1 Data

As described in 1.2, efforts were made to observe all stars in our program approximately equally. Due to numerous factors, including seasonal weather patterns and constraints from the timing of assigned observing runs, an exactly equal distribution of RVs among targets was not always possible. Additionally, we obtained extra RVs for many of the targets from the ESO online archive and from the Carnegie Planet Search's Keck/HIRES public data release (Butler et al., 2017).[1] This further affects the spread of available data. A summary of the net number of RVs is given in Table 4.1, including all STPS targets and additional solar twins observed by other HARPS programs and included in our stellar abundance sample. Note that the number of RVs for a given target is not necessarily the same as the number of spectra for the target; RVs are extracted from the spectra and binned in 20-minute intervals in an effort to average out the influence of short-period oscillations in the star. Some of the brightest targets then have 2-4 short-exposure spectra for each RV epoch.

The distribution of RV observations is plotted in Figure 4.1. A few features are worth noting. The HARPS STPS RV distribution is bimodal, with a significant number of stars near zero observations. This is a result of two effects. First, we did not include stars which were already being observed heavily by other HARPS programs in our STPS sample, so that some stars which do possess a number of HARPS RVs in general have zero STPS RVs. Secondly, within the first year of the STPS campaign a handful of targets were dropped from the sample due to extreme RV variability, leaving them with < 10 STPS observations. This was done to maximize the search sensitivity to low-mass planets by enabling us to obtain more observations for the remaining targets.

When HARPS archive data and HIRES data are included in the RV count, a long tail of stars with large numbers of RVs appears in the histogram. Most of these stars, like HIP29432

---

[1] Data were used from ESO programme IDs 072.C-0488, 074.C-0364, 075.C-0202, 075.C-0332, 076.C-0155, 077.C-0364, 089.C-0415, 089.C-0732, 090.C-0421, 091.C-0034, 091.C-0936, 092.C-0721, 093.C-0409, 095.C-0551, 096.C-0499, 097.C-0090, 097.C-0571, 097.C-0948, 183.C-0972, 183.D-0729, 185.D-0056, 188.C-0265, 192.C-0224, 192.C-0852, 289.C-5053, 292.C-5004, and 60.A-9036.

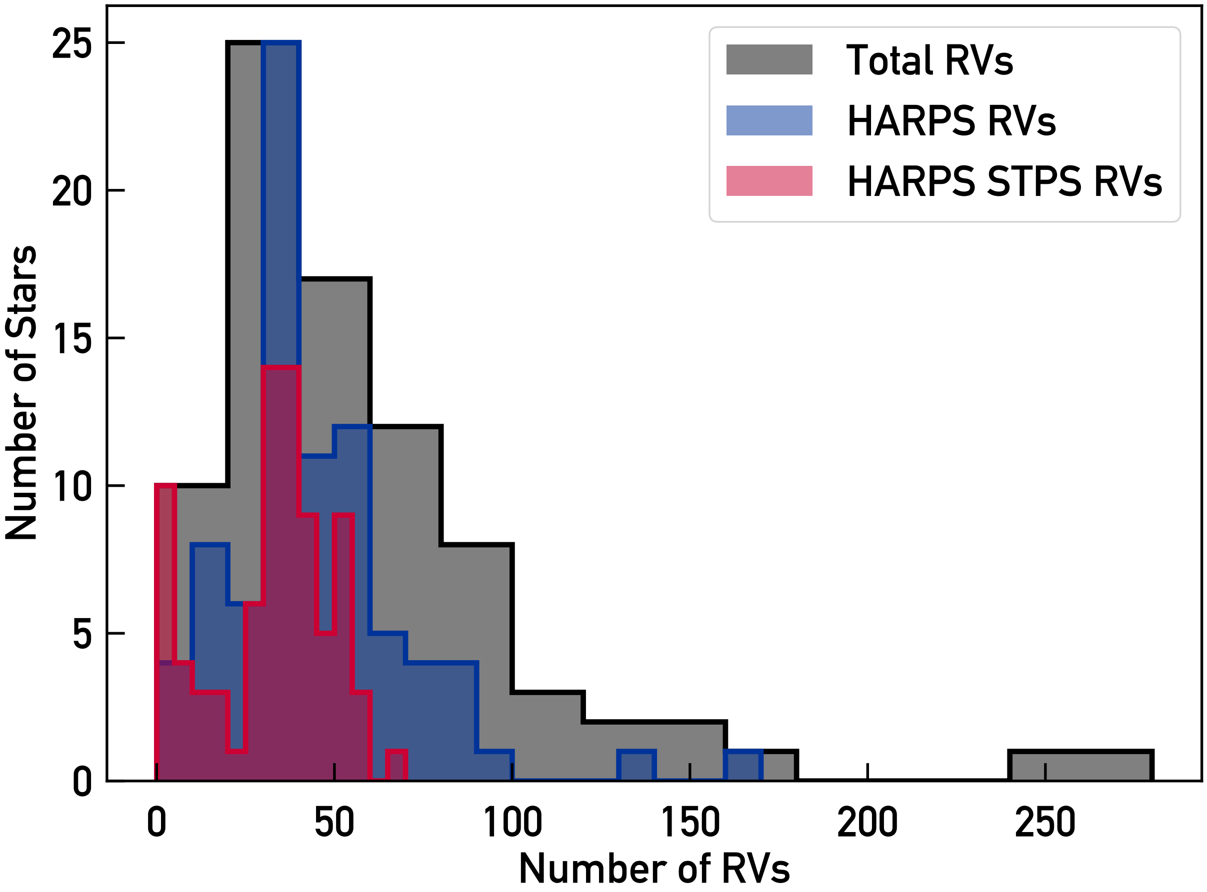

Figure 4.1 Histogram of the number of RVs obtained for each solar twin target. The total available RVs including both HARPS and HIRES data are plotted in black. HARPS RVs from all programs are in blue, and HARPS RVs from the Solar Twin Planet Search program only are in red. Note that the histogram bin sizes vary.

and HIP102040, were heavily observed with HIRES. The largest outlier is HIP79672, also called 18 Sco; as the brightest and nearest solar twin, 18 Sco is a well-known target with a large number of observations in all three categories. 18 Sco has additionally been asteroseismically characterized with HARPS, adding thousands of short-exposure spectra to the archive data (Bazot et al., 2011). We chose to bin these RVs by two-hour time intervals to avoid weighting the data from the asteroseismic observing nights too heavily. We do note some long-term trends in the asteroseismic data at the $\sim$ m s^{-1}level which appear to repeat nightly, which may be either a long-period stellar oscillation or an instrumental drift effect.

Table 4.1: Summary of Solar Twin Observations

HIP	HD	M_V	RA	Dec	Number of RVs[a]			Notes
			(deg)	(deg)	HARPS STPS	HARPS archive	HIRES	
1954	2071	7.27	6.17641401	-53.98392868	52	35		
3203	3821A	7.02	10.19784260	-7.23238325	33			
4909	6204	8.52	15.73924637	-9.86127853	35	7		
5301	6718	8.45	16.95228958	-8.23375130		38		planet detected (Naef et al., 2010)
6407	8291	8.61	20.57790184	3.51348710	7			SB1, P = 5.1 yr
7585	9986	6.77	24.42003059	12.07836628	41	2	99	
8507	11195	8.89	27.42875099	-18.93609810	54			
9349	12264	7.99	30.02211761	-13.54606247	33			
10175	13357	7.63	32.71671677	13.68345356	51		11	
10303	13612B	7.56	33.19344330	-2.39617085	56		26	wide binary
11915	16008	8.61	38.45370483	-19.61189079	53	18		planet detected; see Chapter 2
14501	19467	6.97	46.82741547	-13.76114941	50	24	42	wide SB1, T dwarf companion
14614	19518	7.85	47.18443298	15.33530045	28	5		
15527	20782	7.36	50.01393890	-28.85391426		80		planet detected (Jones et al., 2006)
18844	25874	6.74	60.61065674	-61.35720444	17			wide SB1
19911	26990	7.50	64.06894684	7.15956831	7		25	SB1 (possibly SB2), P = 5.7 yr
22263	30495	5.49	71.90088654	-16.93486786	44			

---

a. Note: HARPS values are the number of usable RV measurements after binning over short periods and discarding poor quality data; number of spectra may be larger.

Table 4.1 continued.

HIP	HD	M_V	RA (deg)	Dec (deg)	Number of RVs HARPS STPS	HARPS archive	HIRES	Notes
25670	36152	8.27	82.24658203	-17.42905807	57	2		
28066	39881	6.60	89.01336670	13.92608833	43		44	
29432	42618	6.85	93.00187683	6.78369045	47	3	202	
29525	42807	6.43	93.30190277	10.62786579		16		
30037	45021	9.16	94.81251526	-68.83158112	27			SB1, P = 31.6 d
30158	44665	8.37	95.19450378	-44.78936768	39			
30476	45289	6.67	96.10171509	-42.84940720	37	29		
30502	45346	8.66	96.18231964	-43.40587616	39	1		
33094	50806	6.05	103.39064789	-28.53872108		38		
34511	54351	8.00	107.27104950	15.42228508	31	3		
36512	59711	7.73	112.66660309	-15.99432182	39	28		
36515	59967	6.66	112.67739868	-37.33949280		10		
38072	63487	9.20	117.02509308	-27.51971245	27			
40133	68168	7.34	122.95505524	16.52449036	38		23	
41317	71334	7.81	126.45592499	-29.92988205	37	28	31	
42333	73350	6.74	129.46028137	-6.80699015	19			
43297	75302	7.45	132.30256653	3.48461103	32			wide SB1
44713	78429	7.31	136.66163635	-43.49241257		83		
44935	78534	8.72	137.29275513	10.82209492	30	1		
44997	78660	8.34	137.47486877	14.45670223	28	7		

Table 4.1 continued.

HIP	HD	M_V	RA	Dec	Number of RVs			Notes
			(deg)	(deg)	HARPS STPS	HARPS archive	HIRES	
49756	88072	7.55	152.34811401	2.37110090	35	7	24	
54102	96116	8.65	166.05673218	-57.76504135	31	8		wide SB1
54287	96423	7.23	166.58197021	-44.37310791	44	31		wide SB1
54582	97037	6.81	167.55618286	-7.38898468	36	30		
62039	110537	7.83	190.74772644	-4.04889345	34	5	63	wide SB1
64150	114174	6.78	197.21238708	5.20886946	36		56	wide SB1, WD companion
64673	115031	8.33	198.83645630	-55.34126282	38			
64713	115169	9.26	198.94775391	-29.50568581	30	1		
65708	117126	7.44	202.07740784	-0.83920324	10			SB1, P = 207 d
67620	120690	6.43	207.83624268	-24.38977242	12			SB1 (possibly SB2), P = 10.4 yr
68468	122194	9.39	210.26539612	-32.75666046	55			planets detected; see Chapter 3
69645	124523	9.41	213.81330872	-42.80474091	37			
72043	129814	7.52	221.04890442	18.46246719	34		21	wide SB1
73241	131923	6.34	224.53672791	-48.86219406	15			
73815	133600	8.18	226.30520630	6.29051256	33	5		
74389	134664	7.76	228.04286194	-30.88603592		33		
74432	135101	6.69	228.18270874	19.28532600	34		41	
76114	138573	7.22	233.18190002	10.96791363	32			
77052	140538	5.86	236.00769043	2.51552510	26	5	93	
77883	142331	8.72	238.58271790	-8.58032322	38	8		

Table 4.1 continued.

HIP	HD	M_V	RA	Dec	Number of RVs			Notes
			(deg)	(deg)	HARPS STPS	HARPS archive	HIRES	
79578	145825	6.55	243.54994202	-31.66303635	26			SB1, P = 18 yr
79672	146233	5.49	243.90472412	-8.36823654	47	116	104	asteroseismic target
79715	145927	8.35	244.02720642	-52.81452560	43	4		
81746	150248	7.03	250.45727539	-45.36849976	13			SB1, P = 8.9 yr
83276	153631	7.12	255.29486084	-13.56634331	7			
85042	157347	6.28	260.71359253	-2.38791442	42	48	78	
87769	163441	8.43	268.93893433	11.80400276	33			wide SB1
89650	167060	8.93	274.43347168	-61.70843124	50	3		
95962	183658	7.27	292.72000122	-6.51408005	43	38	25	
96160	183579	8.67	293.28536987	-54.53216934	51			
101905	196390	7.33	309.76104736	-49.33145905	44	6		
102040	197076A	6.43	310.18777466	19.93477821	33	6	116	
102152	197027	9.18	310.47717285	-27.21591187	68	1		
103983	200565	8.39	316.02389526	3.98105693	9		33	SB1, P = 28 yr
104045	200633	8.34	316.18429565	-4.82842398	36	5		
105184	202628	6.75	319.61282349	-43.33470154	47	7		
108158	207700	7.43	328.69000244	-73.43741608		21		
108468	208704	7.16	329.60128784	-12.66480827	45	26		
109821	210918	6.23	333.65921021	-41.37974167		54		
114328	218544	8.73	347.31925317	-40.99119978	24			

Table 4.1 continued.

HIP	HD	M_V	RA	Dec	Number of RVs			Notes
			(deg)	(deg)	HARPS STPS	HARPS archive	HIRES	
114615	219057	9.60	348.29086304	-30.44977188	53			
115577	220507	7.59	351.17553711	-52.70149612	51	79		
116906	222582	7.68	355.46505737	-5.98548698		29		planet/BD detected (Vogt et al., 2000)
117367	223238	7.69	356.96749878	4.17555332	44		36	
118115	224383	7.89	359.38851929	-9.64716339	46		20	

4.1.2 Procedure

Given a set of time series, how do we carry out an unbiased, semi-automated analysis to see which targets may have companions or display signatures of activity? For this part of the analysis we chose to focus solely on the HARPS RVs for several reasons. The HARPS data are in general higher quality with a greater instrumental stability for RVs. Also, the HARPS data carry multiple robust measurements of activity: for every spectrum, the pipeline provides bisector inverse span (BIS) and full width at half-maximum (FWHM) of the cross-correlation function, which reveal spectral line deformations characteristic of stellar activity (see e.g. Queloz et al., 2001; Figueira et al., 2013). Additionally, we measured the calcium index S_{HK} from the spectra following the procedure outlined in Lovis et al. (2011). While the Keck data nominally include S_{HK} measurements, their reliability is debated given the discrepancies in S_{HK} time series measured by different groups from the same spectra (see the example of HD154345 in Wright, 2016; Butler et al., 2017), and no other activity indicators are available from HIRES. Finally, adding data from multiple instruments increases the complexity of fitting the data since the instrumental zero-points are not equal.

With the HARPS time series of RVs and activity indices for each of the 82 stars in Table 4.1, we perform an automated analysis as follows:

1. Remove any potentially bad measurements: if the activity indices S_{HK} , FWHM, or BIS are more than $3\sigma_{RMS}$ discrepant from the average, then mask out this epoch when performing subsequent analysis.[2]

2. For stars flagged by eye as likely binaries, fit and remove a long-period trend from the RVs.

3. Record RMS of the RV time series.

---

[2] While this could be the signature of a stellar flare, for Sun-like stars such events should be rare, making the more likely cause an instrumental or observational issue in the spectrum.

4. Calculate a Pearson correlation coefficient for RV and S_{HK} and its p-value using a bootstrap simulation; if a 3σ significant ($p < 0.003$) linear correlation exists, fit and subtract it from the RVs.

5. Repeat previous step with RV and BIS.

6. Repeat previous step with RV and FWHM.

7. Record RMS of the activity-corrected RVs.

8. Calculate a Lomb-Scargle periodogram of the activity-corrected RVs and record the periods of peaks with an analytically calculated false alarm probability (FAP) below 1% (Zechmeister & Kürster, 2009).

9. If S_{HK} , BIS, or FWHM correlations were found, record the highest periodogram peaks of the correlated index or indices.

The end results (given in Table 4.2) show at a glance the proportion of stars with diagnosable activity in their RVs, the characteristic period(s) of such activity signals, and any promising signals in the activity-cleaned data. We additionally include in Table 4.2 the predicted stellar rotation period based on the star's isochrone age and its $\log(R'_{HK})$ activity level using the relations of Mamajek & Hillenbrand (2008) for easy comparison to the characteristic periodicities seen in the RV and activity data.

The above procedure is by no means exhaustive. For a star with a viable planet candidate, we must perform more robust tests including fitting planets and activity indicator(s) simultaneously and calculating model comparisons (see Chapters 2 and 3). However, as a means of broadly categorizing the types of RV behavior seen within a large sample, this bulk analysis procedure is quick and efficient.

As presented in dos Santos et al. (2017), a number of the solar twins observed with HARPS exhibit RV trends characteristic of SB1 systems. In the automated analysis, we fit and removed these trends with either a linear slope, a second-order polynomial curve, or a

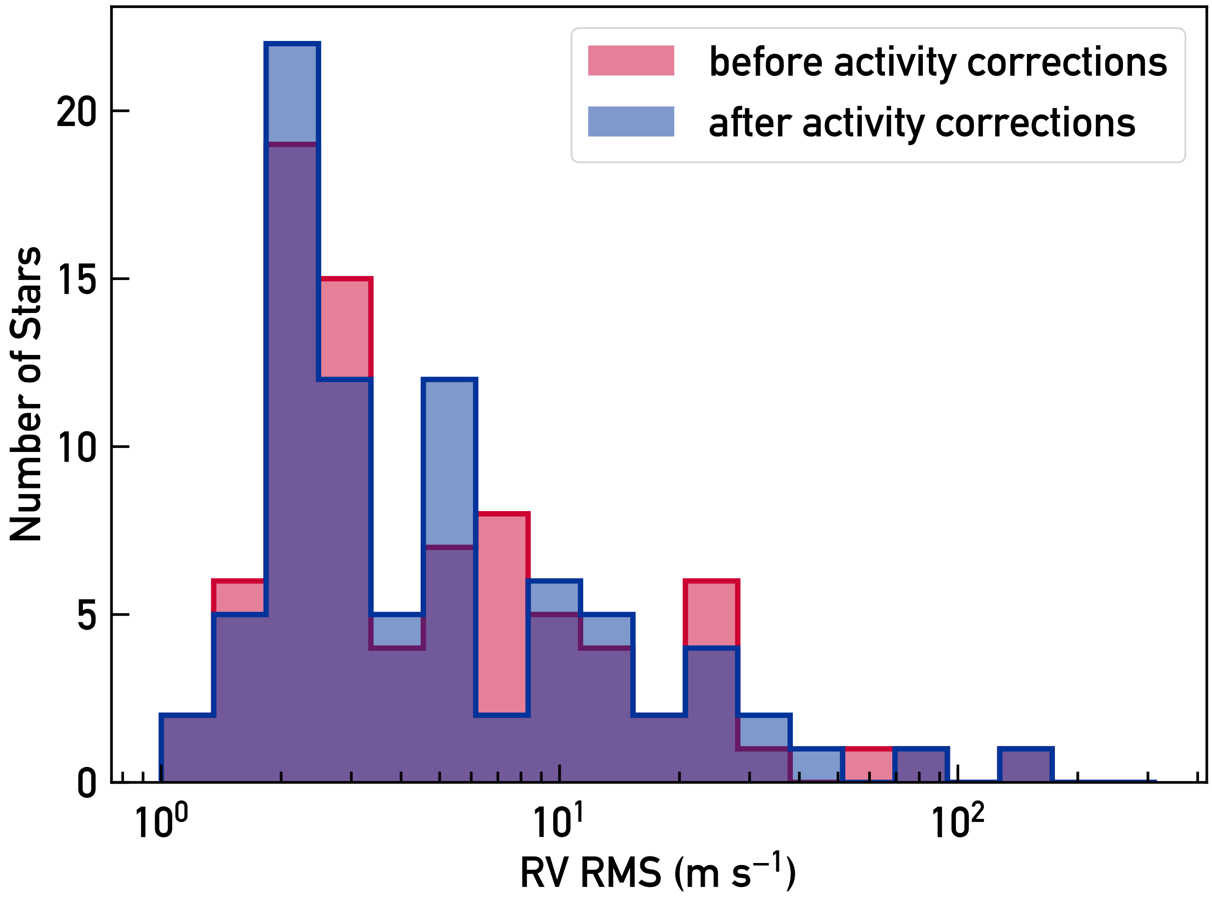

Figure 4.2 RMS of target RVs before (red) and after (blue) fitting and subtracting activity correlations as described in Section 4.1.2. In both cases, bad measurements have been masked and long-term, high-amplitude RV trends have been removed already.

sinusoid. The type of fit used was determined by eye prior to the bulk analysis. Nineteen of the 82 twins were fit for binary trends in this manner. An additional star, HIP30037, was fit with a 31-day Keplerian to remove the 4 km s^{-1} signal from its companion (dos Santos et al., 2017).

The distribution of RV RMS variability across the sample is shown in Figure 4.2. A majority of the sample has RMS < 5 m s^{-1}, indicating a general dearth of both close-in giant planets and strong activity. The lowest RMS stars in the sample have RV dispersions just above 1 m s^{-1}, in keeping with HARPS's superb instrumental stability (Mayor et al., 2003). Fitting and removing activity has a minimal effect on the RMS for the majority of stars, although for a few particularly high-activity stars it does reduce the RMS significantly (see for example HIP3203 or HIP42333). For other stars, though, the automatic application of activity corrections actually increases the RV RMS, indicating perhaps that the linear RV-activity correlation model is not a good fit in these cases. We discuss manifestations of activity further in the following sections.

After binary trends and activity correlations have been removed from the RVs, a whopping 39 of the 82 stars have significant periodogram peaks with FAP at or below 1% . It is possible that all of these signals are planets: both RV surveys and *Kepler* results indicate that approximately half of all Sun-like stars host planets with orbital periods below 100-200 days, and although occurrence rates for longer-period planets are not well-measured such signals can only increase the expected number of planet hosts in the sample (Mayor et al., 2011; Petigura et al., 2013; Silburt et al., 2015). Unfortunately, validating these periodicities as true planet candidates is in general quite tricky, and we are unable to give a robust planet occurrence result with the currently available data. In addition to the two systems detailed in Chapters 2 and 3, we outline a few other promising targets in the following section.

Table 4.2: Bulk RV Analysis Results.

HIP	N_{RV}	Trend	RMS $\mathrm{m\ s^{-1}}$	Activity	RMS_{corr} $\mathrm{m\ s^{-1}}$	Activity peaks (d)	P_1[a] (d)	P_2[b] (d)	RV peaks (d)
1954	86		2.6				26.3	28.0	
3203	32		23.3	bis	14.6	5.70, 3.64	7.7	8.1	
4909	41		15.3	bis	21.1	0.26, 0.20	8.8	10.7	
5301	38		20.8				34.5	31.8	2457.2, 1.0, 1.0, ...
6407	7	linear	5.5				18.5	17.8	
7585	43		6.3	fwhm, bis	16.8	0.33, 0.42, 13.1	22.3	28.0	40.8, 0.3, 81.1, ...
8507	54		2.2	shk	2.1	2319.73, 69.71	27.4	28.5	
9349	33		14.6	shk, bis	12.2	33.90, 19.22, 0.5	9.3	12.5	
10175	48		6.6	fwhm, bis	5.4	1933.88, 1.00, 17.1	21.8	19.6	1.0, 40.6
10303	54		1.5				30.7	33.4	
11915	71		8.0	fwhm	8.6	1478.83, 2991.90	22.8	25.0	2657.3, 10000.0, 1.0, ...
14501	74	linear	1.6	fwhm	1.6	8590.00, 10000.00	39.6	33.7	351.0, 66.4
14614	33	sine	2.0				26.7	28.1	
15527	80		26.2				35.9	29.4	
18844	9	linear	1.1				31.0	34.1	
19911	7	curve	57.8	fwhm	39.3	538.73, 1.00	28.9	12.1	

---

a. Predicted rotation period from stellar age.

b. Predicted rotation period from $\log(R'_{HK})$.

Table 4.2 continued.

HIP	N$_{RV}$	Trend	RMS m s^{-1}	Activity	RMS$_{corr}$ m s^{-1}	Activity peaks (d)	P_1 (d)	P_2 (d)	RV peaks (d)
22263	44		13.7	shk, fwhm	11.6	150.94, 26.11, 0.5	9.5	11.5	70.4, 21.3, 28.5, ...
25670	59		3.0				27.6	30.8	1.0, 34.5, 72.2, ...
28066	43		2.6				38.6	34.1	177.8, 46.1, 27.0, ...
29432	48		2.6	shk	2.4	32.01, 1.03	28.8	27.7	7.8, 1.1, 11.9, ...
29525	16		13.9	bis	8.6	11.95, 7.72	12.8	7.9	149.7, 18.6, 1.0, ...
30037	26	keplerian	2.6				32.4	29.6	
30158	39		1.4				36.4	32.9	
30476	66		1.8	fwhm	2.1	19.29, 170.74	39.3	34.8	0.1, 0.5, 9.0, ...
30502	40		3.1				34.0	32.3	10.1
33094	38		2.6				39.0	37.5	
34511	33		3.0				25.1	31.2	0.9, 18.2, 1.1, ...
36512	67		2.4	bis	2.4	30.36, 66.80	30.8	30.2	
36515	10		13.2	fwhm, bis	7.1	0.34, 1.01, 0.2	7.9	5.2	
38072	27		11.1	shk, bis	10.0	196.94, 61.42, 222.0	12.9	8.4	
40133	33		2.1	shk	2.2	25.84, 42.59	29.3	33.4	
41317	65		2.6				35.9	32.8	88.8
42333	19		21.3	shk, bis	11.4	19.13, 890.01, 0.7	12.4	9.7	
43297	32	sine	11.1				16.0	14.2	65.4
44713	82		4.7	shk, bis	12.5	87.96, 144.48, 21.7	36.0	30.3	10.6, 1.1, 30.7, ...
44935	31		2.0				32.7	33.7	

Table 4.2 continued.

HIP	N$_{RV}$	Trend	RMS m s^{-1}	Activity	RMS$_{corr}$ m s^{-1}	Activity peaks (d)	P_1 (d)	P_2 (d)	RV peaks (d)
44997	36		1.5	shk, bis	1.8	2831.03, 1480.53, 2837.6	32.9	30.1	
49756	40		2.2	fwhm	2.1	10000.00, 1.00	26.4	32.1	
54102	37	sine	6.3	bis	9.0	15.30, 1.07	6.8	16.7	
54287	75		1.3				32.5	34.8	
54582	66	curve	2.5				34.3	34.1	2.2, 13.1, 0.6, ...
62039	39	linear	1.9				32.1	34.6	
64150	36	linear	2.1				32.5	33.6	7.3, 11.2, 0.6, ...
64673	38		2.4				31.2	32.4	
64713	39		2.3				28.9	31.9	
65708	9	sine	71.9	shk	70.9	12.90, 16.06	39.2	35.5	
67620	12	sine	5.1				34.7	18.1	0.5
68468	55		2.3	fwhm	2.3	10000.00, 1.00	29.5	35.9	30.5, 0.3, 32.5
69645	37		2.1				29.0	31.6	
72043	34	sine	10.2				32.2	27.8	69.9, 152.0, 1.0, ...
73241	15	linear	9.1	shk	5.9	22.17, 0.97	39.0	29.8	1.1, 0.3, 0.3, ...
73815	38		2.6	shk, fwhm	2.2	10000.00, 53.61, 5847.6	34.5	33.4	
74389	33		4.2	shk	2.0	1821.49, 10000.00	23.6	25.9	
74432	34		2.3	shk	3.9	72.99, 33.29	38.2	37.1	244.0, 81.3, 0.1, ...
76114	32		5.5				32.8	32.4	58.3, 1.0, 1.0, ...
77052	39		7.1	shk, fwhm, bis	5.6	1440.18, 1280.59, 126.6, 52.2	25.2	20.4	27.3, 15.7, 18.0, ...

Table 4.2 continued.

HIP	N_{RV}	Trend	RMS m s^{-1}	Activity	RMS$_{corr}$ m s^{-1}	Activity peaks (d)	P_1 (d)	P_2 (d)	RV peaks (d)
77883	46		2.3				35.4	32.0	
79578	26	curve	141.6				26.1	21.8	
79715	46		3.7	fwhm	4.6	10000.00, 103.82	31.4	32.8	
79672	163		2.9	shk, fwhm	2.4	924.48, 2581.91, 4769.4	24.9	29.5	182.5, 365.1, 126.7, ...
81746	13	curve	37.3				36.9	33.2	245.9, 305.4, 613.6, ...
83276	7	curve	15.3				32.4	34.9	
85042	89		2.3	shk	3.6	28.66, 38.93	36.1	33.7	9.7, 7.2, 2.7, ...
87769	33	linear	3.7	fwhm	3.7	23.43, 42.29	27.2	31.2	
89650	53		2.8				26.7	33.6	
95962	74		2.8	shk, fwhm, bis	2.5	107.72, 5701.32, 8.4, 4.0	31.2	32.5	
96160	50		4.7	fwhm	4.9	30.96, 13.17	19.2	24.5	0.3, 12.8, 1.1, ...
101905	49		9.9	shk, bis	5.8	2605.80, 10000.00, 5935.8	12.7	19.9	24.5, 26.1
102040	39		2.7				18.6	28.0	39.1, 22.5, 83.4, ...
102152	69		2.8				38.2	33.8	350.2, 1.0, 1.0, ...
103983	9	linear	6.7	shk	6.4	0.40, 0.22	27.7	24.5	
104045	41		5.4				26.5	33.3	2434.7, 3519.3, 1.0
105184	54		7.6	shk	4.3	3836.70, 375.28	9.6	15.6	36.9, 94.6, 61.0, ...
108158	22	linear	1.4				37.0	32.3	
108468	69		3.9	shk, fwhm	3.9	1.00, 0.33, 7507.4	34.1	30.6	24.0, 24.9
109821	54		4.6	bis	5.6	502.19, 445.00	38.9	33.3	10000.0, 53.6, 390.3, ...

Table 4.2 continued.

HIP	N$_{RV}$	Trend	RMS	Activity	RMS$_{corr}$	Activity peaks	P_1	P_2	RV peaks
			m s^{-1}		m s^{-1}	(d)	(d)	(d)	(d)
114328	24		2.1				33.5	33.8	
114615	53		6.5	shk	4.9	19.78, 479.59	11.9	21.2	
115577	130		1.9	fwhm	2.0	10000.00, 1.00	38.7	35.6	10000.0, 1.0, 347.4, ...
116906	28		22.6				33.1	32.9	1719.6, 859.8, 573.3, ...
117367	44		1.9				30.4	33.7	26.7, 0.5
118115	46		1.9				36.7	34.4	48.4

4.2 Planet Candidate Signals

4.2.1 HIP25670

HIP25670 has a forest of significant peaks in its periodogram ranging from 17 to 200 days. We find acceptable fits for several of these periods. In the first panel of Figure 4.3, we show the best-fit solution from the local chi-squared minimum at a period of 49.9 days. Alternative periods with similarly good chi-squared values include 34.4 and 72.2 days. The latter two may be aliases of each other caused by the strong window function peak at 65.5 days (Dawson & Fabrycky, 2010). The stellar rotation period is predicted to be near 29-31 days, but no signs of RV-activity correlations are seen. Depending on the period adopted, the best-fit planet $m \sin i$ varies between 10-20 M_E. This system is a good example of the difficulties posed by uneven and sparse time coverage.

4.2.2 HIP41317

Our bulk analysis of HIP41317 reveals a strong periodicity around 89 days with an analytic FAP of 0.2%. The Keplerian best fit corresponds to an 18 M_E planet in an 88.8-day orbit (Figure 4.3). The HIRES RVs for this star, however, do not show any such periodicity. A two-planet model including a $\sim$7 M_E planet on a 10.7-day orbit may fit the combined HARPS + HIRES data better, but the current evidence is not yet sufficient to claim a detection.

4.2.3 HIP76114

HIP76114 appears to host a planet with $m \sin i \approx 0.2$ M_J and an orbital period of 58 days (Figure 4.3). This signal is quite large (K $\sim$ 8.8 m s^{-1}) and no activity correlations are seen for this star, so despite the relative proximity of this period to a multiple of the stellar rotation period (estimated to be 32-33 days) we consider this a likely planet candidate.

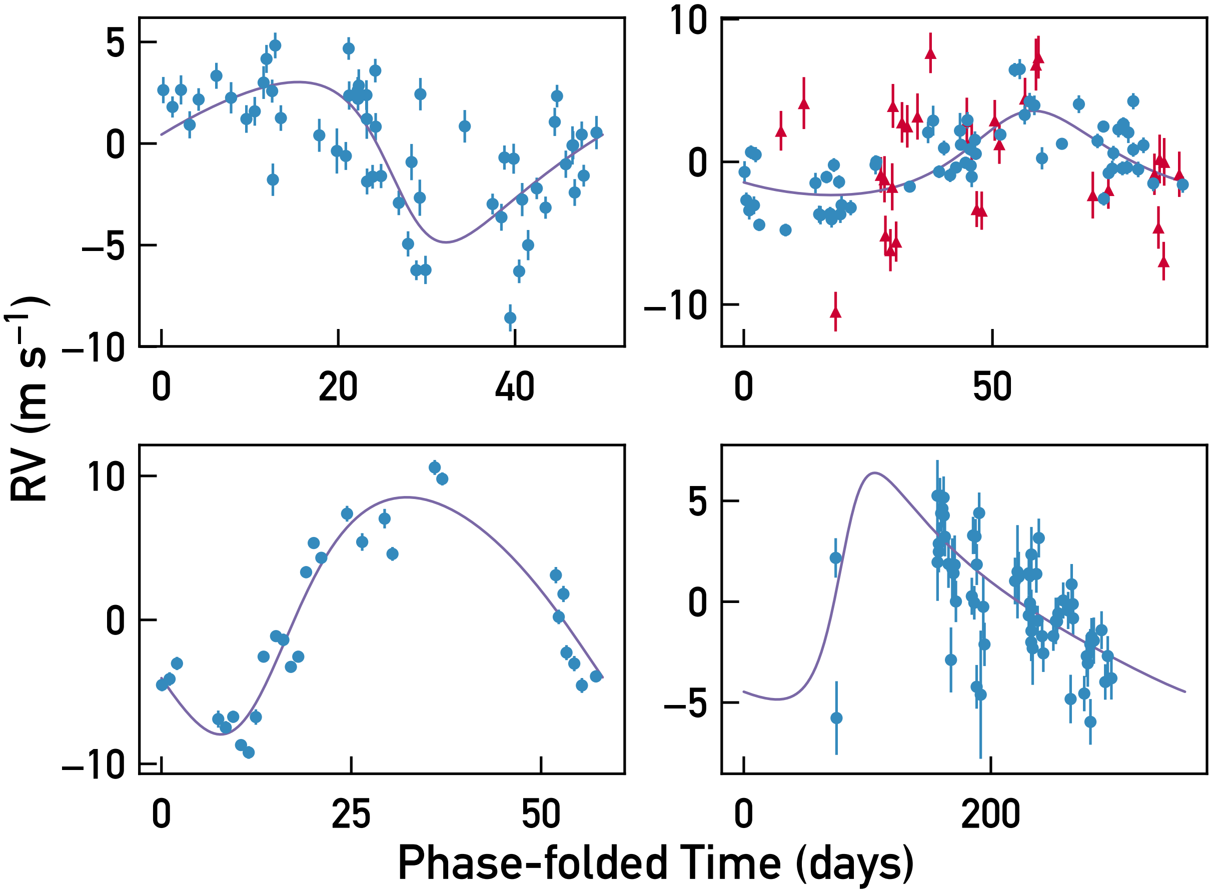

Figure 4.3 A few planet candidates with best-fit RV curves: top left, HIP25670; top right, HIP41317; bottom left, HIP76114; and bottom right, HIP102152. HARPS RVs are plotted as blue circles. For HIP41317, HIRES observations are also available and are plotted as red triangles.

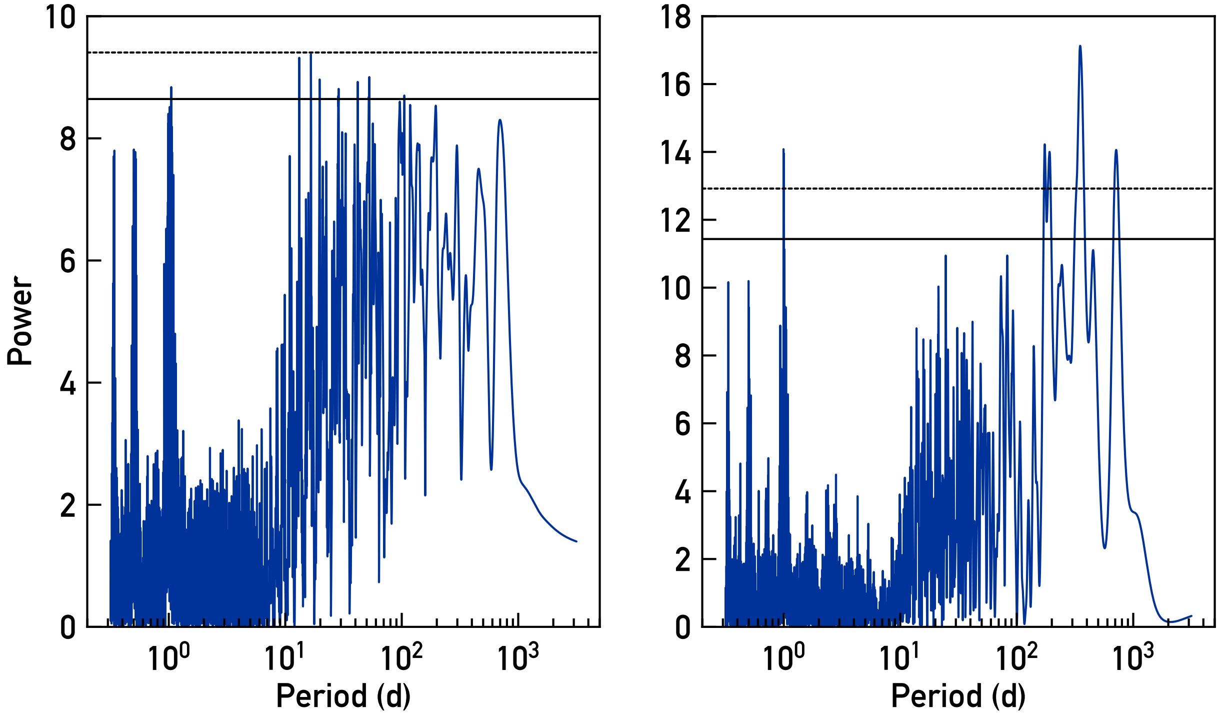

Figure 4.4 RV periodograms for HIP102152 prior to October 2013 (left) and now (right). Horizontal lines indicate the 1% (solid) and 0.1% (dotted) analytic FAP thresholds.

4.2.4 HIP102152

HIP102152 was identified as a promising potential planet host early in our HARPS program due to its high RV RMS and low activity levels. This star is especially intriguing because its abundance pattern as previously determined from UVES spectra exhibits lithium depletion and a T_C trend analogous to the Sun, both of which have been proposed as markers of planet formation (Monroe et al., 2013). We were granted a Director's Discretionary Time (DDT) program on HARPS to monitor the star more closely with 16 nightly observations over a period of six weeks in late 2013.

Prior to the DDT observations, the star's strongest periodogram peaks lay near 13 and 17 days, with a forest of additional peaks at longer periods (see first panel of 4.4). Rather than revealing a complete orbit of a short-period planet, though, the DDT observations captured a steady decline in RV characteristic of a long-period, slightly eccentric giant planet. With the current observational coverage the exact periodicity of the signal remains somewhat degenerate (Figure 4.4). The best fit is achieved at a period near 350 days and a planet $m \sin i$ of 0.2 M_J. As seen in Figure 4.3, this signal is unfortunately difficult to characterize due to its proximity to one year and the resulting poor seasonal coverage.

4.2.5 HIP104045

Much like HIP11915, the "Jupiter twin" host presented in Chapter 2, HIP104045 has a strong RV signal corresponding to an approximately Jupiter-mass planet on an orbital period of ∼10 years (Figure 4.5). At the time of HIP11915b's publication, HIP104045 did not have sufficient cycle coverage to merit inclusion, but with two additional years of observations we can now put strong constraints on this signal as well. No significant correlations are seen between the RVs and any of the activity indicators.

4.3 Activity Cycles

Long-period activity trends analogous to the Sun's 11-year cycle have long been observed in other Sun-like stars. The most comprehensive and long-running observational surveys utilize spectral activity indicators like the S_{HK} index (e.g. Baliunas et al., 1995; Hall et al., 2007). Such cycles are expected to cause periodic changes in the observed radial velocity of the star: during times of low activity, convection in the stellar photosphere creates a net blueshift effect, but at the peak of the cycle a large prevalence of magnetic surface features like spots will inhibit this convection and cause an apparent redshift (Saar & Donahue, 1997). Stellar magnetic cycles have been observed in RVs with semi-amplitudes on the order of 10 m s^{-1} for some Sun-like stars (Lovis et al., 2011).

We identified stars with potential cycles from Table 4.2 by looking for stars with significant correlations between RV and an activity indicator as well as periodogram peaks at large ($>$ 500 day) periods in that indicator. Twenty-one stars meet these criteria. One of these

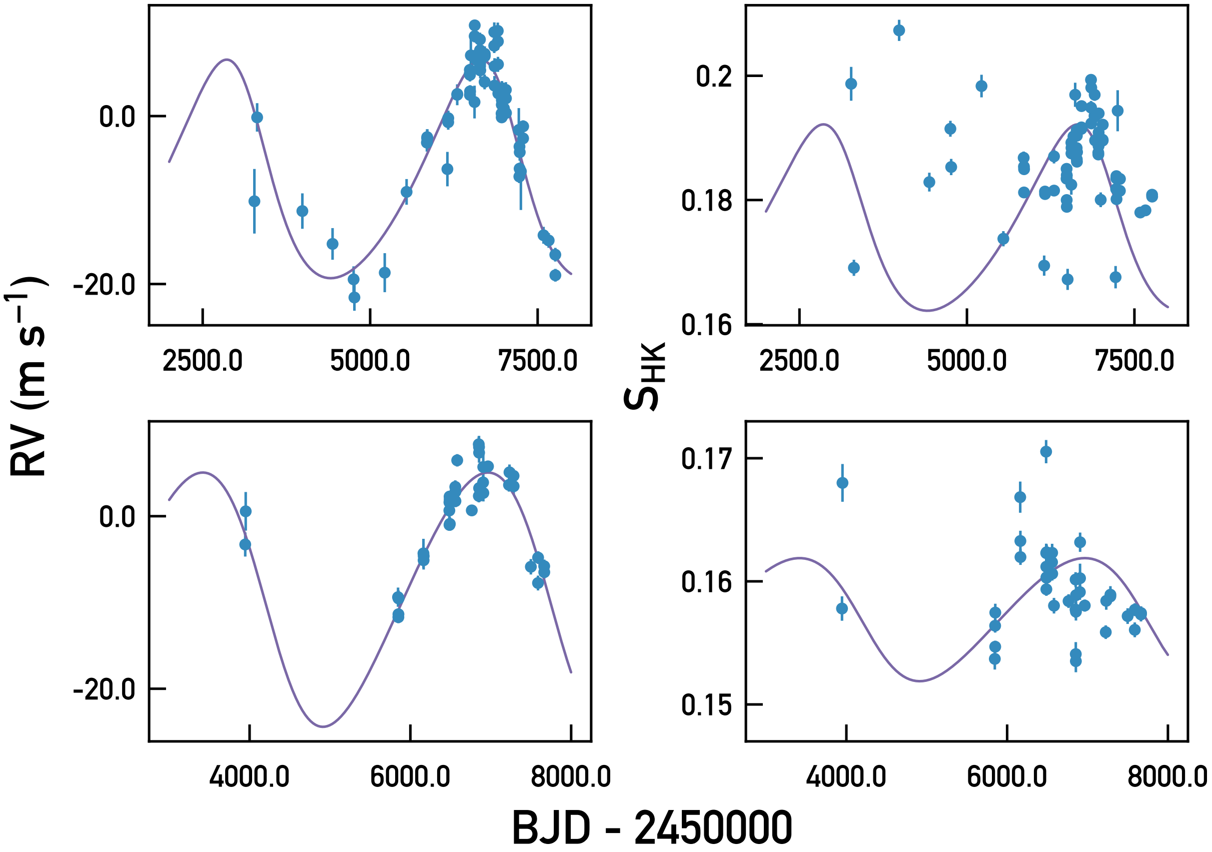

Figure 4.5 RVs for HIP11915 (top left) and HIP104045 (bottom left), along with their S_{HK} time series for comparison (right side panels). Models overplotted with the RVs are the best-fit Keplerians. The amplitudes and offsets of these models were tuned by eye to the S_{HK} time series, keeping all other parameters fixed to the RV solution. The lack of apparent cycling in the S_{HK} time series makes an activity cycle explanation for the RV variations unlikely.

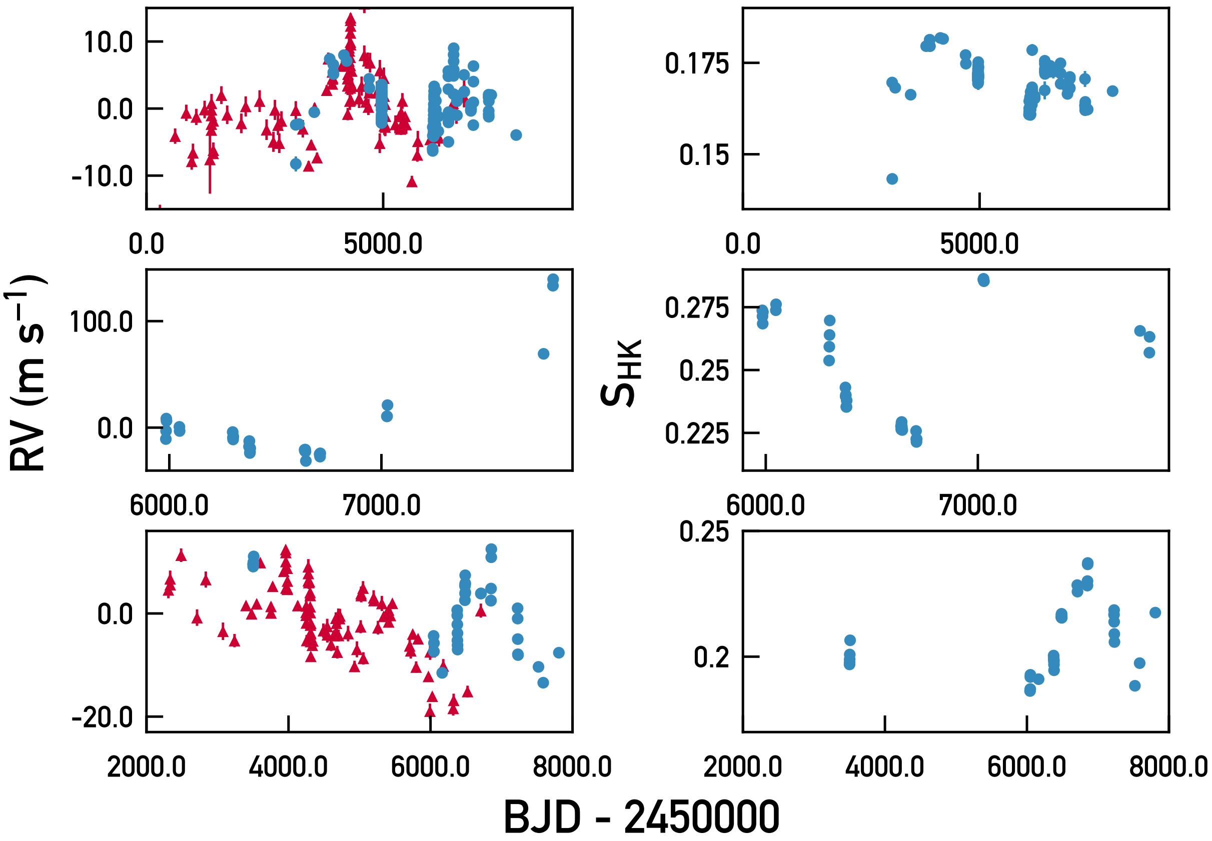

Figure 4.6 Examples of various types of long-period activity seen in the HARPS RVs and S_{HK} time series: a clear cycle in the young solar twin HIP79672, top; a cycle in S_{HK} with questionable RV correspondence in HIP43297, middle; and a likely cycle in the middle-aged solar twin HIP77052, bottom. HARPS data are shown as blue circles. Where available, HIRES RVs are plotted as red triangles.

is HIP11915, whose long-period RV behavior is extensively discussed in Chapter 2; in this case, we find that the observed activity is an insufficient explanation for the long-period RV trend. The other stars show a wide range of cycle-like behaviors. We present a representative sample in Figure 4.6.

The young solar twin HIP79672 is a good example of a strongly cycling star (Figure 4.6, top row). Its seven-year activity cycle has previously been observed in photometry and $\log(R'_{HK})$ measurements by Hall et al. (2007). A characteristic signal with a period of about 7.6 years is clearly seen in the HARPS RVs and activity indices (Meléndez et al., 2014b). The same RV signal is visible in the HIRES data as well.

On the other hand, HIP43297 exhibits a cycle-like trend in S_{HK} without a clear cycle in RV (Figure 4.6, middle row). For the first half of the time series RV and S_{HK} are well-correlated; however, in recent years the stellar RV has increased dramatically while S_{HK} has continued to reach cycle maximum and decrease again. It is not clear whether this RV behavior is due to unusual activity behavior or the influence of a companion on an eccentric orbit.

HIP77052 is a star with a strong RV-S_{HK} correlation and clear long-period behavior in both time series (Figure 4.6, bottom row). Although the variations in RV are of the expected magnitude for a cycle ($K \sim 12$ m s^{-1}), the shape is decidedly non-sinusoidal. The RVs and S_{HK} can be well-fit by a Keplerian with a period of 30 years and eccentricity $e \sim 0.8$. We note that much of this eccentricity is due to the HIRES RVs; with HARPS RVs only a good fit can be found with a 10-year period and zero eccentricity, much more typical of Sun-like stellar activity cycle.

4.4 Short-Period Activity

In addition to long-period cycles, we expect stellar activity to manifest on the timescale of the stellar rotation period and its major harmonics (see e.g. Saar & Donahue, 1997; Boisse et al., 2011). As the star rotates, absorption lines are broadened by the red- and blue-shift of the receding and approaching sides of the visible disk. Localized features like spots and faculae in the stellar photosphere distort this normally symmetric broadening, and as they progress across the stellar surface the changing asymmetry of the spectral lines can easily mimic a Doppler shift at the period of the star's rotation. These effects can be mitigated somewhat through a variety of methods including correlations with spectral line shape-based activity indicators, modeling or "pre-whitening" the data using a known stellar rotation period, or inferring starspot activity from simultaneous photometry if available (Queloz et al., 2001; Aigrain et al., 2012; Dumusque et al., 2017, e.g.).

Since our typical observing pattern is broken up into short runs of a few days separated by months, our HARPS data are unlikely to reveal coherent activity patterns: we lack resolution on long enough timescales to capture a significant part of the rotation period in a single observing run, and the time in between runs is long enough that the stellar surface features have likely evolved and lost phase-coherence with the previous data. As a result, much of the activity in the sample will likely show up as quasi-Gaussian white noise inflating the RMS of the RV data.

In Figure 4.7, we show the distribution of target RV RMS as a function of the stellar age and normalized activity index $\log(R'_{HK})$. As expected, the scatter in RVs is largest for young, high-activity stars. After approximately 4 Gyr, activity levels become nearly constant with age, possibly as a result of a physical transition in the stellar magnetic dynamo (see e.g. Noyes et al., 1984).

4.5 Opportunities for Future Work

From the results presented in Table 4.2, we are able to identify a subset of solar twins best suited for continued follow-up. These targets exhibit no statistically significant correlations between RV and any activity index, meaning that they are inactive ("quiet") at the m s^{-1} level. A total of 35 stars fall into the quiet subsample. We can further divide these targets into a few subcategories:

1. Low-RMS stars, whose RVs show no clear periodicities or trends. Eighteen stars fall into this category: HIP1954, HIP10303, HIP28066, HIP30158, HIP30502, HIP33094, HIP34511, HIP44935, HIP54287, HIP64673, HIP64713, HIP69645, HIP77883, HIP89650, HIP102040, HIP114328, HIP117367, and HIP118115.

2. Stars with an RV trend indicative of a stellar companion, but which have low-RMS inactive RVs after trend removal. Six stars are in this category: HIP14614, HIP30037, HIP54582, HIP62039, HIP64150, and HIP108158.

3. Apparently inactive stars which show signs of hosting planets in the form of strong

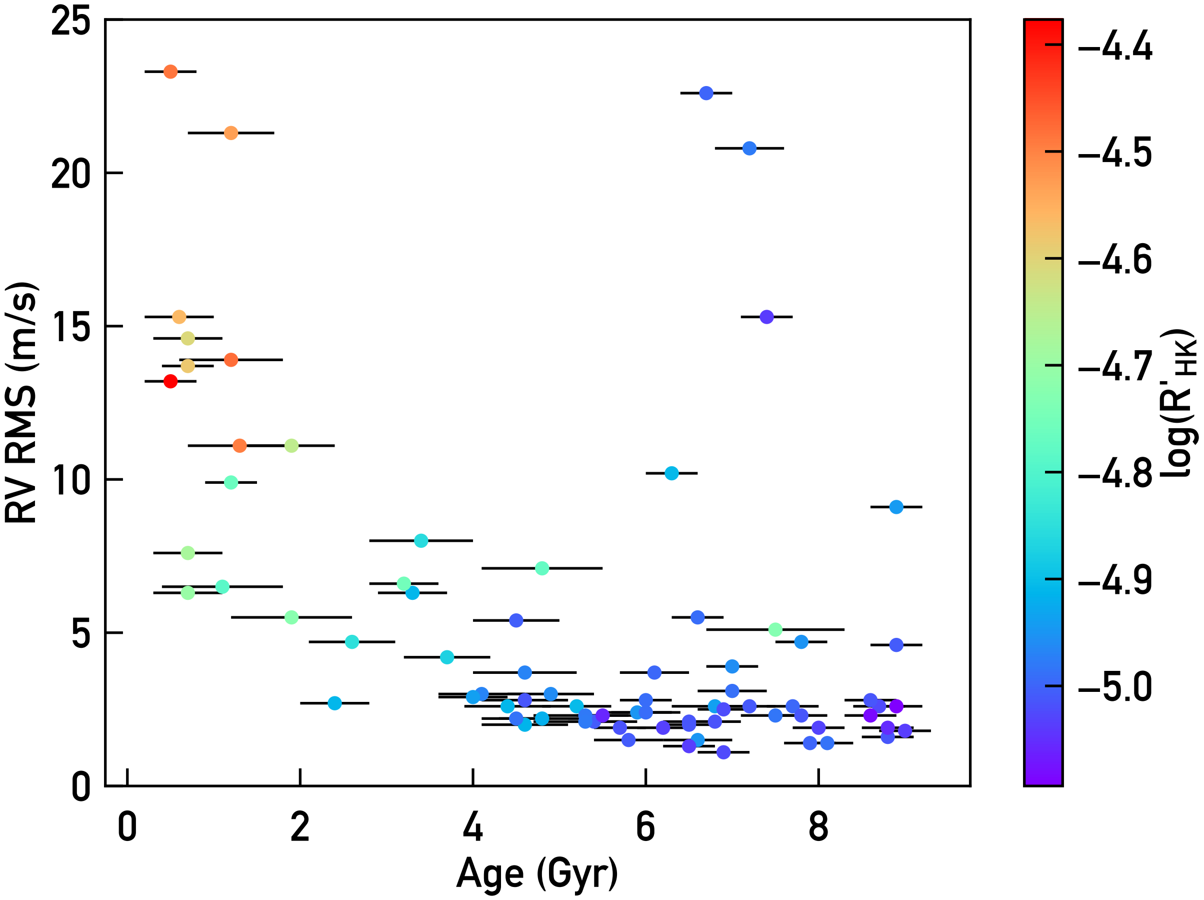

Figure 4.7 RMS of target RVs as a function of stellar age. Color scale indicates the average observed $\log(R'_{HK})$. Ages are derived from isochrones as described in Chapter 6.

RV periodicities and/or high RV RMS. Eight stars are in this category: HIP5301, HIP15527, HIP25670, HIP41317, HIP76114, HIP102152, HIP104045, and HIP116906.

4. Stars which fall into both of the previous categories, having a long-period trend and an excess RV RMS (but no activity correlations) after the trend has been subtracted. Three stars are in this category: HIP43297, HIP72043, and HIP79578.

Five additional stars technically meet the criteria for the quiet subsample but have fewer than ∼10 HARPS RVs recorded. We exclude these stars because their coverage is insufficient to truly rule out high activity levels.

It is interesting to note that the proportion of stars in categories (3) to (1) and categories (4) to (2) are both approximately 2:1, indicating that around one-third of the quiet targets are likely hosts of planets with relatively high RV amplitudes regardless of their binary status. Of course, even the stars in categories (1) and (2) may host planets whose signals are below the current detection threshold, so we make no claims on the overall planet occurrence rate among the sample from this result.

Even the quietest of solar twins will likely show RV noise due to stellar physics at the sub-m s^{-1} level. In particular, inhomogenities in the surface velocity field due to convection and granulation are expected to be a limiting factor around 0.5 m s^{-1} (Meunier & Lagrange, 2013; Dumusque et al., 2015). Finding Earth-like planet signals in the face of this noise will require intensive monitoring on all timescales from hours to years (Dumusque et al., 2011a). Relatively few stars can receive this level of observing time investment. The quiet stars from STPS represent a well-characterized sample of promising candidates for this work.

Part II

Precise Stellar Abundances with Solar Twins

CHAPTER 5

A PROOF-OF-CONCEPT TEST USING SOLAR SPECTRA

In this chapter we present a detailed error budget for high-precision stellar chemical abundance analyses.[1] Using high-resolution, high-signal-to-noise spectra of reflected sunlight from asteroids, we examine several contributors to the total abundance uncertainty. We analyze factors including time-dependent instrumental and atmospheric variability, use of different reference asteroids, use of different instruments, errors in the line equivalent width measurements, and the uncertainty in stellar parameters.

5.1 Observations

The five solar spectra used in this analysis were obtained with very high resolution and signal-to-noise ratios (SNRs) characteristic of data used in past stellar abundance analyses. Two spectra were taken with the Echelle SpectroPolarimetric Device for the Observation of Stars (ESPaDOnS) instrument (Donati, 2003) at the 3.6 meter Canada-France-Hawaii telescope on the night of 2013 March 4. The asteroids Ceres and Vesta were each observed in "star only" mode at a spectral resolving power R = 81000. The spectra have complete coverage over a wavelength range of 380 to 880 nm. Observing conditions for the two spectra were made as identical as possible by observing Vesta immediately after Ceres and at a similar airmass. Observation details are listed in Table 5.1. The spectra were reduced with the Upena pipeline,[2] which employs the Libre-ESpRIT package to reduce and optimally extract each order, perform wavelength calibration, and apply an approximate continuum normalization (Donati et al., 1997). Further normalization was performed using a polynomial fit to the spectrum in 100-Å chunks, with polynomial orders ranging from 2 to 7.

The remaining three solar spectra were taken with the Magellan Inamori Kyocera Echelle

---

[1] This chapter is adapted from Bedell et al. (2014).

[2] `http://www.cfht.hawaii.edu/Instruments/Upena/index.html`

Table 5.1 Summary of observations.

Name	Date	m_V	SNR [a]	AM [b]
Vesta (ESPaDOnS)	2013 Mar 04	8.0	691	1.05
Ceres (ESPaDOnS)	2013 Mar 04	8.3	663	1.01
Vesta (MIKE, 1)	2011 June 24	6.4	730	1.05
Vesta (MIKE, 2)	2011 Sept 09	6.4	764	1.00
Iris (MIKE)	2011 Jan 04	8.2	588	1.33

[a] Signal-to-noise ratio at ∼ 6000 Å.

[b] Airmass at the start of observation.

(MIKE) spectrograph (Bernstein et al., 2003) at the 6.5 meter Magellan Clay telescope. The asteroid Vesta was observed twice and Iris was observed once during three separate observing runs spanning January to September of 2011. All observations were carried out in MIKE's standard setup with the 0.35 arcsecond width slit, giving a spectral resolving power of R = 83000 on the blue CCD and 65000 on the red CCD. Further details of the observations are in Table 5.1. The MIKE spectra were processed with the CarnegiePython MIKE pipeline[3] and barycentric corrections were applied with IRAF's[4] *dopcor* and *rvcor* tasks. Each spectral order was trimmed of ∼ 100 pixels at each end and continuum normalizations were performed using 12th order polynomial fits to the upper envelopes of the data. Furthermore, the 5 reddest orders and the 19 bluest orders were discarded due to unreliable continuum normalization. The orders were merged into a single one-dimensional spectrum using IRAF's *scombine* task. The resulting reduced spectra have complete wavelength coverage between 400 and 800 nm.

---

[3] `http://code.obs.carnegiescience.edu/mike`

[4] IRAF is distributed by the National Optical Astronomy Observatory, which is operated by the Association of Universities for Research in Astronomy (AURA) under cooperative agreement with the National Science Foundation.

Table 5.2 Line List.

Wavelength (Å)	Species	EP (eV)	log(gf)	Vesta ESPaDOnS EW (mÅ)	Ceres ESPaDOnS EW (mÅ)	Vesta 1 MIKE EW (mÅ)	Vesta 2 MIKE EW (mÅ)	Iris MIKE EW (mÅ)
5052.17	6.0	7.68	−1.24	33.6	34.2			
5380.34	6.0	7.68	−1.57	18.3	19.0	21.6	21.1	21.6
6587.61	6.0	8.54	−1.05	13.4	13.4	14.7	13.9	14.2
7111.47	6.0	8.64	−1.07	9.4	9.5			
7113.18	6.0	8.65	−0.76	19.7	19.1	23.1	22.7	22.9
					⋮			

Note. — Table 5.2 is published in its entirety in the electronic version of Bedell et al. (2014). A portion is shown here for guidance regarding its form and content.

5.2 Abundance Analysis

5.2.1 Line Measurements

For the analysis of chemical abundances, we employed a line list consisting of 97 Fe I lines, 18 Fe II lines, and 167 lines of other elements (C, O, Na, Mg, Al, Si, S, K, Ca, Sc, Ti, V, Cr, Mn, Co, Ni, Cu, and Zn). The line list was based on the list employed in Meléndez et al. (2014b), with minor modifications for differing wavelength coverage and telluric line presence in the ESPaDOnS and MIKE spectra. Lines were selected for these analyses with a preference for unsaturated lines with minimal blending. The full line list is presented in Table 5.2. Atomic parameters were taken from laboratory transition probabilities when available and supplemented with theoretical or solar gf-values. For the differential analysis technique employed the exact gf-values adopted are irrelevant, since they cancel out during calculation of the differential abundances.

We measured all line equivalent widths (EWs) by hand using the *splot* task in IRAF to fit a Gaussian to each line. If necessary, multiple Gaussians were fit in the case of a blend. Since the wavelength coverage of the MIKE and ESPaDOnS instruments are different, spectra from each instrument were analyzed separately with slightly modified line lists. Careful attention was given to ensure that the same continuum region and wavelength interval were used to fit lines across all spectra from the same instrument.

A strictly accurate absolute measurement of equivalent width would depend on finding the true spectral continuum. We chose instead to use a "pseudo-continuum" approach which employs whichever point(s) in the immediate vicinity of the line appear most constant across the multiple spectra being measured. The aim of this approach is to measure EWs with the highest possible precision or consistency across multiple spectra, minimizing the impact of nearby features on the line in question. Since our line list consists of lines in the linear region of the curve of growth, a small discrepancy between the measured EWs and the true EW has an insignificant impact on the resulting differential abundance as long as this discrepancy is equally present in the target and reference spectrum measurements. The pseudo-continuum approach is especially valuable in the case of a crowded spectral region in which the spectrum has a local slope across the measured line due to the wings of neighboring lines or unresolved broad features (see the examples of Ti I and Na I in Figure 5.1). The use of very local pseudo-continuum points is not always the best option, however. In some cases, such a choice would result in a pseudo-continuum level too low to accurately fit a Gaussian profile to the line (as in the example of Fe I in Figure 5.1). In other cases, any local slope is minimal enough compared to the level of noise in the spectrum that choosing two local points rather than a broader swath of nearby continuum would only add noise to the measurement (as in the example of Sc I in Figure 5.1). The optimal continuum or pseudo-continuum choice is largely a judgment call made on a line-by-line basis.

We carried out tests to evaluate the validity of this measurement technique compared to more classical methods, measuring a set of 40 Fe I lines in the MIKE Vesta 1 and Vesta 2 spectra using several strategies and comparing the scatter in the resulting differential abundances. The measurement technique used in this work, with a combination of pseudo-continua and "true" continua chosen on a line-by-line basis, yields a resulting scatter in abundances measured by the standard error on the mean of 0.0023 dex. This value was

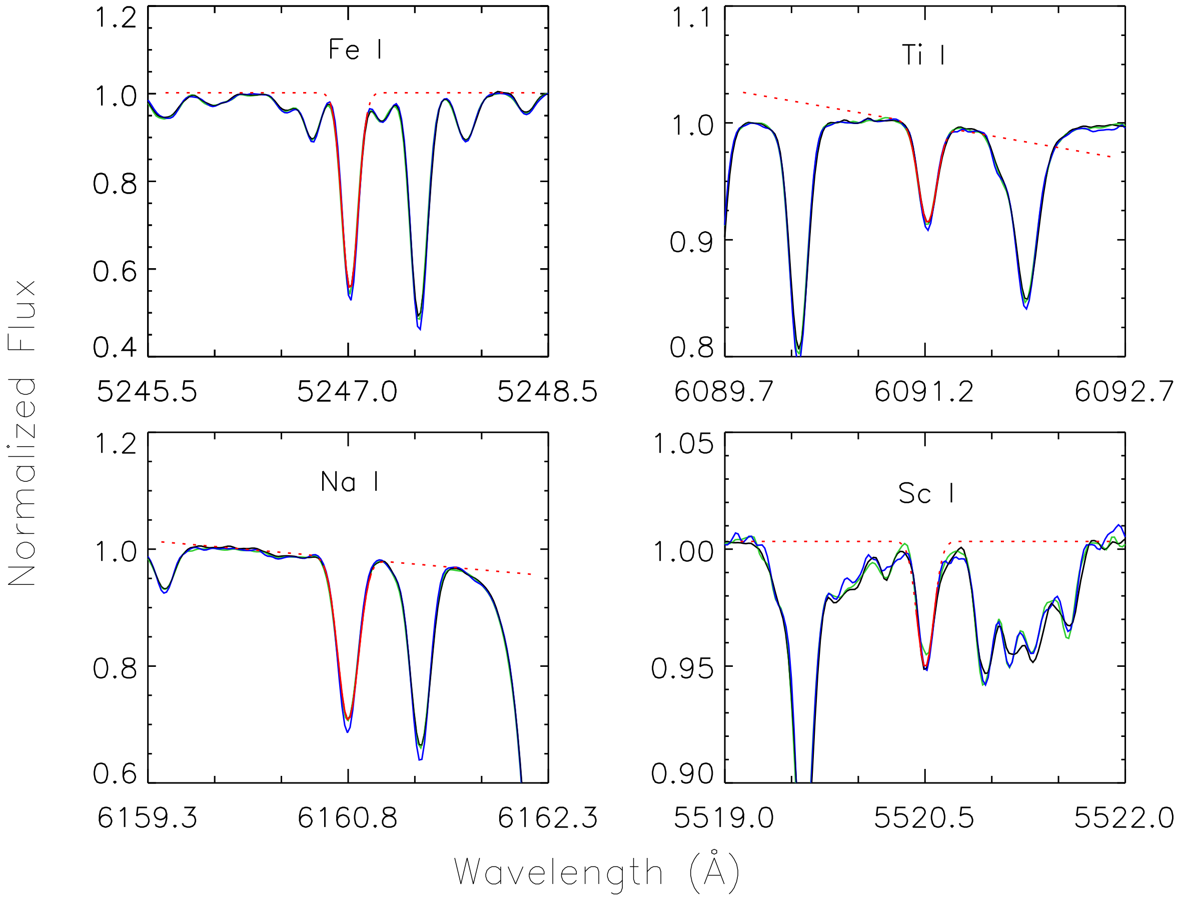

Figure 5.1 Example spectral lines with MIKE Vesta 1 data plotted in black and Gaussian fits to the data plotted in red, with the estimated local continuum extrapolated as a dotted line. MIKE Vesta 2 and Iris spectra are plotted in green and blue respectively for comparison. In some cases, the local pseudo-continuum selected for equivalent width measurements is noticeably different from the true stellar continuum. Choice of pseudo-continuum is made to minimize the potential effects of nearby unresolved features or line wings which may be slightly blended with the line being measured, introducing a local slope or offset.

revised down to 0.0016 dex when the five largest outliers were remeasured with slightly different continuum choice. In contrast, adopting a strict "true" continuum for all lines yields a scatter of 0.0024 dex, and adopting the two neighboring points to the line as a peudo-continuum in every case yields a scatter of 0.0064 dex. For further comparison we used the automated equivalent width measuring code ARES (Sousa et al., 2007), which gave a scatter of 0.0035 dex.

The subjectivity of an individual's choice of pseudo-continuum level could potentially bias results, especially in the case of elements for which only a few lines were measured. To mitigate this effect, seven elements (C, O, Mg, Al, S, Sc, and Cu) were independently analyzed by two of us in a blind test. The resulting abundances for the re-measured elements were generally within the one-sigma statistical error bars of the original abundances.

5.2.2 Stellar Parameter Determination

A critical first step in abundance determination is the derivation of correct stellar parameters (effective temperature $T_{\rm eff}$, surface gravity $log(g)$, microturbulent velocity v_t, and metallicity [M/H]) for the target star. Although all spectra used in this work are solar, we treat the target spectra as unknown stars and determine their parameters using spectral iron lines as we would for any other star. Measured Fe I and Fe II line EWs were converted to abundances using the 2002 version of MOOG [5] with the *abfind* driver, which employs a curve-of-growth method. We used Kurucz ODFNEW model atmospheres[6] and linearly interpolated between grid points to achieve the required resolution in parameter space. Stellar parameters for each target spectrum were found through a differential approach with respect to a reference spectrum, arbitrarily taken as the Vesta 1 spectrum for the MIKE data and Vesta for the ESPaDOnS data. We fix the parameters of the reference spectrum to the nominal solar values, $T_{\rm eff} = 5777$ K, $log(g) = 4.44$ dex, and [M/H] = 0.0, and find the optimal microturbu-

---

[5] `http://www.as.utexas.edu/ chris/moog.html`

[6] `http://kurucz.harvard.edu/grids.html`

lence value by minimizing the trend between derived Fe I abundance and reduced equivalent width. Throughout all analyses, [M/H] was assumed to be equal to [Fe/H].

We then determine the stellar parameters for other spectra by computing iron abundances for the target star and the reference and imposing requirements on the *differential* abundances (target - reference), as described in Meléndez et al. (2014a). These requirements consist of minimal slopes in Fe I abundance with excitation potential (primarily sensitive to the assumed model T_{eff}) and with reduced equivalent width (primarily sensitive to the assumed microturbulence value), minimal difference between the derived abundances of Fe I and Fe II (primarily sensitive to the assumed surface gravity), and equivalence between the input metallicity on the stellar atmosphere model and the output Fe abundance. Our key assumption in using the differential abundances is that any systematic model errors manifesting in the reference star's abundances (e.g. a slope in Fe I abundance with excitation potential when using a model with the nominal solar effective temperature) are identical for the target star. These systematic errors should therefore be subtracted out of the abundances before equilibrium conditions are considered. Since all spectra considered in this paper are solar, this assumption is trivially valid. In a more general sense the assumption should hold for target stars which are sufficiently close to the chosen reference star in parameter space; see for example the evaluation of potential systematics in stellar parameters for a solar twin sample in Ramírez et al. (2014b).

Uncertainties on our derived stellar parameters were estimated using the method described in Epstein et al. (2010) and Bensby et al. (2014). In brief, the observational errors on the quantities which were minimized to find the optimal parameter solution are propagated while accounting for the dependence of each stellar parameter on the others. For the metallicity parameter, the uncertainty was taken as this formal parameter uncertainty added in quadrature with the line-to-line scatter on [Fe/H] derived in the spectral analysis. The parameter solutions and uncertainties for each spectrum analyzed are shown in Table 5.3.

5.2.3 Abundance Measurements

After the optimal model atmosphere was chosen, we determined abundances for all elements in the line list using MOOG. For elements which were observed in multiple ionization states (Fe, Sc, Ti, and Cr), the final abundance was taken as the error-weighted average of the abundances from each ionization state. Hyperfine structure corrections were applied for four elements (Cu, Co, Mn, and V) using MOOG's *blends* driver. All abundances used in this paper assume local thermal equilibrium (LTE). Non-LTE corrections can be crucial for accurate absolute abundance values, but our approach aims only for high precision on the differential measurements, so that applying a similar non-LTE correction to both reference and target stellar abundances creates a very small change in the derived values. Past solar twins work in Meléndez et al. (2012) has shown that non-LTE corrections have a negligible effect (on order of 0.001 dex) on differential abundances for stars with extremely similar parameters to the reference solar spectrum.

5.3 Estimated Error Budget

We consider several combinations of spectra which introduce various potential sources of error on the derived abundances, including time-dependent effects, use of different asteroids, and use of different instruments. The scatter in abundance derived from lines of the same element gives an estimate of the level of random error associated with these uncertainty sources. We also use the deviation of the derived abundances from the expected solar values ($[X/H] \equiv 0.0$ dex) as an estimate of more systematic uncertainty which may be underestimated in the scatter-based error bars. These statistics are compared to the expected errors from formal uncertainties on the line equivalent width measurements and on the derived stellar parameters.

5.3.1 Observed Errors

Time-Dependent Systematics

Instrumental systematics like mechanical flexure and internal scattering of light may change considerably over time, so it is reasonable to expect that spectra taken with the same instrument at significantly different times would have some additional error due to varying spectral quality. Additionally, the Earth's atmosphere is a major contributor to time-dependent spectral variations as weather evolves and as the target spectrum shifts with respect to telluric features due to the Doppler effect of the Earth's rotation. Although we discard obviously telluric-contaminated lines from the list, small unresolved tellurics are still a concern.

We quantify the error due to time-dependent systematics using two spectra of Vesta taken with the MIKE instrument on dates June 24, 2011 ("MIKE Vesta 1") and September 09, 2011 ("MIKE Vesta 2"). The derived stellar parameters for the Vesta 2 spectrum relative to the Vesta 1 spectrum are extremely close to the expected solar values, with T_{eff} differing by 2 ± 5 K, $log(g)$ by 0.00 ± 0.01 dex, v_t by 0.01 ± 0.01 km s^{-1}, and metallicity by -0.01 ± 0.01 dex (Table 5.3). The derived [X/H] abundances are shifted down to a mean of -0.006 dex as a result of this metallicity value, but the standard deviation among [X/H] abundances is only 0.007 dex, indicating that the abundance of one measured element relative to another (e.g. [X/Fe]) can be considered reliable to below 0.01 dex precision (Figure 5.2, Table 5.4).

The most significant outlier from the mean is K ([K/H] - $\langle$[X/H]$\rangle$ = 0.020 dex, or 3.3σ when using the line-to-line scatter as an error bar). This is a less significant deviation when the error due to parameter uncertainties is taken into account (bringing the deviation down to 2.2σ; see section 5.3.2), but it is still an indication of the limitations of employing a short line list. In our list, K is the only element for which only a single line was measured. An estimate of "line-to-line scatter" was obtained from remeasuring the line multiple times with slightly different but still acceptable continuum choices and taking the standard deviation of the resulting abundances, but this error estimate neglects any potential effects on the line such as an unresolved blend that will remain regardless of the local continuum choice.

In general, the consistency of abundances for all elements and their agreement with the expected solar values ([X/Fe] $\equiv$ 0.0) demonstrate that time-dependent systematics for the MIKE instrument over a timescale of months cause abundance errors well below the 0.01 dex level.

Choice of Asteroid

Differential abundance analyses frequently employ reference spectra of solar light reflected from the brightest asteroid at the time of observation, which can vary between different observing runs. Thus a potential error in comparing stellar abundances derived from stars observed at different times could be varying properties of the reference solar spectrum depending on which asteroid was used for each star's reference. It is generally expected that asteroid reflectance properties should have a negligible effect on the observed solar spectrum, since reflectance does not change significantly within wavelength ranges below a few hundred Å (Xu et al., 1995; Binzel et al., 1996; DeMeo et al., 2009). Nevertheless, the possibility of spectral variations from chemical activity such as water evaporation on Ceres (Küppers et al., 2014) makes the use of different asteroids a source of error worth investigating.

We investigate the possibility of asteroid-dependent errors using the ESPaDOnS spectra of Ceres and Vesta, which were observed very close in time and should have minimal time-dependent errors. The asteroids Ceres and Vesta have significantly different reflectance properties (DeMeo et al., 2009), making them good test subjects. The derived stellar parameters for Ceres with respect to Vesta are extremely accurate and of comparable precision to the MIKE pairs (Table 5.3). The resulting [X/H] values have a standard deviation of 0.006 dex and a mean value of 0.001 dex with no major outliers (Figure 5.3, Table 5.5).

An independent test of asteroid-induced errors was performed using the MIKE spectra of Iris and Vesta 1. These spectra were obtained nearly six months apart in time. The [X/H] values for Iris with respect to Vesta have a mean and standard deviation consistent with those of MIKE Vesta test on time-dependent systematics (Figure 5.4, Table 5.6). Again, the largest outliers from the mean (Al at 4.25σ and S at 1.7σ) are elements for which our line list is somewhat limited: Al has four lines grouped as two doublets, while S has four lines, two of which are a doublet and the other two of which are separated by less than 15 Å. The strong dependence of our method on a good choice of local pseudo-continuum for the differential line measurements can lead to errors in the abundances from imperfect spectral normalization or unresolved features in the continuum. These errors will not be fully reflected in the line-to-line scatter if multiple lines come from the same local region and carry the same bias. This underestimation of the error can be reduced, if not eliminated, by choosing different local pseudo-continua for different lines within the same region; this approach was used for the O triplet and the single K line with good results in these analyses.

Neither of the above tests show any bias on abundances arising from use of different asteroids. These results are consistent with a past indirect test on the asteroids Ceres and Juno performed by Meléndez et al. (2012, Appendix B), which found an element-to-element scatter on abundances of 0.005 dex.

Choice of Instrument

The instrument used for the observation and its line spread function are expected to play a significant role in the spectral analysis when pushing the boundaries of the highest abundance precision. Although line equivalent widths are in principle independent of resolution, our use of the local pseudo-continuum in EW measurements means that the resolving power applied to the small features surrounding the line in question can make a difference to the line measurement. Additionally, fitting each line with a Gaussian will naturally lead to errors on the fit due to the inherent non-Gaussianity of the line and of the spectrograph's instrumental profile. When measuring lines differentially using the same instrument, the resolution and instrumental profile of each spectrum are roughly the same and these effects cancel out. If the spectra of the target and reference objects are taken with different instruments, though, the effect of different resolution in the continua could become more important. Moreover, comparing equivalent widths measured as Gaussians from spectra with substantially different non-Gaussian instrumental profiles could introduce significant errors even for instruments with similar nominal resolutions.

To test this effect, we used the ESPaDOnS Vesta spectrum as a reference and the MIKE Vesta 1 spectrum as the target. We trimmed the line list to exclude any lines not present in both spectra. Line EW measurements had been performed separately for these two spectra, meaning that the location of the chosen pseudo-continuum likely varied in some cases. To mitigate this effect, we ran an initial abundance analysis, remeasured the lines which gave the most severe outliers in abundance for each element using a consistent choice of continuum, and re-ran the analysis. The results have by far the largest errors of any analysis considered in this paper, with a standard deviation of 0.04 dex (Figure 5.5, Table 5.7). Due to the relatively large scatter in Fe line abundances, the stellar parameters are also quite uncertain, with the estimated errors being 5-6 times larger than in previous tests (Table 5.3). The relatively poor resulting stellar parameters, in particular the retrieved $log(g)$ of 0.09 ± 0.06 dex below the nominal solar value and the retrieved metallicity of 0.04 ± 0.02 dex above the solar value, make model-based systematic errors in the elemental abundances likely. Abundance precision of 0.01 dex was achievable only in one element, Si. While a better optimized line list and a differential approach to measuring every line would likely improve the precision to some extent, these results suggest that comparing spectra which were obtained with different instruments is inadvisable for the desired high-precision results.

5.3.2 Expected Errors

In this section, we consider the expected level of error based on formal uncertainties in the data and compare this to the observed error levels.

Equivalent Width Measurement Uncertainties

The equivalent widths of the spectral lines are the directly measured quantities in the abundance analysis, so it is key to understand the level of uncertainty in the measured EWs and its effect on the final results. The expected root-mean-square error in EW based on photon statistics is given in Cayrel (1988) as:

$$< \sigma_{EW}^2 >^{\frac{1}{2}} \simeq 1.6(w\delta x)^{\frac{1}{2}}\epsilon \tag{5.1}$$

where w is the Gaussian full width at half maximum of the line, δx is the pixel size in wavelength units, and ϵ is the relative photometric accuracy of the continuum, taken here to be the inverse of the local SNR.

For the spectra used in this analysis, typical EW errors from Equation 5.1 are on order of 0.1 mÅ. We can estimate the effect of these EW errors on the final abundances by drawing a simulated EW from a Gaussian distribution centered on the measured value and with a σ of 0.1 mÅ for each line used in the analysis. Adding random errors in this manner on every line EW for the pair of MIKE Vesta spectra yielded a typical change in each elemental abundance of 0.001 dex. The statistical error bars on the log abundances increased by only 7 ± 10 %.

We conclude from this test that the error on the EW measurements expected from photon statistics generally makes up a small portion of the total statistical errors on the final abundances at high SNR. Factors such as blending of unresolved lines and continuum deformation from unresolved lines or telluric features are more likely to dominate the errors on measured EWs, causing the level of line-to-line scatter which we observe. For this reason, high resolution and high SNR are critical factors in obtaining high precision abundances, since they enable the identification of the optimal continuum choice and accurate measurements of line EWs.

Table 5.3 Summary of derived sun-as-a-star parameters.

Spectrum	$T_{\rm eff}$ (K)	σ_T (K)	log g (dex)	σ_{logg} (dex)	v_t (km s^{-1})	σ_{v_t} (km s^{-1})	[M/H] (dex)	$\sigma_{[M/H]}$ (dex)
Iris (MIKE) [a]	5769	5	4.42	0.01	0.86	0.01	-0.01	0.01
Vesta (MIKE, 2) [a]	5779	5	4.44	0.01	0.86	0.01	-0.01	0.01
Ceres (ESPaDOnS) [b]	5778	8	4.44	0.02	0.85	0.01	0.00	0.01
Vesta (MIKE, 1) [b]	5780	29	4.35	0.06	0.87	0.05	0.04	0.02

[a] Measured differentially with respect to standard MIKE Vesta 1, with assumed solar parameters ($T_{\rm eff}$ = 5777 K, log g = 4.44, v_t = 0.85 km s^{-1}, [M/H] = 0.00).

[b] Measured differentially with respect to standard ESPaDOnS Vesta, with assumed solar parameters as above.

Stellar Parameter Uncertainties

The uncertainty in physical parameters of the target star can lead to use of a sub-optimal model atmosphere in the abundance analysis, creating additional errors. Uncertainties on each parameter were propagated to individual abundances by running the MOOG *abfind* analysis with model atmospheres which varied each parameter by its one-sigma error bar, and the resulting abundance changes due to each parameter were added in quadrature to yield a net "parameter-based uncertainty" on every abundance.

In general, the parameter-based uncertainties are at or below the level of statistical uncertainty inferred from the line-to-line scatter (Tables 5.4 - 5.6). This implies that with high spectral quality and a sufficiently long and balanced Fe line list, which enable stellar parameter precisions on the level of those achieved in our tests, the derived stellar parameters are not the limiting factor on abundance precision. A notable exception is the case of Vesta MIKE - ESPaDOnS (Table 5.7), where the much larger uncertainties on the parameters cause the parameter-based uncertainties to dominate the errors on abundances. As discussed in section 5.3.1, the additional errors introduced by the use of different instruments led to a larger scatter in the derived Fe abundances, making it difficult to achieve parameters as precise as those found in the other tests.

5.4 Implications for Planet Signatures

One past result that critically depends on high-precision abundances is the Sun's evident chemical depletion trend with condensation temperature relative to the average solar twin star (Meléndez et al., 2009), often interpreted as a potential sign of past terrestrial planet formation. We searched for trends in elemental abundance with the 50% condensation temperature from Lodders (2003) in each target spectrum considered above. All solar spectra were found to have a slope in abundance vs. condensation temperature consistent with zero within 2σ (Figure 5.6). It is important to note, however, that characterizing the stellar parameter uncertainties correctly is a key part of evaluating the significance of a potential slope with condensation temperature. The elements at low condensation temperature, especially C and O, are derived from high excitation potential lines. An incorrect stellar effective temperature can change the abundances of C and O relative to the refractory elements and induce a false slope. One way to mitigate this problem is to derive the carbon abundance separately from CH molecular lines. This method was not used in this paper due to the CH lines under consideration falling outside of the MIKE spectral range.

We vary the model parameters from each best fit solution in order to estimate the error in temperature needed to reproduce an abundance slope of the size typically investigated as potential planet formation signatures, as in e.g. Schuler et al. (2011a) or Ramírez et al. (2013). To produce a spurious slope of 5×10^{-5} dex K^{-1}, the effective temperature chosen would need to be around 60-70 K below the true value. For this slope to be a statistically significant result, of course, the formal uncertainties on the stellar parameters would need to be far below the level of the true error. For this reason, it is critical to evaluate the stellar effective temperature and its error completely, preferably using multiple methods of temperature determination. In most of the analyses carried out in this paper, the solar temperature is retrieved for the target with an error well below the estimated 1σ error bar.

5.5 Conclusion

Based on the tests conducted on solar spectra taken with different asteroids as reflectors, different instruments, and different epochs of observation, we conclude that precision below the level of 0.01 dex is achievable given high-quality target and reference spectra obtained with the same instrument. Time-dependent effects on the scale of several months appear relatively unimportant, as does the choice of asteroid used for a reflected solar spectrum. Due to the need for a constant pseudo-continuum level for measuring differential equivalent widths, the line spread function of the target spectrum relative to the reference spectrum is a critical factor in measurement precision. This effect means that using target and reference spectra taken with different instruments is inadvisable.

The greatest contributor to the achievable precision of an individual element is the line list employed in the analysis. For the most part this effect can be quantified by using the standard error on the mean abundance as a statistical error bar, but we urge caution when applying this method of error estimation to elements which have multiple lines within the same small wavelength region. As seen by the examples of K and Al in these analyses, the statistical error can underestimate potential effects from local continuum normalization or unresolved blends on the consistency of the pseudo-continuum across spectra.

Past work using this technique of high-precision differential abundance analysis has demonstrated that the results are free of potential systematic biases at or above the level of 0.01 dex originating from the model atmosphere used (Ramírez et al., 2011; Meléndez et al., 2012) or from non-LTE effects (Meléndez et al., 2012). We can now conclude that time-dependent instrumental effects and the choice of asteroid for the solar standard are also free of such errors. Given a thorough understanding of the limitations of one's line list and use of the same instrument for the target and reference spectra, we find no reason to doubt the reality of sub-0.01 dex precisions on differential abundances for spectrally similar stars.

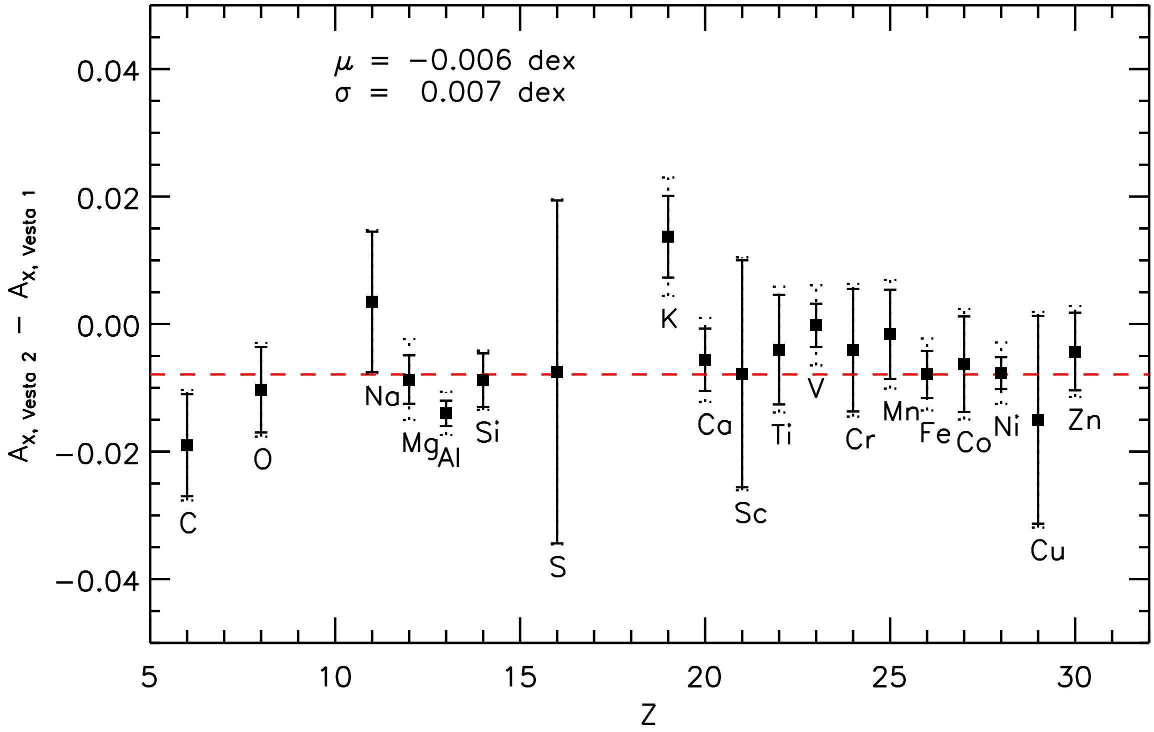

Figure 5.2 Differential abundances for Vesta spectra taken at two epochs with the MIKE instrument. Solid error bars represent the standard error on the mean differential abundance derived from the sample of lines measured. Dotted error bars represent the "total" error from adding statistical error and error from uncertainty on the stellar parameters in quadrature. Red dashed line is at the level of the derived [Fe/H] abundance.

Table 5.4 Stellar abundances [X/H] for MIKE Vesta 2 - Vesta 1.

Element	$[X/H]_{Vesta}$ (dex)	$\Delta T_{\rm eff}$ +5K (dex)	$\Delta \log g$ +0.01 dex (dex)	Δv_t +0.01 km s^{-1} (dex)	Δ[M/H] +0.01 dex (dex)	param[a] (dex)	obs[b] (dex)	total (dex)
C	-0.019	-0.003	0.002	0.000	-0.001	0.003	0.008	0.009
O	-0.010	-0.003	0.000	0.000	0.000	0.003	0.007	0.007
Na	0.004	0.002	0.000	-0.000	0.001	0.002	0.011	0.011
Mg	-0.009	0.004	-0.001	-0.002	0.001	0.005	0.004	0.006
Al	-0.014	0.003	-0.001	0.000	0.001	0.003	0.002	0.003
Si	-0.009	0.001	0.001	-0.000	0.001	0.002	0.004	0.005
S	-0.007	-0.002	0.002	0.000	0.000	0.003	0.027	0.027
K	0.014	0.005	-0.003	-0.001	0.003	0.007	0.006	0.009
Ca	-0.006	0.003	-0.002	-0.002	0.002	0.004	0.005	0.007
Sc[c]	-0.008	0.002	0.002	-0.001	0.002	0.004	0.018	0.018
Ti[c]	-0.004	0.004	0.001	-0.001	0.002	0.005	0.009	0.010
V	-0.000	0.005	0.001	-0.000	0.001	0.005	0.003	0.006
Cr[c]	-0.004	0.003	0.000	-0.002	0.002	0.004	0.010	0.010
Mn	-0.002	0.004	-0.001	-0.002	0.001	0.005	0.007	0.009
Co	-0.006	0.004	0.001	-0.000	0.002	0.004	0.007	0.009
Ni	-0.008	0.003	0.000	-0.001	0.002	0.004	0.003	0.005
Cu	-0.015	0.003	0.001	-0.001	0.002	0.005	0.016	0.017
Zn	-0.004	0.001	0.001	-0.002	0.003	0.004	0.006	0.007
Fe[c]	-0.008	0.003	-0.000	-0.002	0.002	0.004	0.004	0.006

[a] Error due to propagating formal uncertainties on the stellar parameters.

[b] Statistical error reflected in the line-to-line scatter of derived abundances.

[c] Abundances and errors quoted are the weighted mean of the results for two ionization states.

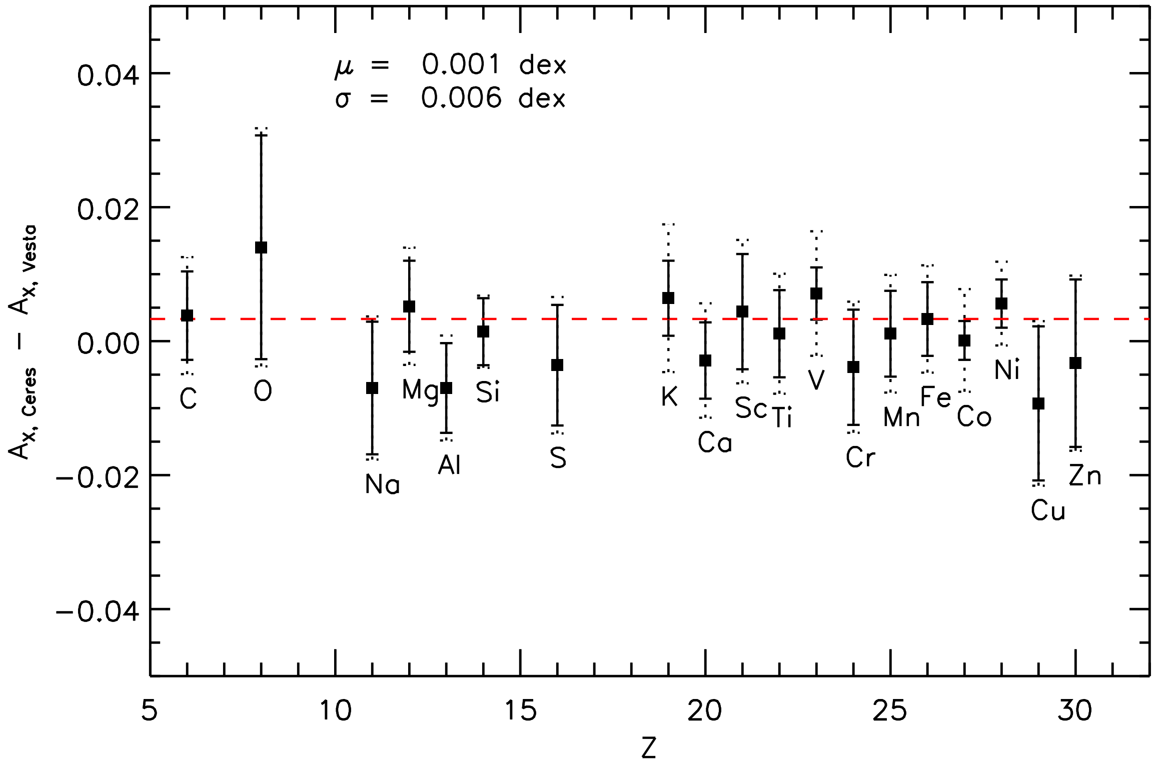

Figure 5.3 Differential abundances for Ceres and Vesta data from the ESPaDOnS instrument. Error bars and red line as in Figure 5.2.

Table 5.5 Stellar abundances [X/H] for ESPaDOnS Ceres - Vesta.

Element	$[X/H]_{Ceres}$ (dex)	$\Delta T_{\rm eff}$ +8K (dex)	$\Delta\log g$ +0.02 dex (dex)	Δv_t +0.01 km s^{-1} (dex)	Δ[M/H] +0.01 dex (dex)	param[a] (dex)	obs[b] (dex)	total (dex)
C	0.004	-0.004	0.004	0.000	0.001	0.006	0.007	0.009
O	0.014	-0.006	0.000	-0.001	0.002	0.006	0.017	0.018
Na	-0.007	0.004	0.000	-0.000	-0.000	0.004	0.010	0.011
Mg	0.005	0.005	-0.001	-0.001	-0.001	0.006	0.007	0.009
Al	-0.007	0.003	-0.002	-0.000	-0.000	0.004	0.007	0.008
Si	0.001	0.002	0.001	-0.000	0.001	0.002	0.005	0.005
S	-0.004	-0.004	0.003	-0.000	0.001	0.005	0.009	0.010
K	0.006	0.006	-0.006	-0.002	0.002	0.009	0.006	0.011
Ca	-0.003	0.006	-0.003	-0.002	0.000	0.006	0.006	0.009
Sc[c]	0.004	0.002	0.006	-0.002	0.002	0.006	0.009	0.011
Ti[c]	0.001	0.004	0.004	-0.002	0.001	0.006	0.006	0.009
V	0.007	0.008	0.002	-0.000	-0.001	0.008	0.004	0.009
Cr[c]	-0.004	0.003	0.003	-0.002	0.001	0.005	0.009	0.010
Mn	0.001	0.006	-0.000	-0.001	-0.000	0.006	0.006	0.009
Co	0.000	0.006	0.003	-0.000	0.000	0.007	0.003	0.008
Ni	0.006	0.005	0.000	-0.002	0.001	0.005	0.004	0.006
Cu	-0.009	0.003	0.001	-0.001	0.002	0.004	0.011	0.012
Zn	-0.003	0.002	0.001	-0.002	0.002	0.004	0.013	0.013
Fe[c]	0.003	0.006	0.000	-0.002	0.001	0.006	0.005	0.008

[a] Error due to propagating formal uncertainties on the stellar parameters.

[b] Statistical error reflected in the line-to-line scatter of derived abundances.

[c] Abundances and errors quoted are the weighted mean of the results for two ionization states.

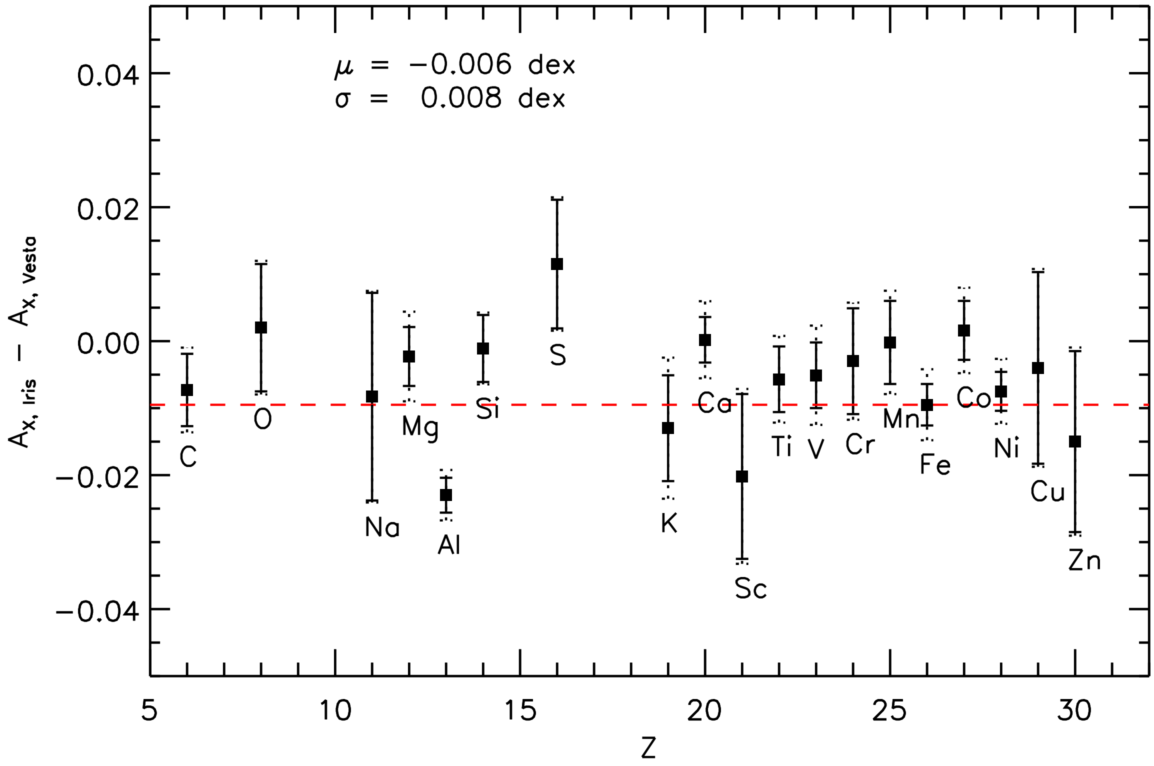

Figure 5.4 Differential abundances for Iris and Vesta data from the MIKE instrument. Error bars and red line as in Figure 5.2.

Table 5.6 Stellar abundances [X/H] for MIKE Iris - Vesta.

Element	[X/H]$_{Iris}$	$\Delta T_{\rm eff}$	Δlog g	Δv_t	Δ[M/H]	param^{a}	obs^{b}	total
		+5K	+0.01 dex	+0.01 km s^{-1}	+0.01 dex			
	(dex)	(dex)	(dex)	(dex)	(dex)	(dex)	(dex)	(dex)
C	-0.008	-0.002	0.002	0.000	-0.001	0.003	0.007	0.008
O	0.002	-0.003	0.000	0.000	0.000	0.003	0.010	0.011
Na	-0.008	0.003	0.000	-0.000	0.001	0.003	0.015	0.016
Mg	-0.002	0.004	-0.001	-0.002	0.001	0.005	0.004	0.007
Al	-0.023	0.002	-0.001	-0.001	0.001	0.003	0.003	0.004
Si	-0.001	0.001	0.001	-0.000	0.001	0.002	0.005	0.005
S	0.011	-0.002	0.002	0.000	-0.000	0.003	0.010	0.010
K	-0.013	0.005	-0.003	-0.001	0.004	0.007	0.008	0.011
Ca	0.000	0.004	-0.002	-0.002	0.001	0.005	0.003	0.006
Sc^{c}	-0.020	0.002	0.002	-0.001	0.002	0.004	0.012	0.013
Ti^{c}	-0.006	0.002	0.002	-0.002	0.002	0.004	0.005	0.006
V	-0.005	0.005	0.001	-0.000	0.001	0.006	0.005	0.008
Cr^{c}	-0.003	0.003	0.000	-0.002	0.002	0.004	0.008	0.009
Mn	-0.000	0.004	-0.002	-0.003	0.002	0.005	0.006	0.008
Co	0.002	0.004	0.001	-0.001	0.002	0.004	0.005	0.007
Ni	-0.007	0.003	-0.000	-0.002	0.002	0.004	0.003	0.005
Cu	-0.003	0.003	-0.001	-0.002	0.002	0.004	0.015	0.015
Zn	-0.015	0.001	0.000	-0.003	0.002	0.004	0.014	0.014
Fe^{c}	-0.009	0.003	0.000	-0.002	0.002	0.004	0.003	0.005

[a] Error due to propagating formal uncertainties on the stellar parameters.

[b] Statistical error reflected in the line-to-line scatter of derived abundances.

[c] Abundances and errors quoted are the weighted mean of the results for two ionization states.

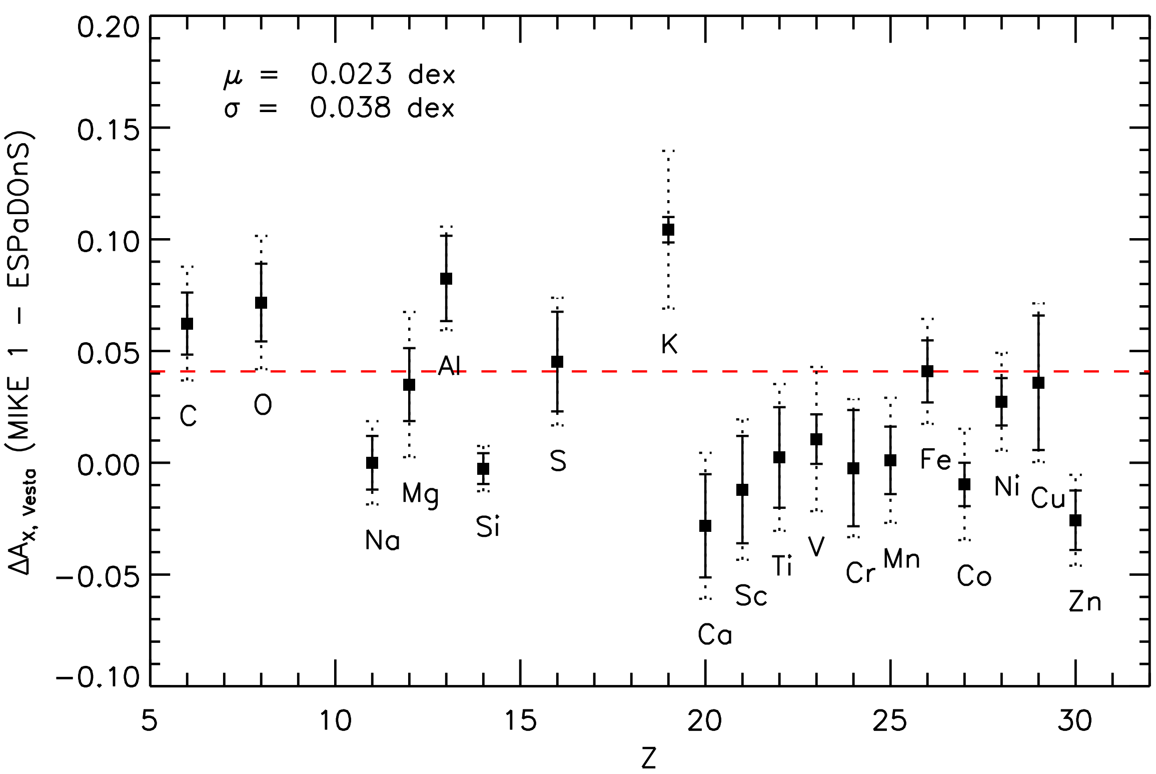

Figure 5.5 Differential abundances for Vesta data from MIKE (taken on 2011 June 24) and ESPaDOnS. Error bars and red line as in Figure 5.2. Note that the y-axis is rescaled compared to previous figures.

Table 5.7 Stellar abundances [X/H] for Vesta MIKE 1 - ESPaDoNS.

Element	[X/H]$_{Vesta}$	$\Delta T_{\rm eff}$	Δlog g	Δv_t	Δ[M/H]	param[a]	obs[b]	total
		+29K	+0.06 dex	+0.05 km s^{-1}	+0.02 dex			
	(dex)	(dex)	(dex)	(dex)	(dex)	(dex)	(dex)	(dex)
C	0.062	-0.016	0.014	-0.001	0.001	0.021	0.014	0.025
O	0.072	-0.023	0.006	-0.003	0.004	0.024	0.017	0.030
Na	0.000	0.014	-0.001	-0.001	-0.000	0.014	0.012	0.019
Mg	0.035	0.025	-0.007	-0.010	-0.001	0.028	0.016	0.033
Al	0.083	0.012	-0.004	-0.002	-0.000	0.013	0.019	0.023
Si	-0.003	0.006	0.003	-0.002	0.002	0.007	0.007	0.010
S	0.045	-0.013	0.012	-0.001	0.002	0.018	0.022	0.029
K	0.104	0.025	-0.022	-0.009	0.003	0.035	0.006	0.035
Ca	-0.028	0.019	-0.010	-0.008	0.001	0.023	0.023	0.033
Sc[3]	-0.012	0.006	0.017	-0.007	0.005	0.020	0.024	0.031
Ti[3]	0.002	0.022	0.006	-0.006	0.000	0.024	0.022	0.033
V	0.011	0.030	0.003	-0.002	-0.001	0.030	0.011	0.032
Cr[3]	-0.002	0.015	0.003	-0.007	0.001	0.017	0.026	0.031
Mn	0.001	0.023	-0.002	-0.006	-0.000	0.024	0.015	0.028
Co	-0.010	0.022	0.006	-0.001	0.000	0.023	0.010	0.025
Ni	0.027	0.017	-0.001	-0.009	0.002	0.019	0.011	0.022
Cu	0.036	0.017	0.002	-0.009	0.001	0.019	0.030	0.036
Zn	-0.026	0.004	0.004	-0.013	0.005	0.015	0.013	0.020
Fe[3]	0.041	0.015	0.002	-0.011	0.002	0.019	0.014	0.023

[a] Error due to propagating formal uncertainties on the stellar parameters.

[b] Statistical error reflected in the line-to-line scatter of derived abundances.

[c] Abundances and errors quoted are the weighted mean of the results for two ionization states.

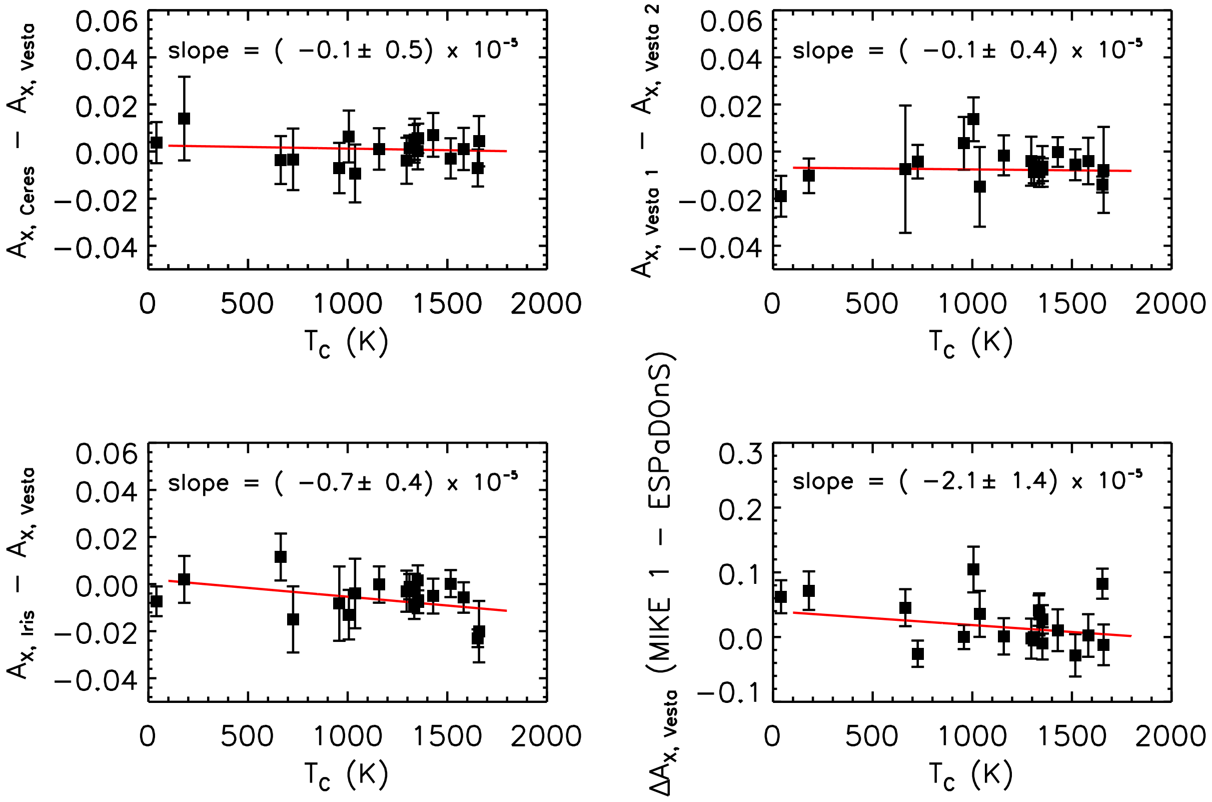

Figure 5.6 Differential abundances plotted against the 50 % condensation temperature from Lodders (2003). Linear fits to the data were performed using the total error bars as weights and are shown in red.

CHAPTER 6

COMPOSITIONS OF 80 SOLAR TWINS

In this chapter we present a spectroscopic analysis of the abundances of 17 elements in a set of 80 solar twin stars. All stars with HARPS spectra (whether from the Solar Twin Planet Search or from the online ESO archive) were included in this analysis. By combining the HARPS spectra, we achieve an average signal-to-noise ratio of 1000 at resolving power R = 115,000. Using these extremely high-quality spectra and applying a strictly differential equivalent width analysis technique, we are able to achieve abundance precisions on order 0.01 dex for most elements. We examine the results for elemental condensation temperature trends, a proposed tracer of planet formation and/or ingestion. We also find galactic chemical evolution (GCE) effects in the abundances measured for twins of different ages, and we quantify the impact of GCE on the condensation temperature trends.

Overall, we find that the Sun is enhanced in refractory elements relative to 92% of solar twins, although this result is only valid when the most volatile (and most difficult to accurately measure) elements are excluded from the analysis. A large star-to-star scatter exists in condensation temperature trends and we investigate possible origins of this. Meanwhile, among elements of similar origin such as the α group, all stars maintain a small scatter between abundances, as expected by GCE theory. In particular, the C/O and Mg/Si abundance ratios are extremely close to solar for all targets regardless of age.

6.1 Background

Is the Sun a typical star? This question has been a major driver behind stellar astronomy for centuries. Stellar spectra are commonly measured in comparison to the features of the solar spectrum, and stellar abundances derived relative to the solar composition. Special attention is paid to solar analogs and solar twins, or stars whose spectra most closely resemble that of the Sun (see e.g. Hardorp, 1978; Cayrel de Strobel, 1996). Such stars are scientifically interesting on multiple levels: not only do they represent closely adjacent alternate end states of our own Solar system, but also they allow us to extract the maximum possible amount of information about stellar compositions. The detailed physical processes of stellar atmospheres and their effects on spectral features remain poorly known, placing systematic limitations on our ability to extract compositional information from spectra of stars whose underlying physical proerties are different from the Sun (Asplund, 2005). The direct comparison of the Sun to its spectral twins effectively sidesteps these issues and enables us to measure highly precise relative stellar abundances.

In a differential spectroscopic study of eleven solar twins, Meléndez et al. (2009, hereafter M09) found that the Sun has an unusual abundance pattern characteristic of dust condensation. When comparing the Sun to the average solar twin, M09 observed a deficit of refractory elements relative to volatiles. This trend was quantified as a negative slope in abundance [X/H] as a function of T_{C}, the temperature at which an element is expected to condense under protoplanetary disk conditions (Lodders, 2003). This T_{C} trend has remained a topic of extensive debate, with some studies reproducing M09's findings and others refuting it for various samples of Sun-like stars (Ramírez et al., 2009, 2010; González Hernández et al., 2010, 2013; Gonzalez et al., 2010b; Gonzalez, 2011; Schuler et al., 2011b).

A myriad of explanations for T_{C} trends have been proposed. M09 suggested that the solar T_{C} trend may arise as a result of rocky planet formation. Chambers (2010) subsequently demonstrated that the Sun's refractory deficit corresponds to 4 Earth masses of terrestrial and chondritic material, confirming the plausibility of this explanation. While most studies have focused on potential links between T_{C} trends and planet formation, it is also likely that T_{C} behavior is affected by galactic chemical evolution (GCE) and thereby correlates with stellar age (Adibekyan et al., 2014; Nissen, 2015; Spina et al., 2016b). Alternative causes of the Sun's unusual T_{C} trend include gas-dust segregation in the protoplanetary disk and dust cleansing in the primordial nebula (Önehag et al., 2014; Gaidos, 2015).

In recent years, we have been conducting a radial velocity (RV) planet search on the

HARPS spectrograph on the ESO 3.6m telescope (Mayor et al., 2003). This search targets solar twin stars, with the aim of characterizing their planetary systems, ages, and stellar abundances at high precision to investigate potential causes of T_C trends in the sample. Further details of the sample are given in Ramírez et al. (2013). In this chapter, we present a detailed spectral analysis of 80 solar twins from our planet search program. We use stacked HARPS spectra with resolution R = 115,000 and average SNR $\sim$ 1000 per pixel at 600 nm. We achieve abundance precisions $\leq$ 0.01 dex for 17 elements in most sample stars.

In sections 6.2 and 6.3, we detail the data reduction and analysis methods. Section 6.4 addresses the correlations between elemental abundances and stellar age due to GCE. We then discuss the spread of C/O and Mg/Si abundance ratios and T_C trends in the sample in Sections 6.5 and 6.6. We summarize our findings in Section 6.8.

6.2 Data

The spectra used in this analysis were created by stacking all HARPS observations of a given star from our program and from the public ESO Science Archive Facility.[1] The HARPS pipeline provides extracted 1-dimensional spectra and radial velocity information automatically. Using these data products, we Doppler-corrected, continuum normalized, and stacked all spectra to create a very high SNR composite spectrum. This procedure was done slightly differently for the blue ($378 < \lambda < 530$ nm) and red ($533 < \lambda < 691$ nm) CCD chips. The blue chips were automatically continuum normalized using a 20th-order polynomial fit in IRAF's `onedspec.continuum` module.[2] The red chips, which are more strongly affected by wide bands of telluric absorption lines, were hand-fit in interactive mode. In either case,

---

[1] Data were used from ESO programme IDs 072.C-0488, 074.C-0364, 075.C-0202, 075.C-0332, 076.C-0155, 077.C-0364, 088.C-0323, 089.C-0415, 089.C-0732, 090.C-0421, 091.C-0034, 091.C-0936, 092.C-0721, 093.C-0409, 095.C-0551, 096.C-0499, 097.C-0090, 097.C-0571, 097.C-0948, 183.C-0972, 183.D-0729, 185.D-0056, 188.C-0265, 192.C-0224, 192.C-0852, 289.C-5053, 292.C-5004, and 60.A-9036.

[2] IRAF is distributed by the National Optical Astronomy Observatory, which is operated by the Association of Universities for Research in Astronomy (AURA) under cooperative agreement with the National Science Foundation.

efforts were made to ensure that all spectra were normalized similarly across stars, since our differential equivalent width technique is more sensitive to star-to-star differences than it is to absolute continuum slopes.

Combined spectra for a total of 80 targets were created in this manner. We excluded two of the 82 stars with HARPS spectra in Table 4.1, HIP19911 and HIP103983, because careful inspection of their line profiles indicates that they are actually double-lined spectroscopic binaries (dos Santos et al., 2017). The combined spectra of the remaining stars varies in quality depending on the brightness of the target and the number of HARPS spectra observed, but on average an SNR of approximately 1000 pix^{-1} at 600 nm is achieved (Figure 6.1). The HARPS spectra have resolution R = 115,000 and wavelength coverage between 378 and 691 nm.

The solar reference spectrum used in this work was created by combining multiple exposures of sunlight reflected from the asteroid Vesta. The resulting spectrum has an SNR well above 1000 pix^{-1} at 600 nm. It was continuum-normalized in the same manner as the target spectra.

Spectra previously obtained with the MIKE spectrograph and used in Ramírez et al. (2013) were also used in some parts of the analysis (Bernstein et al., 2003). These spectra have SNR $\sim$ 400 pix^{-1} at 600 nm, resolution R = 83,000 - 65,000 (on blue/red CCDs), and wavelength coverage between 320 and 1000 nm.

6.3 Spectroscopic Analysis

6.3.1 Fundamental Stellar Parameters

Stellar fundamental parameters ($T_{\rm eff}$, $\log g$, and [Fe/H]) were obtained using the differential equivalent widths of FeI and FeII features with the method detailed in Chapter 5. While most of these targets were already characterized in this manner by Ramírez et al. (2013) using MIKE spectra, we chose to re-do the analysis using the HARPS spectra due to their superior

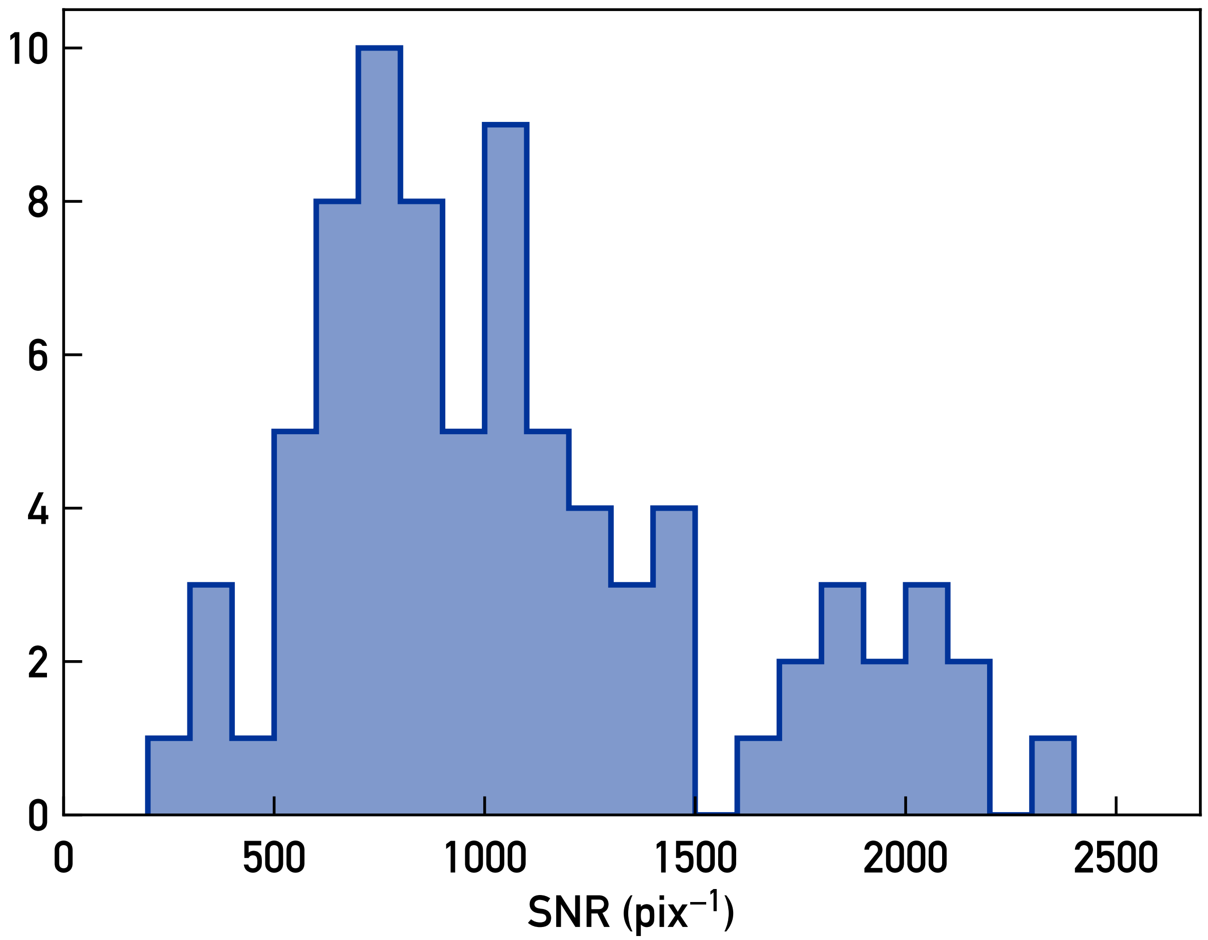

Figure 6.1 Estimated SNR per pixel at 600 nm after co-adding all available HARPS spectra of each target.

quality and minor concerns about the quality of the MIKE data. Our new HARPS-based parameters are in good agreement with those obtained by Ramírez et al. (2013) but have significantly higher precision. A more detailed comparison will be presented in a forthcoming paper (Spina et al. in prep).

6.3.2 Elemental Abundances

Also using a strictly differential equivalent width method, we measured the abundances of 17 elements in each spectrum: C, O, Na, Mg, Al, Si, S, Ca, Sc, Ti, V, Cr, Mn, Co, Ni, Cu, and Zn. The line line was adapted from our previous works including **?** and Ramírez et al. (2014b). Hyperfine structure corrections were applied for V, Mn, Co, and Cu. The computation of abundances was done with q^2, a python wrapper for MOOG (Sneden, 1973).[3] Final abundances for each element were obtained by taking an average of the differential abundance from each line. Uncertainties on these abundances come from the standard error on the mean, added in quadrature with the propagated effects of the uncertainties on the fundamental parameters.

Three elements in addition to iron were measured in multiple ionization states (TiI/TiII, ScI/ScII, CrI/CrII). As expected, the abundances of the two species agree within the uncertainties for most stars (Figure 6.2).

The abundances of C and O are especially tricky as few spectral features are available for these elements, and yet both are elements of high astrophysical interest. We therefore paid special attention to testing these abundance results as much as possible. In the HARPS spectra, lines of both CI and CH fall within the wavelength range, but no uncontaminated oxygen features are present. The MIKE spectra from Ramírez et al. (2013), however, do extend far enough into the infrared to include the triple oxygen feature at 777 nm. We measured oxygen abundances from the MIKE spectra and applied the NLTE corrections of Ramírez et al. (2007).

---

[3] `http://github.com/astroChasqui/q2`

Since our analysis is strictly differential and we always employ as a reference the solar EWs measured by the same instrument as the target EWs, we do not expect a significant bias when comparing abundances derived from the MIKE spectra versus the HARPS spectra. Nevertheless, we sought to test this assumption by comparing the CI and CH abundances obtained from measuring the same lines in both spectra. Figure 6.3 shows the results. CH abundances agree quite well between the two instruments. The dispersion in CI is much greater, especially in MIKE, which is likely a result of the difficulty in measuring the CI lines: our CI line list contains only lines with $\mathrm{EW}_\odot \lessapprox 30$ mÅ, which is challenging to measure accurately even at the high resolution of HARPS and especially at the lower resolution of MIKE. The CI abundances are systematically higher than CH in the high-[C/H] regime regardless of the instrument, which is an unexpected and as-yet unexplained result.

For the purposes of our analysis, we chose to consider all CI and CH lines from HARPS when computing the carbon abundances, and used the MIKE triplet for oxygen.

6.3.3 Stellar Ages

We obtained age estimates for all stars using isochrone fits. A joint fit was performed using our measured T_{eff}, $\log g$, and [Fe/H] as well as the absolute V magnitude inferred from parallaxes. *Gaia* DR1 photometry and parallaxes were used when available (Gaia Collaboration et al., 2016b,a); data for the other stars came from the All-Sky Compiled Catalogue and Tycho-2 (Kharchenko & Roeser, 2009; Høg et al., 2000). We additionally applied metallicity corrections from the [α/H] abundances using MgI as a proxy for α. More detail can be found in a forthcoming paper (Spina et al. in prep).

6.4 Chemical Evolution with Stellar Age

Using the precise stellar ages and abundances of the sample, we investigated the dependence of abundance ratios [X/Fe] on age. As shown in Figure 6.4, remarkably tight trends can

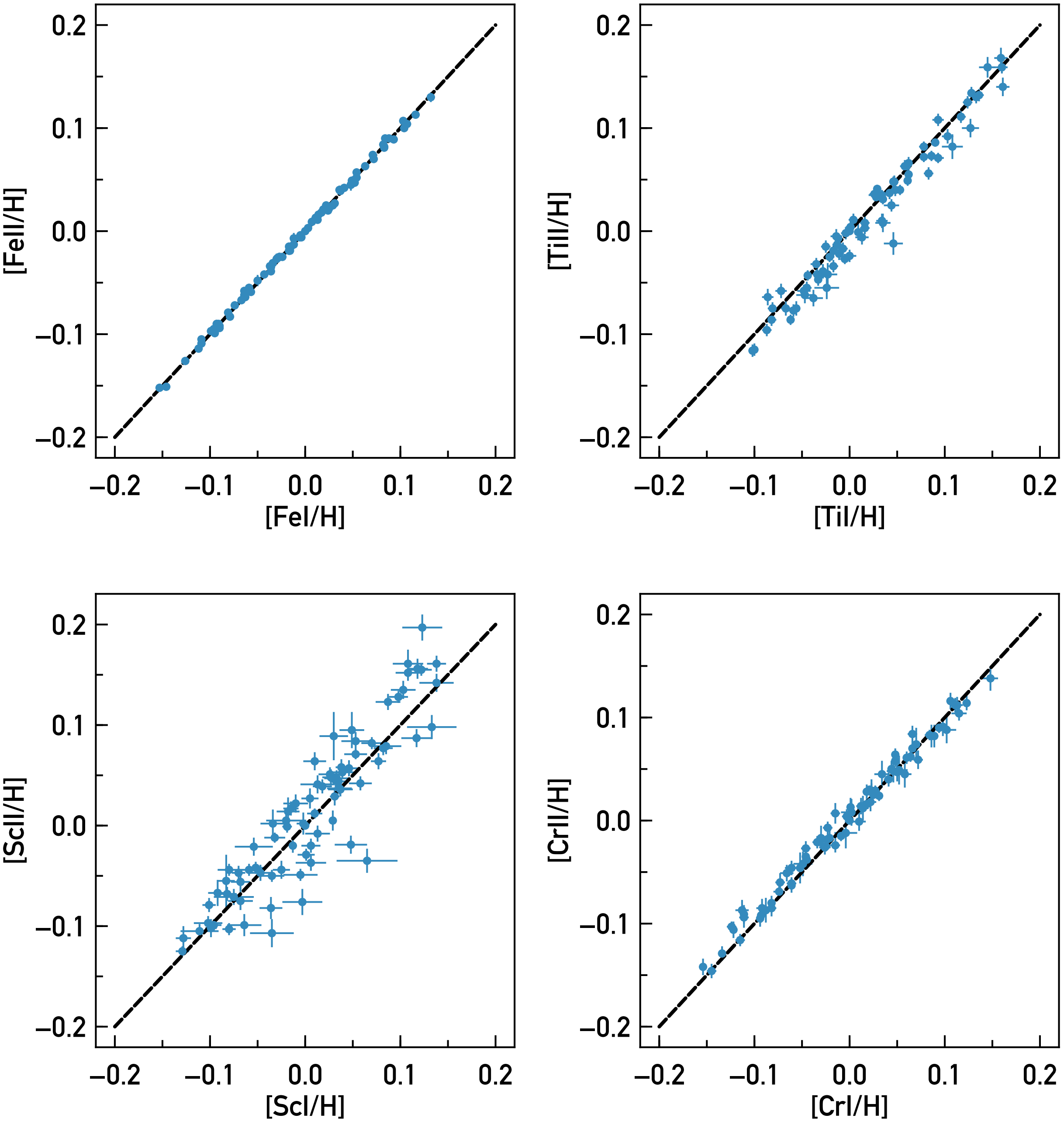

Figure 6.2 Comparison of inferred abundances of an element obtained from measuring different ionization states. Ionization balance of FeI and FeII (top left) is maximized in the process of setting the stellar fundamental parameters, particularly log g. The other elements plotted here (Ti, Sc, and Cr) were not considered when setting the stellar parameters, but should be balanced within the uncertainties if the parameters are accurate.

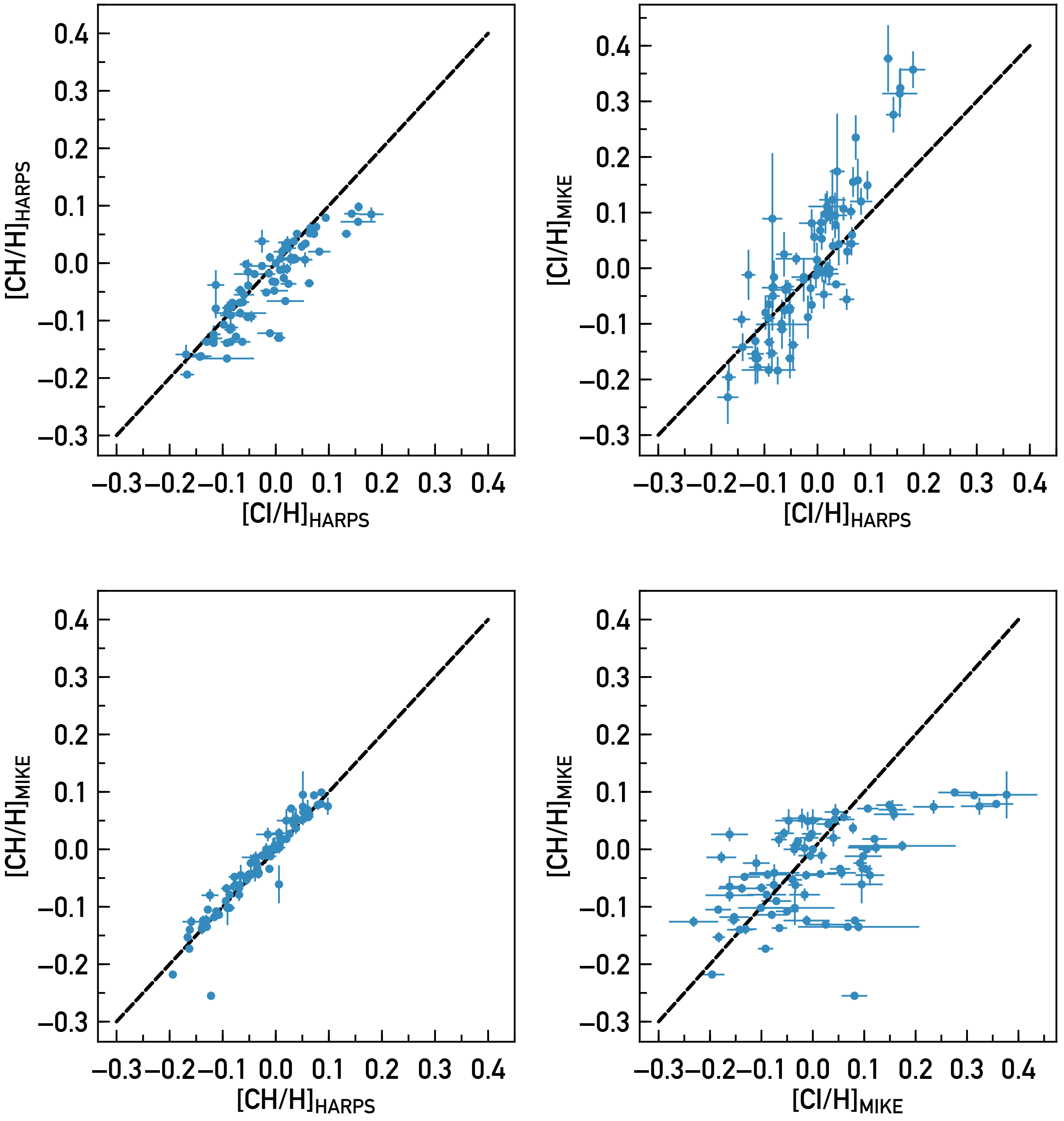

Figure 6.3 Comparison of carbon abundances obtained from CI and CH species in HARPS and MIKE spectra.

be seen for many elements, reflecting the chemical evolution of the local galaxy through time. As done in previous works (e.g. Adibekyan et al., 2016; Nissen, 2015; Spina et al., 2016a), we fit these trends with a linear model. Ten stars with ages above 8 Gyr and a visible enhancement in α elements were excluded from the fits. These apparently belong to a different population, perhaps originating in the thick disk, and are not well-fit by our linear relationships.

The linear models were fit using the objective function derived by Hogg et al. (2010) for the case of non-negligible measurement uncertainties in both (x, y) variables. In brief, we minimize the orthogonal distances between the linear model and each data point weighted by the data uncertainties. We assume no covariance in these uncertainties. We additionally incorporate a "jitter" or white-noise term added in quadrature with the measurement uncertainties, accounting for the intrinsic star-to-star scatter in abundances. The resulting model has three free parameters for each element: abundance-age slope m, intercept b, and intrinsic scatter s. We find best-fit values using the BFGS algorithm as implemented in the `scipy.optimize.minimize` module, and uncertainties from an MCMC using `emcee` with flat priors on all parameters.

For four elements (C, Ti, Sc, and Cr), abundances were measured using multiple ionization or molecular states. In principle the linear fits should be identical across states. In reality, though, the limited line lists used and systematics-prone nature of spectroscopic analyses mean that different degrees of scatter and even systematic offsets could be present between multiple species of the same element. To account for this possibility, we perform joint fits on the two species with slope m required to be the same and b, s allowed to be different for each one.

The resulting best-fit parameters and uncertainties are presented in Table 6.1. Our results generally agree well with previous works including Spina et al. (2016a) and Nissen (2015). We note that none of the elements which were measured in multiple species display a systematic offset in their b parameters beyond the level expected from random scatter.

Table 6.1 GCE Trend Parameters

Species	m (dex gyr^{-1})	b (dex)	s (dex)
CI	0.0114 ± 0.0015	-0.0829 ± 0.0085	0.0393 ± 0.0047
CH	0.0114 ± 0.0015	-0.0944 ± 0.0085	0.0303 ± 0.0033
OI	0.0084 ± 0.0015	-0.0250 ± 0.0082	0.0247 ± 0.0029
NaI	0.0087 ± 0.0015	-0.0615 ± 0.0082	0.0270 ± 0.0030
MgI	0.0098 ± 0.0009	-0.0364 ± 0.0049	0.0126 ± 0.0018
AlI	0.0138 ± 0.0009	-0.0592 ± 0.0053	0.0156 ± 0.0019
SiI	0.0062 ± 0.0006	-0.0305 ± 0.0034	0.0114 ± 0.0012
SI	0.0100 ± 0.0015	-0.0542 ± 0.0084	0.0239 ± 0.0036
CaI	-0.0009 ± 0.0006	0.0211 ± 0.0035	0.0098 ± 0.0011
ScI	0.0055 ± 0.0010	-0.0239 ± 0.0056	0.0155 ± 0.0020
ScII	0.0055 ± 0.0010	-0.0222 ± 0.0057	0.0223 ± 0.0030
TiI	0.0034 ± 0.0005	-0.0014 ± 0.0032	0.0118 ± 0.0013
TiII	0.0034 ± 0.0005	-0.0090 ± 0.0030	0.0122 ± 0.0016
VI	0.0014 ± 0.0006	-0.0026 ± 0.0036	0.0092 ± 0.0012
CrI	-0.0015 ± 0.0003	0.0092 ± 0.0019	0.0057 ± 0.0009
CrII	-0.0015 ± 0.0003	0.0129 ± 0.0019	0.0000 ± 0.0002
MnI	0.0024 ± 0.0011	-0.0315 ± 0.0059	0.0205 ± 0.0021
CoI	0.0071 ± 0.0010	-0.0454 ± 0.0059	0.0185 ± 0.0020
NiI	0.0069 ± 0.0010	-0.0501 ± 0.0051	0.0173 ± 0.0017
CuI	0.0146 ± 0.0018	-0.0849 ± 0.0102	0.0262 ± 0.0031
ZnI	0.0101 ± 0.0014	-0.0697 ± 0.0078	0.0223 ± 0.0027

The intrinsic scatter parameter s tends to be largest for those species whose line lists are very short, including NaI (4 lines), CuI (3 lines), OI (3 lines), and the carbon species. This is likely a reflection of the statistical tendency to underestimate uncertainties in the limit of small samples (Adibekyan et al., 2016). For elements with a more extensive list of easy-to-measure lines, like TiI and NiI (18 lines each), the intrinsic scatter remains significantly non-zero. This may be a reflection of the true degree of inherent deviations in individual stars from the GCE-predicted average abundance pattern.

6.5 C/O and Mg/Si Ratios

From a planet formation perspective, the range of possible carbon-to-oxygen and silicon-to-magnesium ratios among a sample of stars is a topic of keen interest. If, for example, a

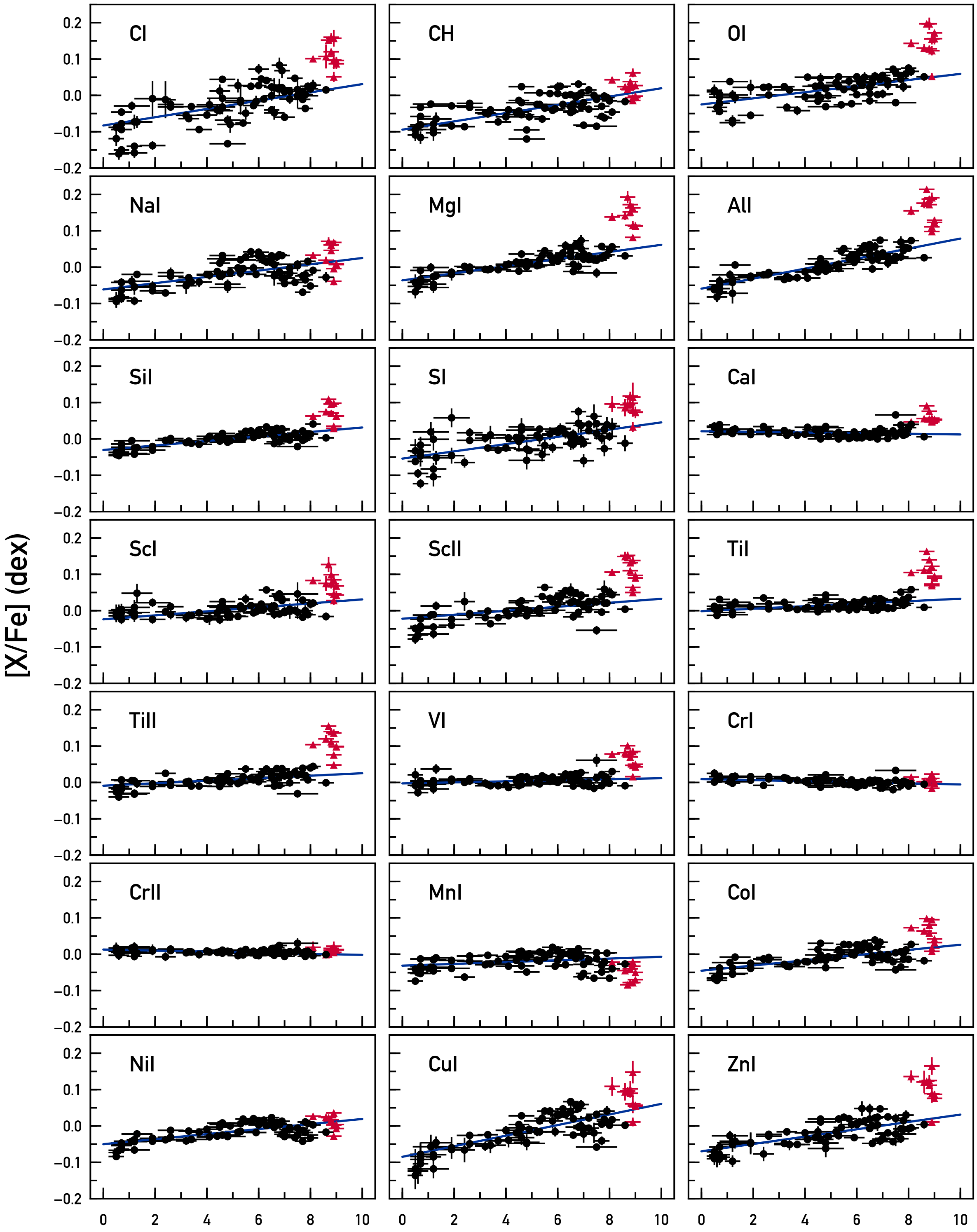

Figure 6.4 Abundances as a function of stellar age showing galactic chemical evolution in the sample. Black circles are stars included in the GCE trend fits; red squares are excluded. Blue lines are the best-fit linear trends.

significant population of stars form from gas with a primordial C/O ratio > 1, this could lead to carbon-rich planets, which would carry significant repercussions when interpreting the observed compositions of such planets' atmospheres (see e.g. Madhusudhan, 2012). Similarly, the Mg/Si ratio is a key parameter in models of rocky planet interior structure, with a Mg/Si ratio significantly below 1 or above 2 leading to non-Earth-like balances of compounds like pyroxine and olivine within the planet and potentially altering its geological processes (Sotin et al., 2007; Carter-Bond et al., 2012).

We calculated the abundance ratios C/O for each star:

$$C/O \equiv 10^{(A_C - A_O)} = 10^{([C/H]-[O/H])} \times 10^{(A_C^{\odot} - A_O^{\odot})}, \tag{6.1}$$

where A_X is the logarithm of the number density of atoms of element X normalized to the hydrogen density and $A_X^{\odot}$ is the solar value. Using the solar photospheric abundances from Asplund et al. (2009), we have:

$$C/O = 10^{([C/H]-[O/H])} \times 0.55. \tag{6.2}$$

Similarly, using the meteoritic values for Mg/Si (Lodders et al., 2009, and references therein):

$$Mg/Si = 10^{([Mg/H]-[Si/H])} \times 1.05. \tag{6.3}$$

The resulting distributions of C/O and Mg/Si ratios among the sample are shown in Figures 6.5 and 6.6 respectively. We find a much smaller range of observed C/O and Mg/Si ratios than in past works like Delgado Mena et al. (2010), Petigura & Marcy (2011), and Brewer & Fischer (2016). In particular, no stars in our sample have C/O beyond the range 0.4-0.6, and none have Mg/Si significantly below 1. Our results suggest that these key abundance ratios are quite similar across all Sun-like stars, implying that the formation of terrestrial planets with very non-Earth-like compositions may be rare.

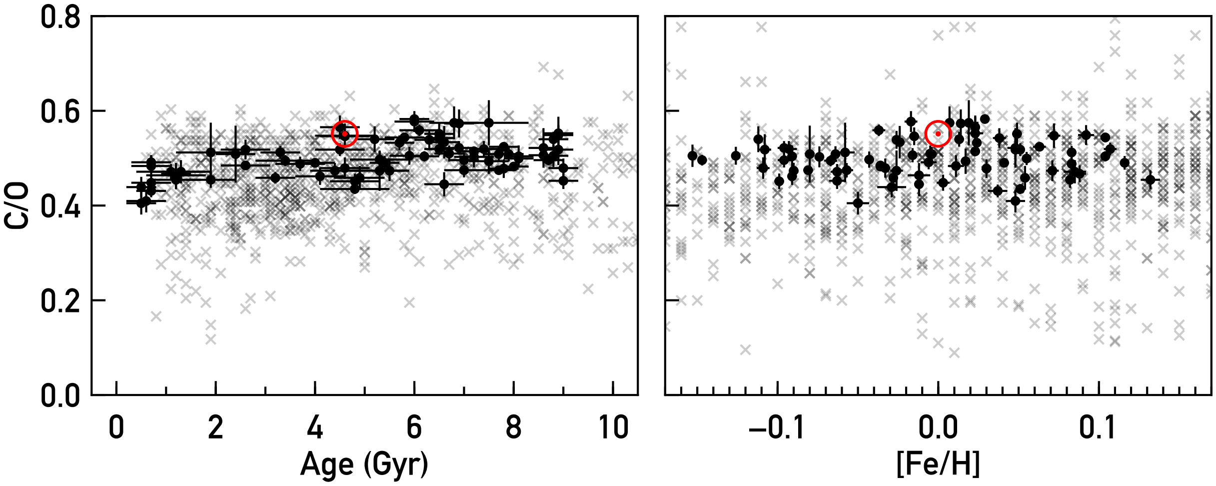

Figure 6.5 Carbon-to-oxygen ratio of solar twins (black circles) normalized to the solar value (0.55, red solar symbol on plot; Asplund et al., 2009), plotted as functions of age (left panel) and metallicity (right panel). Values from Brewer et al. (2016) are plotted as grey crosses for comparison.

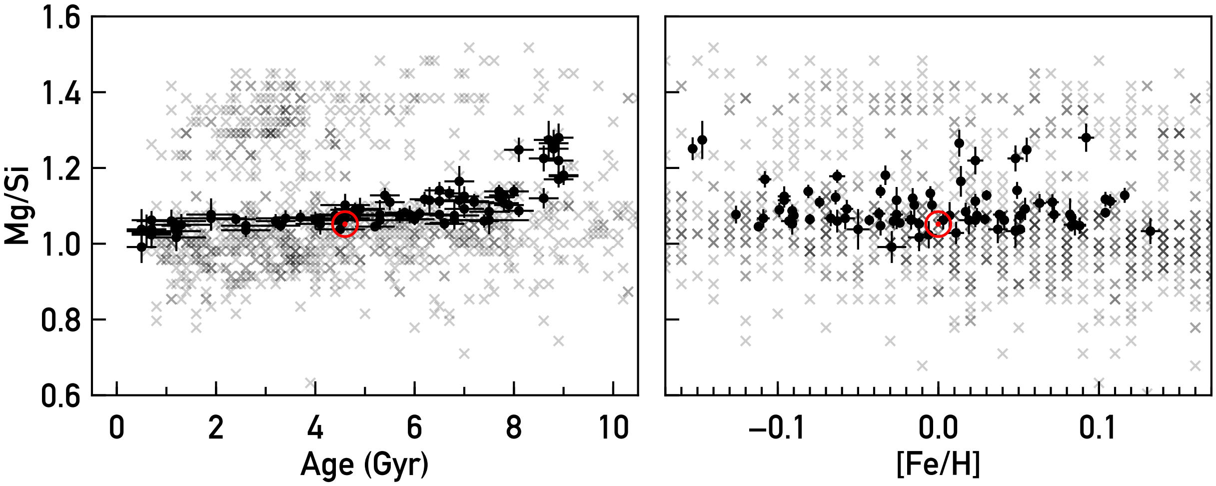

Figure 6.6 Magnesium-to-silicon ratio of solar twins (black circles) normalized to the solar value (1.05, red solar symbol on plot; Lodders et al., 2009), plotted as functions of age (left panel) and metallicity (right panel). Values from Brewer et al. (2016) are plotted as grey crosses for comparison.

We additionally consider the evolution of these abundance ratios with stellar age and/or metallicity. The C/O ratio appears to evolve very little, as predicted by the GCE simulation of Gaidos (2015) and in good agreement with past work by Nissen (2015)(Figure 6.5). Although the variance of C/O values is smaller than found in Brewer & Fischer (2016), the overall placement of the Sun at the high-C/O end of the distribution agrees well.

On the other hand, the Mg/Si ratio increases with age (Figure 6.6). This agrees with theory: while both Mg and Si are produced by alpha-capture processes in massive stars, there is also non-negligible Si production from Type Ia supernovae (e.g. Burbidge et al., 1957). In keeping with this ongoing Si production, we observe lower Mg/Si in younger stars than in the oldest sample stars. Adibekyan et al. (2015) found a similar effect when examining the Mg/Si ratio for stars across a wide range in metallicity, with the lowest [Fe/H] population exhibiting the largest Mg/Si. In this case, we see no significant correlation between [Fe/H] and Mg/Si, which is not surprising over such a small range in metallicity. Age is apparently a more sensitive tracer of the galactic evolution processes that shape the Mg/Si ratio.

6.6 Condensation Temperature Trends

We calculated T_{C} trends for every star in the sample by fitting a linear model to the [X/H] abundances and uncertainties with `scipy.optimize.minimize`. T_{C} values were adopted from Lodders (2003) calculations for solar system composition gas. For elements with multiple species available, a weighted average was done to achieve an estimate of the overall elemental abundance.

Since GCE effects may have an impact on the T_{C} slopes of stars, we repeated this analysis on the stars after subtracting the GCE trends fit in Section 6.4. This should in principle account for much of the variation in primordial compositions of the protostellar nebulae from which these stars formed, making any secondary compositional effects from e.g. planet formation processes easier to see.

The resulting distribution of T_{C} slopes in the sample is shown in Figure 6.7. A relatively wide range of slopes is seen regardless of whether GCE corrections have been applied. For comparison, we fit the “average solar twin” abundance pattern derived by M09 using the same linear model and find a slope of $(3.8 \pm 0.8) \times 10^{-5}$ dex K^{-1}. In contrast, we find that the median T_{C} slope among the sample lies at 0.7×10^{-5} dex K^{-1} before GCE corrections or 1.3×10^{-5} dex K^{-1} after. The T_{C} slope distribution is wide enough to easily encompass both the M09 value and the solar value (0.0 by definition). In other words, while the M09 result falls well within the range of observed solar twin composition patterns, the expected distinction between Sun-like abundance patterns and M09-like abundance patterns is not borne out in our sample. Instead, the Sun appears to be a typical star, albeit somewhat more refractory-poor than average.

Why do our results differ from M09 so strongly? The M09 sample only consisted of 11 solar twins, but their result is unlikely to stem from statistics alone: a bootstrap simulation drawing 11 stars randomly from our larger sample finds an average solar twin T_{C} slope at or above the level of M09 in fewer than 3% of all trials. A major component of the discrepancy appears to lie in the volatile elements. As shown in Figure 6.8, the average oxygen and sulfur abundances found in this work are significantly lower than M09's values. These elements have an outsized effect on the T_{C} slope due to the relative scarcity of low-T_{C} species. OI and SI are also among the most difficult species to measure: we used the OI triplet from the MIKE spectra and measured SI from four lines which are all composed of several blended components.

There may be additional systematic effects present in M09's volatile element abundances due to the stellar parameters used. We examined nine stars which overlap between the M09 sample and the twins used in this work and found that the T_{eff} values adopted were higher in M09 with a median difference of 27 K. This not only alters the volatile [X/Fe] abundances, but it also changes the NLTE corrections applied to oxygen. The net effect from such a temperature difference can explain the 0.07 dex total decrease in oxygen abundance from M09 to the present work.

Whatever the cause, it is clear that the volatile element abundances are challenging to measure and have a disproportionate effect on the $T_{\rm C}$ slopes found. To mitigate this issue, we repeated the analysis considering only the elements with $T_{\rm C} > 800$ K and fit slopes to the more steeply inclined refractory end of the overall $T_{\rm C}$ trend. These elements have more robust line lists and are less sensitive to minor changes in the stellar parameters. We find good agreement between the results in this work and M09 for the refractory-only $T_{\rm C}$ slopes (Figure 6.9).

In particular, among the GCE-corrected refractory-only $T_{\rm C}$ slopes, only six solar twins or about 8% of the sample have a slope at or below the solar trend. This implies that the Sun is depleted in refractory elements relative to 92% of Sun-like stars in the solar neighborhood.

6.7 $T_{\rm C}$ Trends and Stellar Properties

To investigate potential origins of the solar abundance pattern, we turn to other measured properties of the solar twin sample and search for correlations with $T_{\rm C}$ slope. One commonly proposed factor in shaping $T_{\rm C}$ trends is the stellar age. Adibekyan et al. (2014), Ramírez et al. (2014a), and Nissen (2015) all found some degree of correlation between $T_{\rm C}$ slope and stellar age for samples ranging from 21 to 148 Sun-like stars. The magnitude and even direction of these correlations, however, vary between different samples, leaving the reality and underlying mechanisms of the relationship between $T_{\rm C}$ slope and stellar age unresolved.

Figures 6.10 and 6.11 show the $T_{\rm C}$ slopes of the sample relative to their isochrone ages. Even before GCE corrections are applied to the abundances, there is no significant relationship seen. The only exception to this result is in the refractory-only $T_{\rm C}$ slopes of the oldest stars in the sample, which are systematically higher than the rest of the sample. This is likely to be an artifact of the strong α-element enrichment seen in these stars (Figure 6.12). When the volatile elements C and O are included in the $T_{\rm C}$ fit there is an α-enhancement at both low and high $T_{\rm C}$ resulting in little net change in the slope; however, when these elements are excluded the most enhanced elements are clustered at high $T_{\rm C}$ so that the

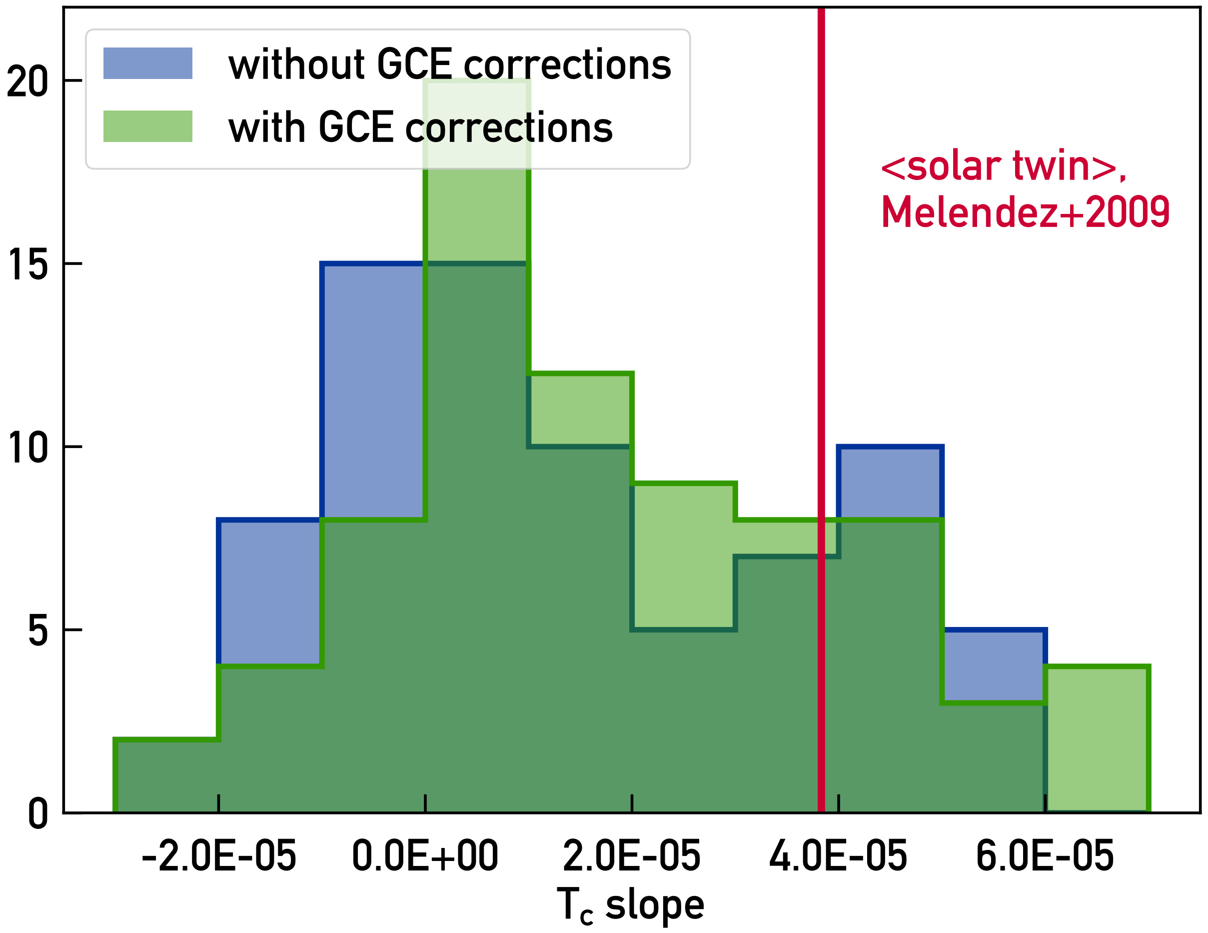

Figure 6.7 Distribution of T_C slopes for the sample before (blue) and after (green) GCE correction. The "average twin" slope found in the analysis of Meléndez et al. (2009) is marked in red. The solar T_C slope is zero by definition.

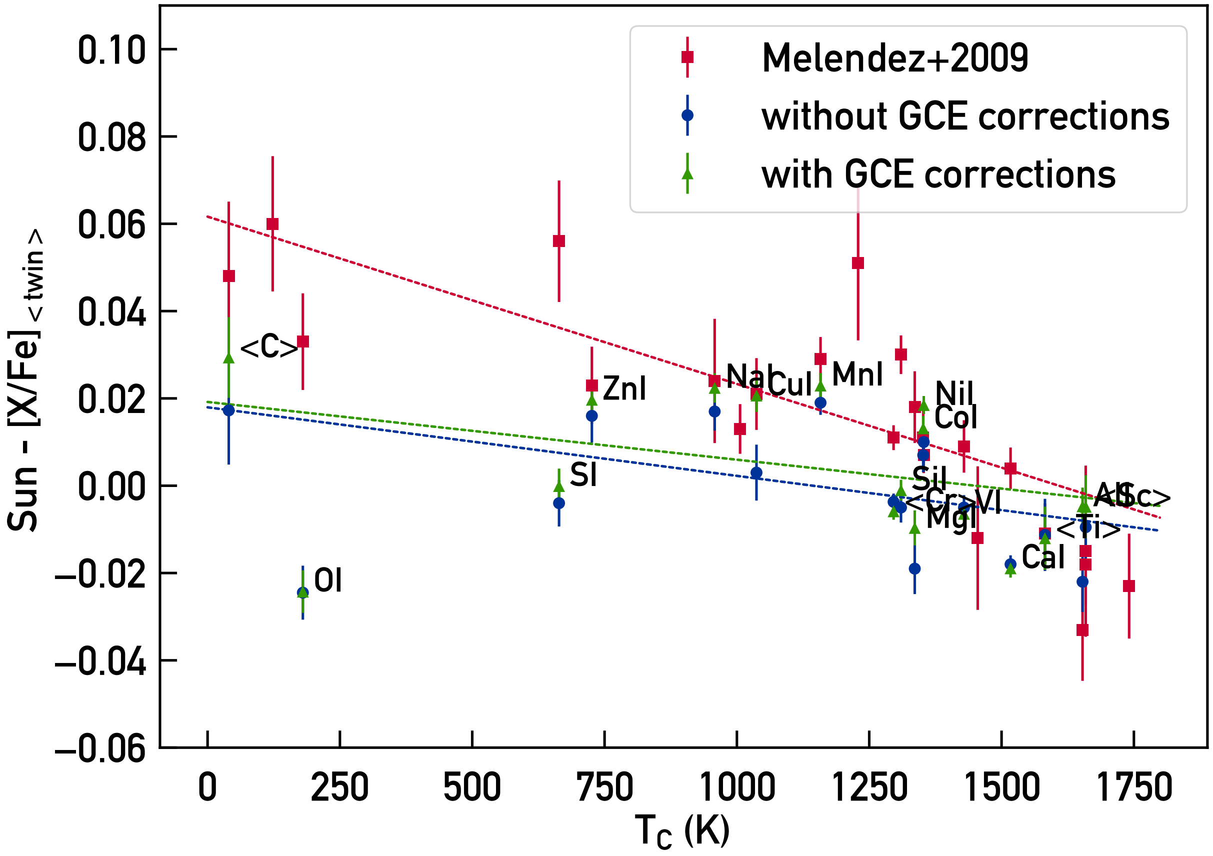

Figure 6.8 Condensation temperature trend of the Sun relative to the average solar twin. Results from Meléndez et al. (2009) are marked as red squares. Results from this work are shown before (blue circles) and after (green triangles) applying GCE corrections.

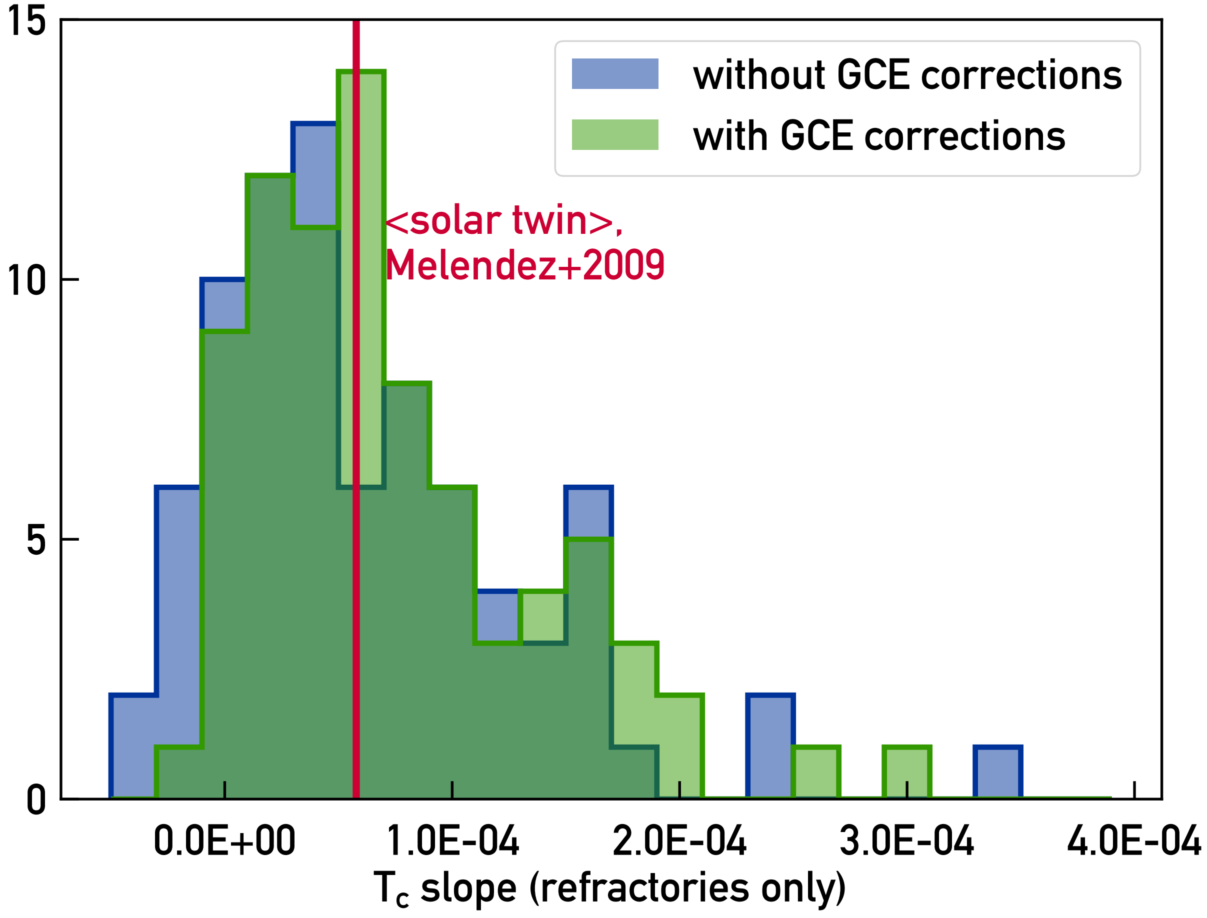

Figure 6.9 Same as Figure 6.7 for T_C slopes fit only to elements with $T_C > 800$ K.

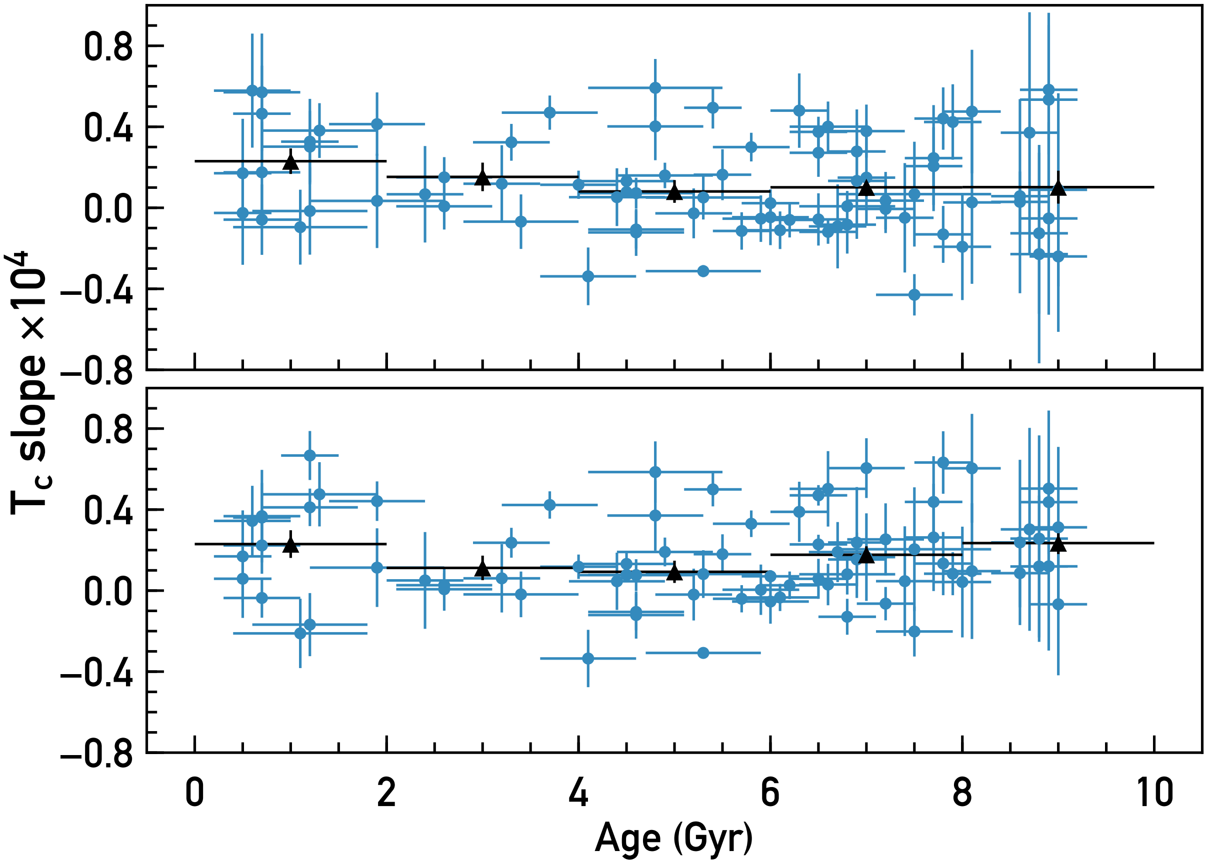

Figure 6.10 T_C slopes as a function of stellar age before (upper) and after (lower) GCE correction marked in blue circles. Data binned by 2 Gyr intervals are marked by black triangles.

slope is strongly affected. Our GCE relations did not attempt to fit this enhancement in the oldest population, so applying GCE corrections cannot resolve this issue. Given the large element-to-element scatter around the best-fit T_C trend, we do not consider this effect to be a true reflection of dust condensation behavior in the old solar twin systems.

We also considered the possibility that binary companions could shape the T_C trend. Radiation and gravitational pull from a nearby companion star could conceivably affect the lifetime of the protoplanetary disk or the stability of planets formed around a star. To test this, we divided the sample into stars with strong RV trends indicative of a companion and stars without such trends (see Section 4.1 for details on the RV analysis). The T_C slopes are not significantly different between these two samples (Figure 6.13), implying that binary

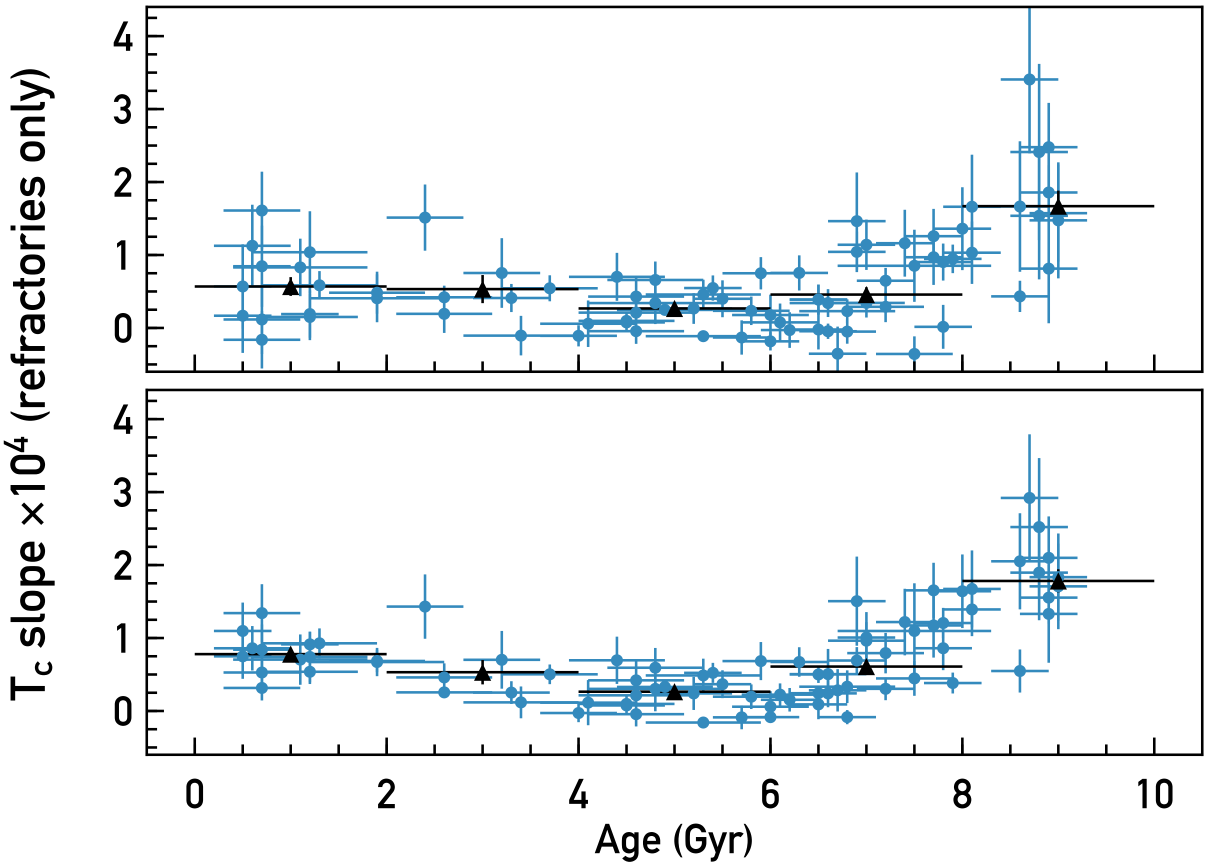

Figure 6.11 Same as Figure 6.10 for T_C slopes fit only to elements with $T_C > 800$ K.

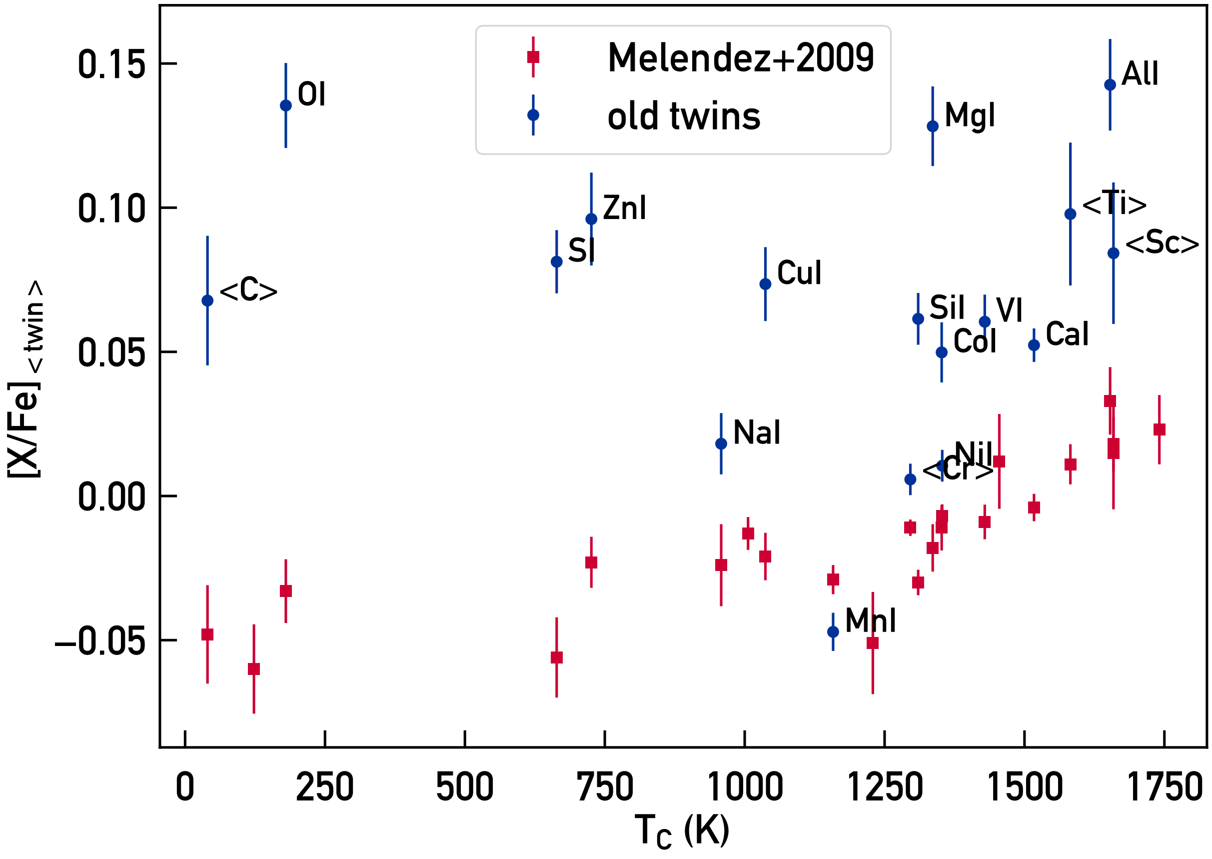

Figure 6.12 Condensation temperature trend of the oldest solar twins (blue circles) relative to the average twin abundance pattern from M09 (red squares).

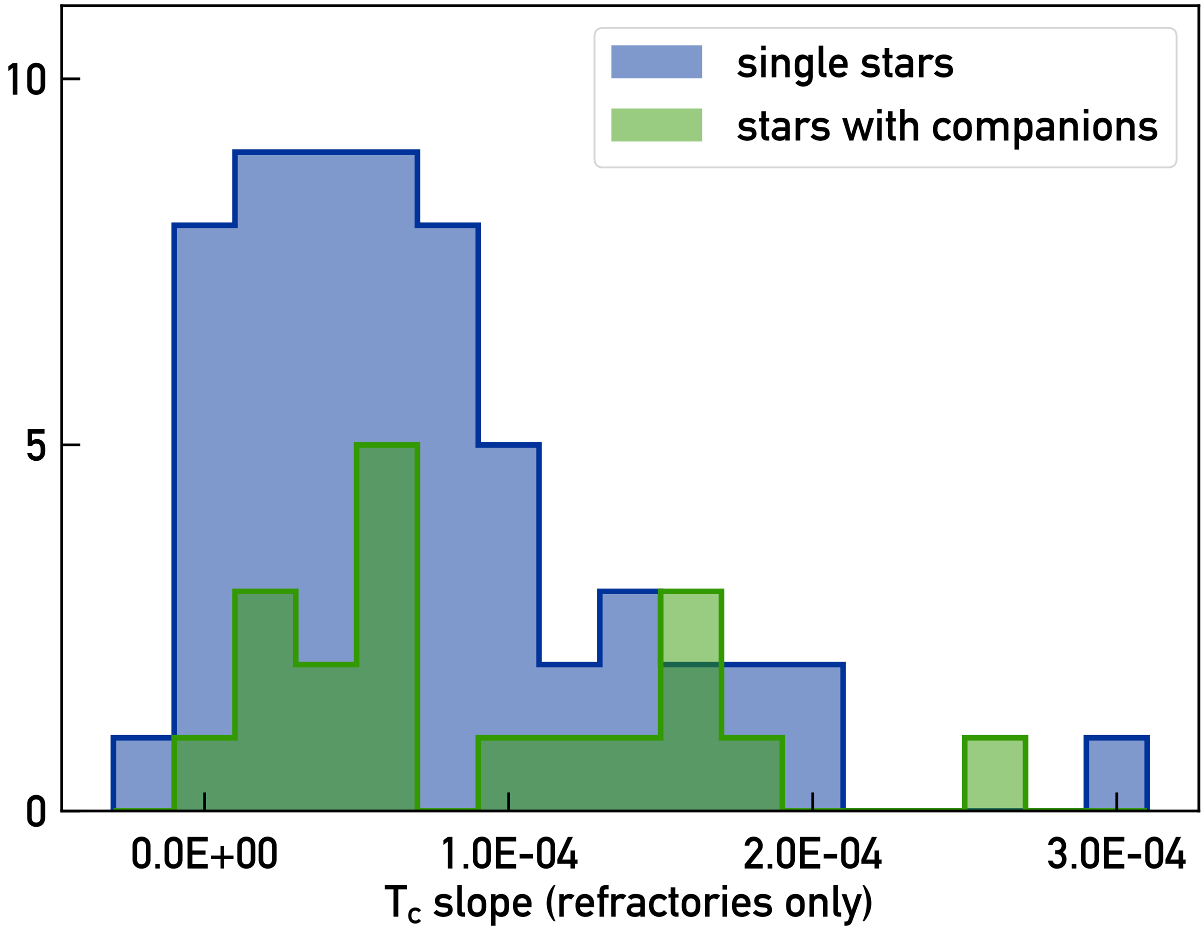

Figure 6.13 Distribution of refractory-only, GCE-corrected T_C slopes for HARPS-monitored stars with and without RV trends indicative of close companions (see Section 4.1).

companions are not a primary source of scatter in the T_C slopes of the sample.

Perhaps the most interesting, and the most difficult to investigate, of all T_C trend theories is the potential link between stellar abundances and planet formation history. One hypothesis along these lines, proposed by M09 among others, is that stars hosting terrestrial planets like Earth are depleted in refractory materials as a result of planet formation. As extensively discussed in Chapter 4, it is beyond our current capabilities to detect Earth-mass planets at Earth-like orbital periods, but we can in some cases infer the *lack* of such planets. *Kepler* has demonstrated that most stars have planets of some kind. Assuming that this is true of our sample, to first order we might regard the RV RMS as a measurement of how inhospitable a system is to Earths: the more scatter there is among the RVs, the more massive and the more close-in planets in the system are, meaning that a small planet is less likely to have retained a dynamically stable orbit within the habitable zone throughout the system's history. This does, of course, rely on signals due to very long-period companions or stellar astrophysics having been previously removed from the RVs.

Using this assumption, we examined separately the low-RMS and high-RMS stars from the activity-quiet HARPS subsample as laid out in Section 4.5. Figure 6.14 compares the two populations. Both are consistent with being randomly drawn from the full sample. This does not by any means rule out a connection between planet populations and T_{C} trends, but if any such connection does exist it will require more advanced planet detection capabilities to discern. We remain optimistic that such studies will be possible in the near future from a combination of further RV monitoring, data from future missions like *TESS* and *Gaia*, and continued work on the filtering of stellar activity signals from the RVs of Sun-like stars.

6.8 Conclusion

In this chapter, we have analyzed the abundances of 17 elements in 80 solar twin stars, achieving a typical precision of 0.01 dex. With this unprecedentedly large and precise sample we are able to characterize several important aspects of stellar abundances, including the effects of galactic chemical evolution and the behavior of the elements as a possible result of dust condensation. We demonstrate that the solar abundance pattern does indeed show a relative depletion in refractory materials as a function of T_{C}, as first suggested by M09; however, we caution that these effects can become obscured by possible systematic errors in the abundances of volatile elements including carbon, oxygen, and sulfur. We recommend focusing on the abundances of refractory elements only ($T_{\mathrm{C}} < 800$ K) when searching for robust trends in abundances with condensation temperature.

While the exact causes of the variations in T_{C} trends seen in this work remain unclear,

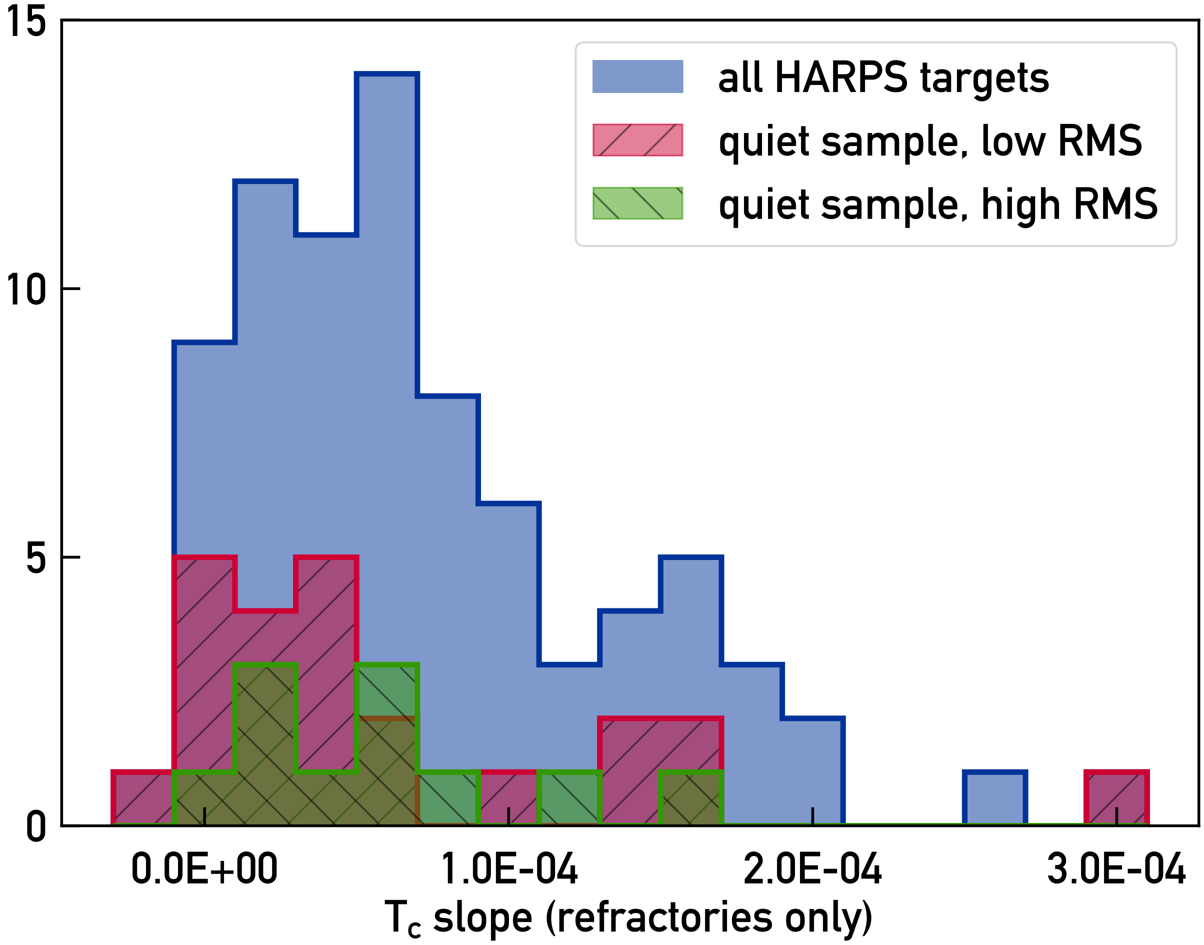

Figure 6.14 Distribution of refractory-only, GCE-corrected T_C slopes for HARPS-monitored stars. Targets from the activity-quiet subsample (see Sections 4.1, 4.5) appear consistent with the underlying population regardless of their RV behavior.

we look forward to the insights that better knowledge of these stars' planetary systems may bring in the future.

CHAPTER 7

KEPLER-11: AN UNEXPECTED SOLAR TWIN

In this chapter we present an analysis of the Kepler-11 system.[1] The six planets of the Kepler-11 system are the archetypal example of a population of surprisingly low-density transiting planets revealed by the *Kepler* mission. We determine the fundamental parameters and chemical composition of the Kepler-11 host star to unprecedented precision using an extremely high quality spectrum from Keck-HIRES (R$\simeq$67,000, S/N per pixel$\simeq$260 at 600 nm). Contrary to previously published results, our spectroscopic constraints indicate that Kepler-11 is a young main-sequence solar twin. The revised stellar parameters and new analysis raise the densities of the Kepler-11 planets by between 20-95% per planet, making them more typical of the emerging class of "puffy" close-in exoplanets. We obtain photospheric abundances of 22 elements and find that Kepler-11 has an abundance pattern similar to that of the Sun with a slightly higher overall metallicity. We additionally analyze the *Kepler* lightcurves using a photodynamical model and discuss the tension between spectroscopic and transit/TTV-based stellar density estimates.

7.1 Background

Five years after their initial discovery, the six planets of the Kepler-11 system remain a crown jewel of *Kepler* science results (Lissauer et al., 2011, hereafter L11). All six planets orbit a Sun-like host star with low eccentricies in a largely co-planar, tightly packed configuration. The formation and long-term stability of the system remains an open question (see e.g. Ikoma & Hori, 2012; Hands et al., 2014; Mahajan & Wu, 2014). Kepler-11 is regarded as the prototypical example of a system of tightly-packed inner planets, a class of *Kepler* multi-planet systems which offers a surprising counterpoint to our own solar system's more widely spaced architecture. Given the low geometric probability of finding a six-planet transiting

---

[1] This chapter is adapted from Bedell et al. (2017).

system, Kepler-11 is a valuable and rare opportunity to study in detail a potentially common population of exoplanets.

In addition to their unusually tight system architecture, the Kepler-11 planets are noteworthy in another sense: their measured masses and radii place them among the lowest-density super-Earths known to date. Transit timing variations (TTVs) have been measured for all six planets. In the discovery paper, L11 derived mass constraints for the five inner planets based on TTVs from six quarters of *Kepler* data. Migaszewski et al. (2012) reanalyzed the same data using a photodynamical model and found similar results, with an additional constraint on the outermost planet's mass. The system was later revisited by Lissauer et al. (2013, hereafter L13) using fourteen quarters of *Kepler* data. All three analyses estimate mean densities of $\leq 0.5\ \rho_E$ for all the planets in the system, implying a considerable gas envelope on even the smaller super-Earths. This result has implications for potential formation scenarios, with the viability of forming such low-density planets on short orbits in situ up for debate (e.g. Lopez et al., 2012; Chiang & Laughlin, 2013; Bodenheimer & Lissauer, 2014; Howe & Burrows, 2015).

Mean planet densities derived from transits and TTVs (or from transits and radial velocities) have a strong dependence on the assumed properties of the host star. Since the transit depth observationally constrains the ratio of planetary radius to stellar radius, the planet volume depends on the assumed stellar radius to the third power. The planet mass found from TTV inversion is correlated with the stellar mass. Host star characterization is therefore a critical part of measuring planet densities.

In past works, Kepler-11 has been characterized only through spectroscopic analysis of low to modest signal-to-noise data. Rowe et al. (2014), L11, and L13 all use moderate signal-to-noise ratio spectra (S/N$\leq$ 40) from Keck and apply the Spectroscopy Made Easy package (SME, Valenti & Piskunov, 1996) to perform synthetic spectral fitting. The resulting stellar atmospheric parameters, when compared with stellar evolution models, indicate that Kepler-11 is a slightly evolved solar analog with a density of $0.80 \pm 0.04\ \rho_\odot$ (L13).

Asteroseismic oscillation signals are not detected for Kepler-11, so the stellar density has not been independently determined (Campante et al., 2014). Previous analysis of the stellar composition is also minimal. Adibekyan et al. (2012a) perform an equivalent width (EW) analysis on one of these Keck spectra to derive abundances of three α-elements and find that Kepler-11 has moderately low abundances of Ca, Cr, and Ti; however, the line list employed is quite limited with ≤ 5 lines per element.

Kepler-11's well-characterized planetary system makes it a prime target for more detailed spectroscopic study. In this work, we present an analysis of a new, very high S/N spectrum. We use equivalent widths to measure the stellar properties and abundances of 22 elements at high precision.

The data are presented in Section 7.2. Derivation of the fundamental stellar properties from the spectrum is presented in Sections 7.3 and 7.4, and photospheric abundances are found in Section 7.5. We then present a new analysis of the *Kepler* lightcurve using a photodynamical model in Section 7.6. Finally, we compare the results from the spectroscopic and transit-based methods and discuss implications for the planetary system in Section 7.7.

Table 7.1 Summary of derived fundamental stellar properties.

Spectrum	$T_{\rm eff}$ (K)	σ_T (K)	$\log g$ (dex)	σ_{logg} (dex)	v_t (km s^{-1})	σ_{v_t} (km s^{-1})	[Fe/H] (dex)	$\sigma_{[Fe/H]}$ (dex)
Sun (Ceres) [a]	5777		4.44		0.97		0.0	
K11	5836	7	4.44	0.02	0.98	0.02	0.062	0.007
HD1178	5650	7	4.36	0.02	0.93	0.02	0.013	0.008
HD10145	5638	6	4.34	0.03	0.96	0.02	−0.032	0.009
HD16623	5791	26	4.37	0.07	0.97	0.06	−0.462	0.022
HD20329	5606	7	4.38	0.02	0.88	0.02	−0.094	0.008
HD21727	5610	9	4.38	0.03	0.96	0.02	−0.015	0.007
HD21774	5756	29	4.32	0.07	0.98	0.06	0.252	0.026
HD28474	5751	17	4.47	0.06	0.93	0.05	−0.614	0.014
HD176733	5609	9	4.41	0.03	0.87	0.02	−0.018	0.007
HD191069	5710	7	4.26	0.02	1.06	0.01	−0.044	0.005

---

[a] Used as reference star.

7.2 Data

Owing to its relative faintness (V = 14.2, L11), previous observations of Kepler-11 were at a signal-to-noise ratio insufficient for high-precision spectroscopic characterization. We dedicated nearly 8 hours of NASA-awarded Keck I time to obtaining a higher quality spectrum. Over the course of two consecutive nights (July 26-27 2015), we made 22 1200-s exposures of Kepler-11 for a co-added result of S/N$\simeq$260 per pixel in the continuum near 600 nm. For these observations, HIRES was used with the B2 slit and kv387 filter, yielding a resolution R$\simeq$67,000 and wavelength coverage between 390 and 830 nm.

We also observed the solar spectrum (via reflection from Ceres) and nine bright potential Kepler-11 twins with the same instrumental setup and similar S/N. The Kepler-11 twins were selected by imposing criteria of $5600 \leq T_{\rm eff} \leq 5750$ K and $4.2 \leq \log g \leq 4.4$ dex on databases of previously published stellar parameters (Adibekyan et al., 2012b; Bensby et al., 2014). Preference was given to stars likely to be thick-disk members with approximately solar metallicity. These criteria were set based on the original spectroscopic analysis of Kepler-11 by L11, who found $T_{\rm eff} = 5680 \pm 100$ K, $\log g = 4.3 \pm 0.2$ dex, [Fe/H]$= 0.0 \pm 0.1$ dex, and a significant chance of Kepler-11's being a thick disk member based on its kinematics.

The spectral extraction was performed by the Mauna Kea Echelle Extraction (MAKEE) pipeline.[2] All Kepler-11 spectra were then co-added using IRAF's *scombine*.[3] Continuum normalization was done by fitting low-order polynomial functions to each order, with care to use the same functional order for a given spectral order on every stellar spectrum to avoid bias in the subsequent differential analysis. Doppler corrections were applied using IRAF's *dopcor* task.

---

[2] `http://www.astro.caltech.edu/~tb/makee/`

[3] IRAF is distributed by the National Optical Astronomy Observatory, which is operated by the Association of Universities for Research in Astronomy (AURA) under cooperative agreement with the National Science Foundation.

7.3 Stellar Properties from Spectroscopic Analysis

The fundamental properties of Kepler-11 and its potential twins were derived from an equivalent width analysis. We manually measured 94 Fe I and 17 Fe II spectral lines using IRAF's *splot*. The line list used unblended and unsaturated iron lines adapted from previous works such as Ramírez et al. (2014b). Laboratory values for transition probability were adopted where available, but for this strictly differential analysis the values of log *gf* are largely irrelevant, since they cancel out for all lines in the linear region of the curve-of-growth. Equivalent widths were measured by carefully choosing local continua as described in Bedell et al. (2014) to maximize differential precision between the spectra. The full line list and measured equivalent widths are available in the online version of Bedell et al. (2017). Since our method depends on hand-measuring equivalent widths with the exact same choices made for target and reference spectra, we always use solar equivalent widths measured at the same time as the target stars. Since a few of the potential twin stars (HD10145, HD21727, and HD191069) were measured at a different time than the others, a second column of solar equivalent widths is given as a reference for those three stars only.

The stellar effective temperature T_{eff}, surface gravity $\log g$, metallicity [M/H], and microturbulence v_t were determined by imposing a set of requirements on the iron abundances derived by MOOG (Sneden, 1973). Namely, we required the [Fe/H] abundances from both ionization states to be equal, and any trends in iron abundance with the excitation potential or reduced equivalent width of the lines to be minimized. As the most readily observable abundant metal in the photosphere, we used iron abundance [Fe/H] as a direct proxy for metallicity [M/H]. It is important to note that we exclusively used the *differential* abundance measurements relative to the solar spectrum for this analysis. By directly comparing line-by-line differential abundances of spectrally similar stars, we minimize the influence of stellar model systematics on the final parameters and abundances (see e.g. Ramírez et al., 2014b).

Parameter solutions were found iteratively using the q^2 python package.[4] Uncertainties were determined by propagating scatter among the measured line abundances as described in Epstein et al. (2010) and Bensby et al. (2014).

The resulting stellar parameters for all observed stars are given in Table 7.1. The T_{eff} and $\log g$ for Kepler-11 are significantly higher than previously determined values. We find $T_{\text{eff}} = 5836 \pm 7$ K, $\log g = 4.44 \pm 0.02$ dex, and [Fe/H]$= 0.062 \pm 0.007$ dex, while L13, for example, find $T_{\text{eff}} = 5666 \pm 60$ K, $\log g = 4.28 \pm 0.07$ dex, and [Fe/H]$= 0.00 \pm 0.04$ dex. Potential sources of this tension include the substantially different S/N of spectra used and the difference in analysis technique. L13 and other previous analyses use SME, which fits synthetic spectra to the observations. Different choices of spectral analysis technique have been shown to vary the derived stellar parameters beyond their nominal error estimates, so this explanation cannot be ruled out (Hinkel et al., 2016). However, since our analysis is performed relative to the solar spectrum, our results are anchored to the accurate stellar parameters of the Sun. Furthermore, our method is strictly differential, based on line-by-line comparison of equivalent widths measured using spectra of the Sun and Kepler-11 gathered with the same instrumentation and in the same observing run. Thus, our approach minimizes possible systematic errors that could affect other analyses.

Our revised stellar parameters securely place Kepler-11 in the solar twin category. This can be seen even by eye: as depicted in Figure 7.1, at high S/N Kepler-11's spectrum is nearly identical to the solar spectrum and distinctly different from that of HD1178, the star from our sample whose fundamental parameters most closely match those found by L13. In particular, the solar-like $\log g$ for Kepler-11 implies that it is denser and less evolved than previously thought.

We used stellar evolutionary models to estimate the mass, radius, and age of Kepler-11. Yonsei-Yale isochrones were fit using q^2 (Demarque et al., 2004). We applied an [Fe/H] offset of 0.04 dex to align the isochrone grid with the solar values, as discussed in Meléndez et al.

---

[4] `http://github.com/astroChasqui/q2`

(2012). From this, we estimate a stellar mass $M_\star = 1.042 \pm 0.005 M_\odot$, radius $R_\star = 1.021 \pm 0.025 R_\odot$, and age 3.2 ± 0.9 Gyr (Figure 7.2). This gives a stellar density $\rho_\star = 1.38 \pm 0.10$ g cm^{-3}, or 0.98 ± 0.07 $\rho_\odot$.

Given the difficulty of inferring a stellar mass and radius to percent-level precision, it is worth looking deeper into the above-quoted estimates. As a solar twin, Kepler-11 is located close to the anchor point of solar-calibrated isochrone grids, so such high precision is not unreasonable. As one test, we applied Dartmouth isochrones using the *isochrones* python package (Dotter et al., 2008; Morton, 2015). The Dartmouth models give $M_\star = 1.036 \pm 0.006 M_\odot$, $R_\star = 1.015 \pm 0.022 R_\odot$, age 3.4 ± 0.8 Gyr, and density 0.99 ± 0.07 $\rho_\odot$, in excellent agreement with the Yonsei-Yale values. While systematic errors in mass and radius may be introduced from effects like differing helium abundance and/or age-dependent gravitational settling, the proximity of Kepler-11's stellar parameters, abundances, and age to the solar values should minimize these effects. Additionally, the Yonsei-Yale grid accounts for changes in helium abundances with a metallicity-dependent scaling factor.

7.4 Alternative Stellar Age Indicators

In addition to isochrones, we used several alternate methods to measure the age of Kepler-11 as an independent test of its evolutionary state. The results unanimously agree upon a sub-solar age for Kepler-11. Details of the methods used follow.

7.4.1 Stellar Rotation

The apparent rotation rate $v \sin i$ was measured using five saturated lines (Fe I 6027.050 Å, 6151.618 Å, 6165.360 Å, 6705.102 Å, and Ni I 6767.772 Å) from the Keck spectrum. The procedure used is described in depth in dos Santos et al. (2016), and is summarized here. We first measured the macroturbulence value $v_{\mathrm{macro},\odot}$ for each line in the solar reference spectrum using MOOG *synth* with $v \sin i_\odot$ fixed at 1.9 km s^{-1}. We then calculated v_{macro}

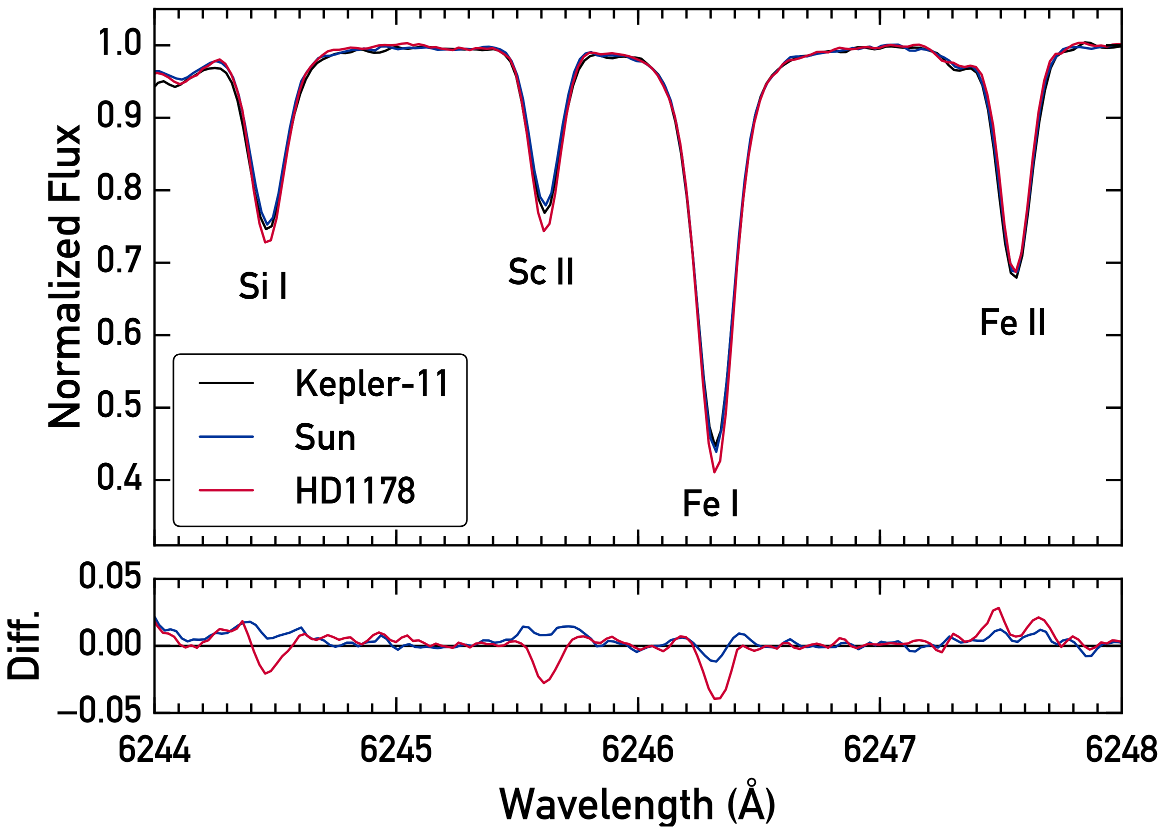

Figure 7.1 A small section of the Keck-HIRES spectra of the Sun (blue), Kepler-11 (black), and HD1178 (red), which has fundamental parameters similar to those given by Lissauer et al. (2013) for Kepler-11. Residuals for flux relative to the Kepler-11 spectrum are plotted in the lower panel.

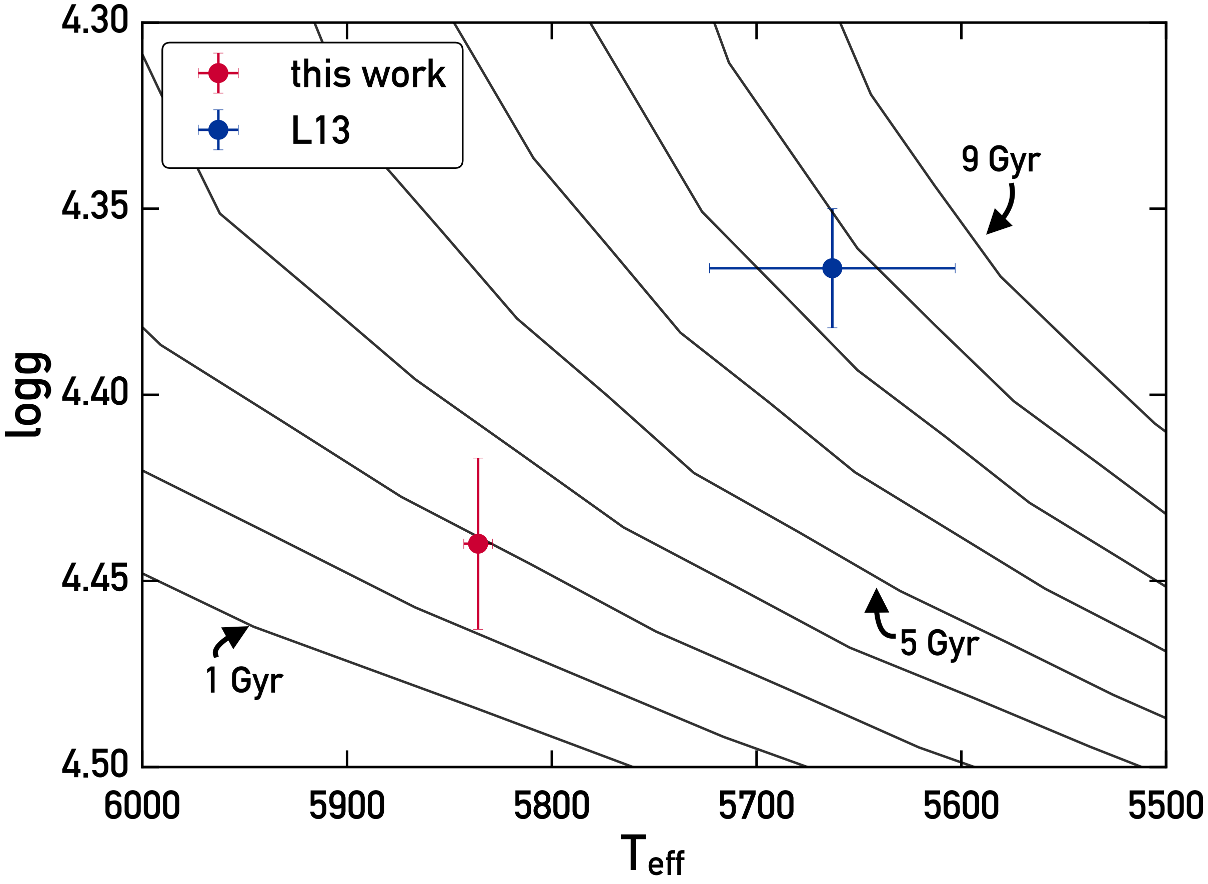

Figure 7.2 Measured stellar properties of Kepler-11 from this work and from L13 plotted with Yonsei-Yale isochrones at a metallicity of 0.06 dex.

for Kepler-11 using the measured solar values and an empirical relation given in Equation 1 of dos Santos et al. (2016) which calculates the expected $v_{\rm macro}$ difference from the Sun as a function of stellar $T_{\rm eff}$ and $\log g$. This relation was derived using 10 solar twins observed at very high resolution with HARPS, so we expect the $v_{\rm macro}$ relation to be accurate for the solar twin Kepler-11 as well. Finally, MOOG *synth* was used to find $v \sin i$ for each line in Kepler-11's spectrum with $v_{\rm macro}$ fixed to the calculated value.

The five lines give a consistent result of $v \sin i = 2.2 \pm 0.2$ km s^{-1}. Assuming alignment of the stellar spin axis with the orbital axis of its transiting planets, we can take $v \sin i$ as the true rotational velocity. This translates to an age of 3.4 Gyr using the law of Skumanich (1972) anchored by the Sun, or 3.0 Gyr from dos Santos et al. (2016)'s updated relation.

7.4.2 Lithium Abundance

The lithium abundance of Kepler-11 was measured by synthesizing the Li I 6707.8 Å line with MOOG *synth*. The line list was adopted from Meléndez et al. (2012) and includes blends of atomic and molecular lines. We find a lithium abundance of $A(\rm Li) = 1.28 \pm 0.07$, higher than the measured solar value of 1.03 ± 0.04 at the level of 3σ (Figure 7.3). After applying NLTE corrections, these values become $A(\rm Li) = 1.32 \pm 0.07$ for Kepler-11 and $A(\rm Li)_\odot = 1.07 \pm 0.04$ for the Sun (Lind et al., 2009).[5] Kepler-11's higher lithium abundance implies a sub-solar age, since lithium is depleted throughout a star's main-sequence lifetime (Duncan, 1981). Using the solar-twin-based lithium-age relation from Carlos et al. (2016) gives an age estimate of about 3.5 ± 1.0 Gyr for Kepler-11.

7.4.3 [Y/Mg] Abundance Ratio

Recent works by Nissen (2015) and Tucci Maia et al. (2016) have identified the ratio of yttrium to magnesium abundances as an excellent proxy for age in main-sequence Sun-like

---

[5] Data obtained from the INSPECT database, version 1.0 (`http://www.inspect-stars.com`)

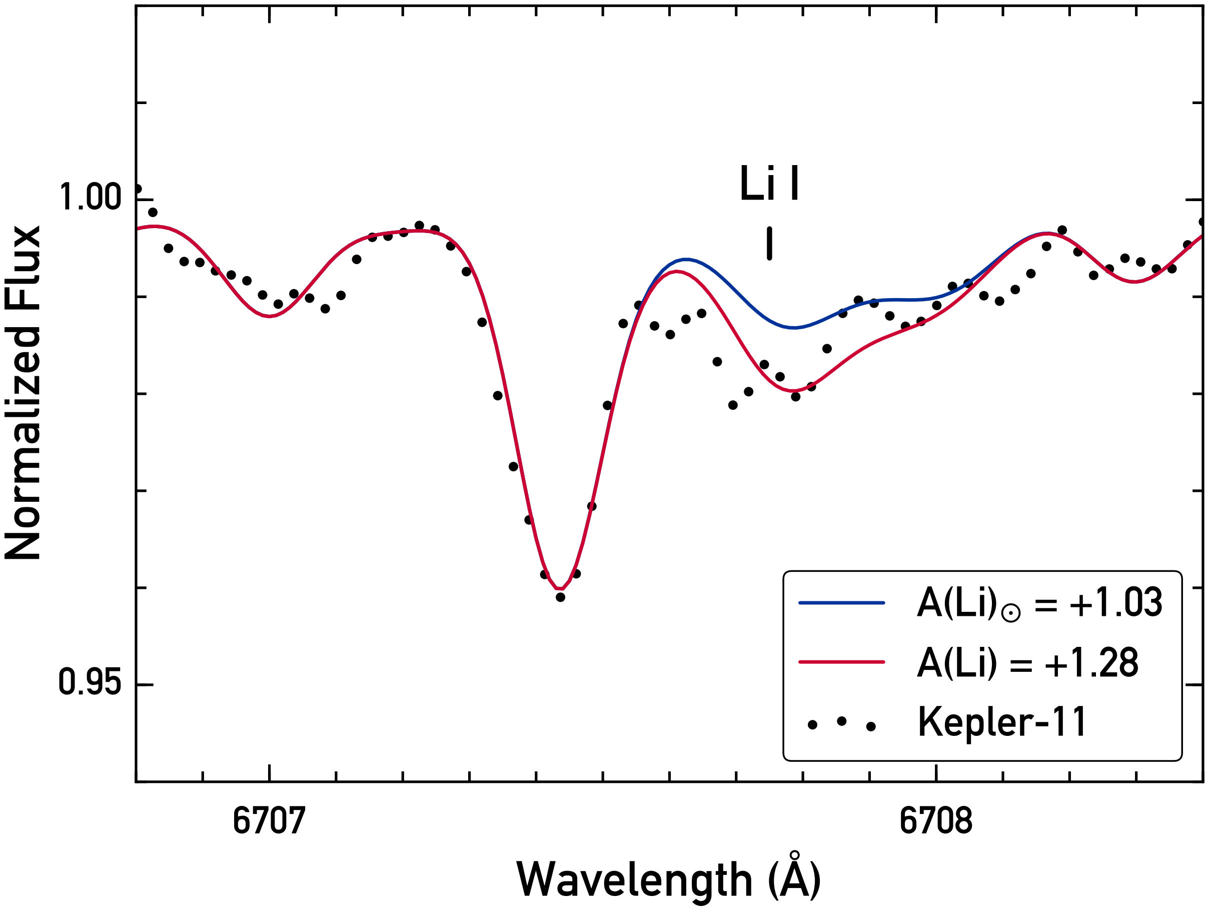

Figure 7.3 Observed spectrum of Kepler-11 around the Li I 6707.8 Å line. Synthetic fits for the best-fit Li abundance (red) and the solar Li abundance (blue) are overplotted.

stars. We measured these abundances as described in Section 7.5 and found a [Y/Mg] ratio of 0.04 ± 0.05 dex. Using the age relation from Tucci Maia et al. (2016), this gives an age of 4.0 ± 0.7 Gyr.

7.4.4 *Chromospheric Emission*

We measured the chromospheric emission level of Kepler-11 using the Ca II H line. Since our spectral coverage cut off around 390 nm at the blue end, it was not possible to obtain a measurement of the standard chromospheric activity index $\log(\mathrm{R}'_{\mathrm{HK}})$. Instead, we defined an alternative index H as the flux integrated from a 1.3 Å width triangular filter centered on the H line at 3968.47 Å, divided by the continuum integrated with a flat filter of 5 Å width around 3979.8 Å. This measurement of H was converted to the standard Mount Wilson S_{HK} using the following equation, which was derived from the literature values of ten Sun-like stars:

$$S_{HK} = 0.901H + 0.033 \tag{7.1}$$

We find an activity index $\log(\mathrm{R}'_{\mathrm{HK}})$ = -4.82. This is slightly higher than the maximum activity level of the solar cycle and suggests a sub-solar age (Skumanich, 1972). The activity-age relation for solar twins given in Freitas et al. (2016) yields an age estimate of 1.7 Gyr, although this is quite uncertain since we have measured the activity level at only one epoch and cannot average over the activity cycle.

7.5 Stellar Abundances

We measured photospheric abundances using the curve-of-growth technique for 20 other elements (excluding lithium, whose synthesis-based abundance determination is discussed in Section 7.4.2). As with the iron lines, all equivalent widths were measured by hand and line-by-line differential abundances determined with MOOG using q^2. The line list was adapted

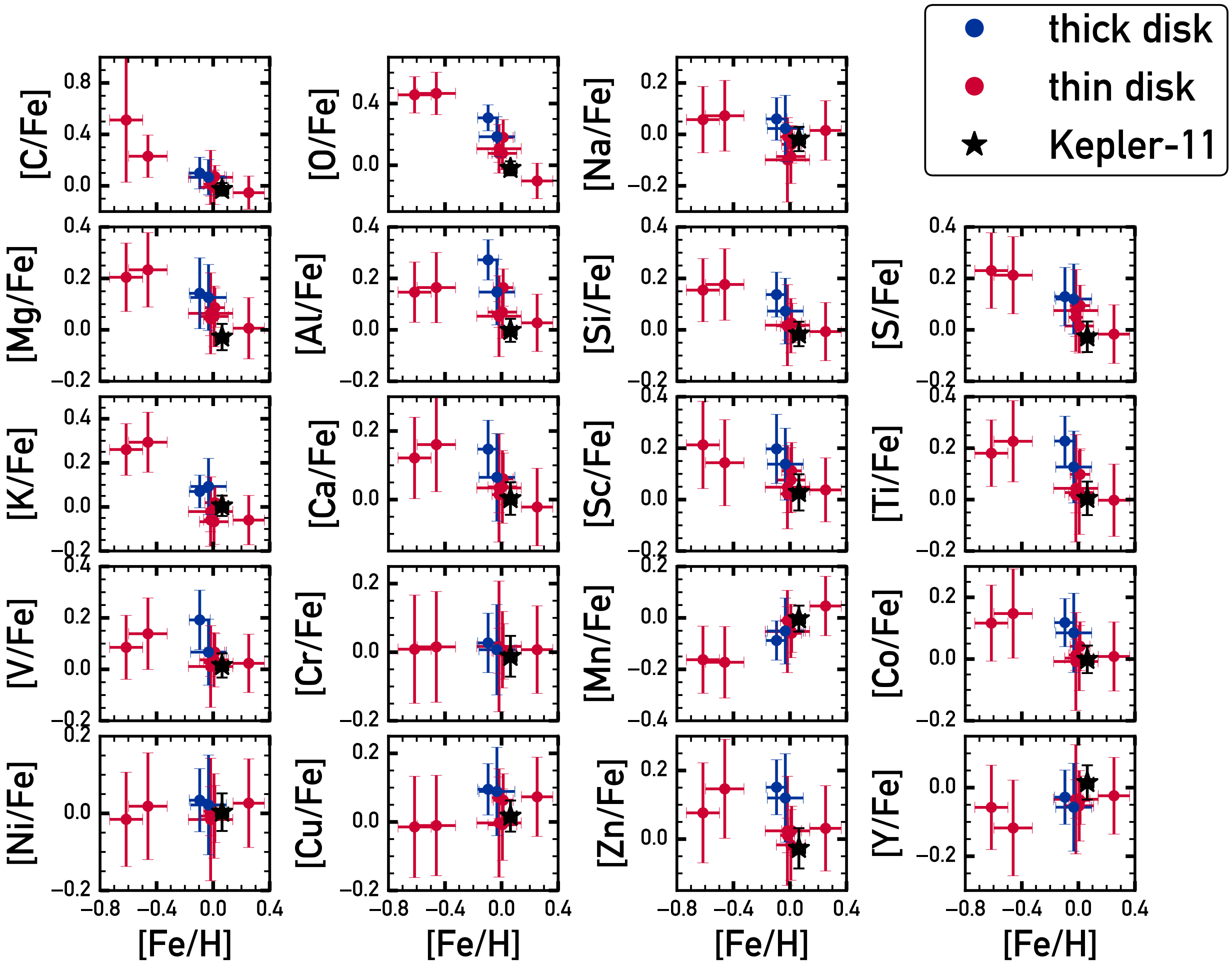

Figure 7.4 Measured abundances plotted as a function of metallicity for the full sample. Thin (red circle) and thick (blue circle) disk stars are categorized by their kinematic membership probabilities. Kepler-11 is represented as a black star.

from previous works including Bedell et al. (2014). For the element K, only one line was available, so it was measured multiple times and the deviation of the results was used as an error estimate; however, this uncertainty may be underestimated due to the line's location near a telluric-contaminated region. Hyperfine structure corrections were applied for Co I, Cu I, Mn I, V I, and Y II following Meléndez et al. (2012). Non-LTE corrections were applied for O I using grids from Amarsi et al. (2015). Carbon abundances were measured by a combination of C I and CH lines; we note that the abundances for the two species are in tension at the $\sim 2\sigma$ level for several of the stars in the sample, indicating that there may be some systematic effects at play. The measured equivalent widths and resulting abundances for all stars are available in the online tables associated with the original publication of this work (Bedell et al., 2017). The quoted abundance errors include both the intrinsic scatter of the lines and the uncertainty propagated from errors on the stellar parameters. For subsequent analysis, all measured states of a given element (e.g. CI and CH, TiI and TiII, etc.) were combined with a weighted average to yield the overall elemental abundance.

Since Kepler-11 was previously thought to be a potential thick-disk member based on its radial velocity (RV = -57.16 km s^{-1} in L11; we find -56.7 ± 0.7 km s^{-1}), several of the intended Kepler-11 twins were selected by thick-disk kinematics. As a result, we have both thin and thick disk stars in our sample. The detailed abundances of these groups can be quite different even within a small range of metallicities (see e.g. Liu et al., 2016). In Figure 7.4, we plot the abundances for thick- and thin-disk stars as a function of their measured metallicity. Disk membership was assigned based on UVW kinematics using the procedure specified in Reddy et al. (2006).

Kepler-11 follows the abundance trends of the other thin-disk stars well and does not display a notable α-element enrichment. In fact, we find that despite its low radial velocity, its UVW kinematics are consistent with it being a thin disk member. Using the proper motions from UCAC3 (Zacharias et al., 2010), our measured RV, and the isochrone-based absolute magnitude estimate ($M_V = 4.7$ or a parallax of 1.3 mas), we find (U, V, W) = (8.1,

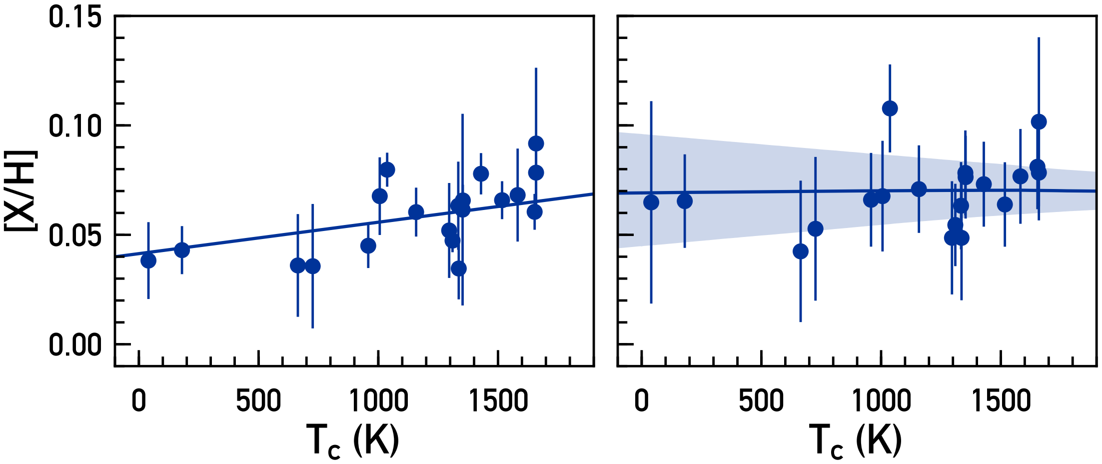

Figure 7.5 Abundances of Kepler-11 relative to the Sun as a function of the condensation temperature of the element within the protoplanetary disk. Left panel shows the abundances and best-fit linear trend before applying galactic chemical evolution (GCE) corrections, with error bars from the line-to-line scatter and propagated uncertainty in the stellar parameters. In the right panel, the data have been GCE-corrected following Spina et al. (2016a), assuming a stellar age of 3.2 Gyr, with error bars that additionally include propagated uncertainties in the stellar age and GCE correction factors. The shaded region represents the 1σ uncertainty interval on the linear fit to [X/H] vs T_C from the bootstrap simulation described in the text.

-43.7, -6.3) km s^{-1}. This translates to a 98% probability of Kepler-11 belonging to the thin disk population.

Kepler-11's status as a thin-disk solar twin enables direct comparison of its abundance pattern to that of the Sun and other known solar twins. Of particular interest is the question of trends in elemental abundances with condensation temperature (T_C). As shown by Meléndez et al. (2009), the solar abundance pattern is unusual in its depletion of refractory elements relative to volatiles. This depletion has been interpreted as "missing" rocky material that is locked up in the Solar System planets (Chambers, 2010). Building up the number of stars with precisely characterized abundance patterns and planetary systems can help to test this possibility.

We applied corrections for the effects of galactic chemical evolution (GCE), which can change the abundance patterns and T_C trends of stars at varying ages (Nissen, 2015; Spina et al., 2016b). We corrected each abundance [X/H] using the linear relationships found by

Spina et al. (2016a), who fit [X/H] as a function of stellar age for a sample of solar twins. We then used the corrected abundances and $T_{\rm C}$ values from Table 8 of Lodders (2003) to search for a trend.

The uncertainty on the trend of [X/H] with $T_{\rm C}$ was propagated using a bootstrap Monte Carlo method to account for multiple potential sources of error. Each abundance is uncertain due to the intrinsic scatter of abundances derived from different lines. This uncertainty increases when the GCE correction is applied, since the correction coefficients carry some degree of random error. Additionally, the slope of the $T_{\rm C}$ trend can be altered by errors on the fundamental stellar parameters used (as seen in Teske et al., 2015) and by the uncertainty on stellar age in the GCE correction. We account for all of these effects by running 10,000 bootstrap trials where the stellar parameters are resampled from their posterior distributions; the resulting abundances are randomized by drawing samples from the multiple measured lines; the age is determined based on the resampled stellar parameters; and the GCE correction is applied using coefficients that have been randomly sampled from the (assumed Gaussian) uncertainties given in Spina et al. (2016a). The resulting distribution of $T_{\rm C}$ trend fits gives a slope of [X/H] vs $T_{\rm C}$ of $(-0.6^{+9.3}_{-11.0}) \times 10^{-6}$ dex K^{-1} (Figure 7.5). In short, the trend of Kepler-11's abundances with $T_{\rm C}$ is indistinguishable from the solar pattern, albeit with a large degree of uncertainty due to the many sources of error which come into play when considering GCE effects.

An additional source of systematic error in the $T_{\rm C}$ trend is in the NLTE correction adopted for oxygen. As one of the few extremely volatile elements in our analysis ($T_{\rm C} = 180$ K), oxygen has a strong influence on the $T_{\rm C}$ slope. The 777 nm triplet used for oxygen abundances in this analysis is also quite sensitive to NLTE effects. We carried out the above analysis using the NLTE corrections of Ramírez et al. (2007). This yielded an oxygen abundance $[\mathrm{O/H}] = 0.058 \pm 0.012$ (pre-GCE correction) and a $T_{\rm C}$ slope of $(-4.6^{+7.9}_{-8.7}) \times 10^{-6}$ dex K^{-1}, still within the 1σ uncertainty.

7.6 Stellar Properties from Photodynamic Transit Analysis

7.6.1 Analysis

In order to reassess the stellar density constraint based on the transit data, we performed a photodynamical fit to the full *Kepler* short cadence (58.8 second exposure) data set. The model integrates the 7-body Newtonian equations of motions for the central star and six planets, including the light–travel–time effect. When the planets pass between the star and the line of sight, a synthetic light curve is generated (Pál, 2012), which can then be compared to the data. This approach therefore takes into account all transit-timing variations, simultaneously constraining planet masses, eccentricities, and radii. To prepare the data for fitting, we detrended the data with a cubic polynomial with a 2880 minute (2 day) width every 100 points, and interpolated for points between. We divided the flux by this fit as a baseline to generate our data set of 1746779 points. We additionally multiplied the uncertainties given by *Kepler* by a factor of 1.115318 so that the reduced χ^2 of a fiducial model was 1.0. This broadens our posteriors and helps take into account unmodeled noise in the data. To simultaneously generate the posteriors on all of our model parameters, we ran differential evolution Markov chain Monte Carlo (DEMCMC, Ter Braak, 2006) fits with planetary parameters $\{P, T_0, e^{1/2}\cos(\omega), e^{1/2}\sin(\omega), i, \Omega, R_\mathrm{p}/R_\star, M_\mathrm{p}/M_\star\}$ for all planets, where P is the period, T_0 is the mid-transit time, e is eccentricity, ω is the argument of periapse, i is inclination, Ω is nodal angle, and R and M are radius and mass, respectively (with subscripts $\mathrm{p} = \mathrm{b, c, d, e, f, g}$ for the planets and $\star$ for the star). The star has five additional parameters: $\{M_\star, R_\star, c_1, c_2, dilute\}$, where $\{c_i\}$ are the two quadratic limb-darkening coefficients and *dilute* is the amount of dilution from other nearby sources. We used eccentricity vector components scaling as $e^{1/2}$ so that we get flat priors in total e, and fixed the values of $dilute = 0$ since there is no evidence of other nearby stars diluting the lightcurve. We also fixed the value of $M_\star$, as transits alone generally only give information about the density of the star, rather than $M_\star$ and $R_\star$ individually. We fixed $\Omega = 0$ for all planets because the data are not precise enough to constrain these values (Migaszewski et al., 2012). Additionally, it is extremely unlikely that there are large mutual inclinations among the planets given that we see six transiting planets (L11, Figure 4), five of which are dynamically packed and thus have no misaligned non-transiting planets between them (L11). We used flat priors for all other parameters.

We ran two DEMCMCs to model the data. One had no constraints on the stellar radius, i.e., allowed the transits themselves to completely determine the stellar density, which we will label $\mathcal{NSI}$ for "No Spectral Information." The second DEMCMC was run with the stellar mass and radius fixed at the spectroscopically measured values in this study, $M_\star = 1.04 M_\odot$ and $R_\star = 1.02 M_\odot$, which we will label $\mathcal{FSP}$ for "Fixed Stellar Parameters." The $\mathcal{NSI}$ run produces a lower density star $\rho_\star = 1.19^{+0.04}_{-0.11}$ g cm^{-3} than the fixed value of $\rho_\star = 1.38$ g cm^{-3} in $\mathcal{FSP}$. This indicates that the transit data alone are discrepant with the spectroscopically measured stellar density. Table 7.2 shows the mass, radius, and density results for all bodies for both DEMCMC runs. We note that the densities of planets with no spectral information, $\mathcal{NSI}$, are slightly higher than reported in L13 because that study includes the lower spectroscopically measured stellar density in their final best fits.

The best fit solution from $\mathcal{NSI}$ run has a lower χ^2 value by more than 40 compared to the best-fit $\mathcal{FSP}$ run. Thus we see that fixing the stellar parameters at their spectroscopically measured values causes the fit to the *Kepler* data to become significantly worse; the p-value for such an increase in χ^2 is on order 10^{-9}. This confirms the existence of tension between the transit measured stellar density and the spectroscopically measured one.

7.6.2 Physical Interpretation

Transit measurements of stellar (and thus planet) densities rely on the the transit of the planet probing the width of the star. For a given stellar mass, once the period of a planet is known from successive transits its orbital velocity (v_{orb}) can be determined. The physical distance a planet traverses during the duration of a transit (T_{dur}) is to a very good approximation $T_{\mathrm{dur}}/v_{\mathrm{orb}}$. There are two main degeneracies between the stellar radius and and the measured duration: (1) eccentricity of the planets orbit and (2) impact parameter of the transit.

Eccentricity changes v_{orb} as a function of orbital phase following Kepler's Second Law. However the observed transit timing variations provide information on the level of eccentricity of the interacting planets, and they are all found to be very small (< 0.05), only negligibly affecting the measured stellar radius. Using standard orbital mechanics, it may be seen that $\rho_\star \propto R_\star^{-3} \propto v_{\mathrm{orb}}^{-1} = (GM_\star(\frac{2}{r} - \frac{1}{a}))^{-1/2} \propto 1 - e\sin\omega + \mathcal{O}(e^2)$, where G is the Newtonian gravitational constant, a is the planet's semi-major axis, and r is the instantaneous star-planet distance. Thus a change in $\rho_\star$ by the $\sim$20% required to reconcile the spectroscopic and TTV measurements would require a uniform increase in $e\sin\omega$ across all planets of order 0.06, well beyond that allowed by the TTVs. Our fits marginalize over the range of possible eccentricities by including the eccentricity vectors as free parameters when fitting for stellar and planetary densities. In the $\mathcal{FSP}$ DEMCMC, the planets' eccentricities do increase substantially, but the chains are unable to find a TTV solution nearly as good as for the low eccentricity case, as discussed above.

The second major degeneracy (impact parameter, b) is determined by the shape of the transits. The slope of the ingress/egress indicates the curvature of the star during ingress/egress and therefore the radius of the star may be computed via $R_\star = (a/b)\cos i$, where a is the semi-major axis and i is the inclination. We also marginalize over these parameters, but note that the impact parameter is a positive definite quantity, and is consistent with 0 for planets d and g. Without perfectly measured transit shapes, there is some freedom to increase impact parameter away from 0 simultaneously with an increase in stellar radius so that the transit chord and thus T_{dur} is constant. If the stellar radius is decreased while the impact parameter is at or near 0, then there is no such compensatory degenerate parameter to change that would increase the transit chord, and the well-measured value of

Table 7.2 Star and Planet Properties

	$\mathcal{NSI}$			$\mathcal{FSP}$		
Body	Mass (M_E)	Radius (R_E)	Density (g cm^{-3})	Mass (M_E)	Radius (R_E)	Density (g cm^{-3})
Kepler-11 b	$2.78^{+0.64}_{-0.66}$	$1.83^{+0.07}_{-0.04}$	$2.45^{+0.63}_{-0.62}$	$2.83^{+0.62}_{-0.66}$	$1.74^{+0.02}_{-0.02}$	$2.96^{+0.66}_{-0.70}$
Kepler-11 c	$5.00^{+1.30}_{-1.35}$	$2.89^{+0.12}_{-0.04}$	$1.11^{+0.32}_{-0.32}$	$5.05^{+1.19}_{-1.37}$	$2.75^{+0.02}_{-0.02}$	$1.34^{+0.32}_{-0.36}$
Kepler-11 d	$8.13^{+0.67}_{-0.66}$	$3.21^{+0.12}_{-0.04}$	$1.33^{+0.14}_{-0.15}$	$7.52^{+0.68}_{-0.68}$	$3.06^{+0.02}_{-0.02}$	$1.45^{+0.13}_{-0.13}$
Kepler-11 e	$9.48^{+0.86}_{-0.88}$	$4.26^{+0.16}_{-0.07}$	$0.66^{+0.08}_{-0.09}$	$8.37^{+1.01}_{-1.04}$	$4.03^{+0.02}_{-0.03}$	$0.71^{+0.09}_{-0.09}$
Kepler-11 f	$2.53^{+0.49}_{-0.45}$	$2.54^{+0.10}_{-0.04}$	$0.83^{+0.18}_{-0.16}$	$1.59^{+0.58}_{-0.54}$	$2.40^{+0.03}_{-0.03}$	$0.63^{+0.23}_{-0.21}$
Kepler-11 g	< 27	$3.33^{+0.26}_{-0.09}$	< 4	< 29	$3.16^{+0.03}_{-0.03}$	< 5
Kepler-11	1.04 $M_\odot$ (fixed)	$1.07^{+0.04}_{-0.01}$ $R_\odot$	$1.19^{+0.04}_{-0.11}$	1.04 $M_\odot$ (fixed)	1.02 $R_\odot$ (fixed)	1.38 (fixed)

Note. — Medians and 1-σ uncertainties from the DEMCMC runs as described in § 7.6

T_{dur} no longer fits the model. This results in the asymmetric photodynamically measured stellar density as shown in Fig. 7.6.

We also consider the effects of potential star spot crossing changing the apparent TTVs or transit durations. If star spots variations were contributing significantly to the fits, we would expect to see a greater reduced χ^2 in transit compared to out of transit, as our transit model would not properly fit the planets' transits over star spots or faculae. This effect is not observed, strengthening our confidence in the sufficiency of our model.

7.7 Discussion

7.7.1 Discrepancies in Stellar Densities

The stellar densities found through spectroscopic characterization (1.38 ± 0.10 g cm^{-3}) and photodynamical modeling ($1.191^{+0.043}_{-0.11}$ g cm^{-3}) are inconsistent at the level of $\sim 2\sigma$ (Figure 7.6). The uncertainties on the fundamental stellar parameters would need to have been underestimated by at least a factor of 4 to allow 1-σ agreement with the lightcurve-based stellar density measurement, which we regard as unlikely from extensive tests on our spectroscopic methods (Bedell et al., 2014; Ramírez et al., 2014b). While stellar densities from fundamental parameters can be strongly dependent on imperfect stellar isochrone models, we note that in this case Kepler-11's extreme similarity to the Sun places it near the anchor

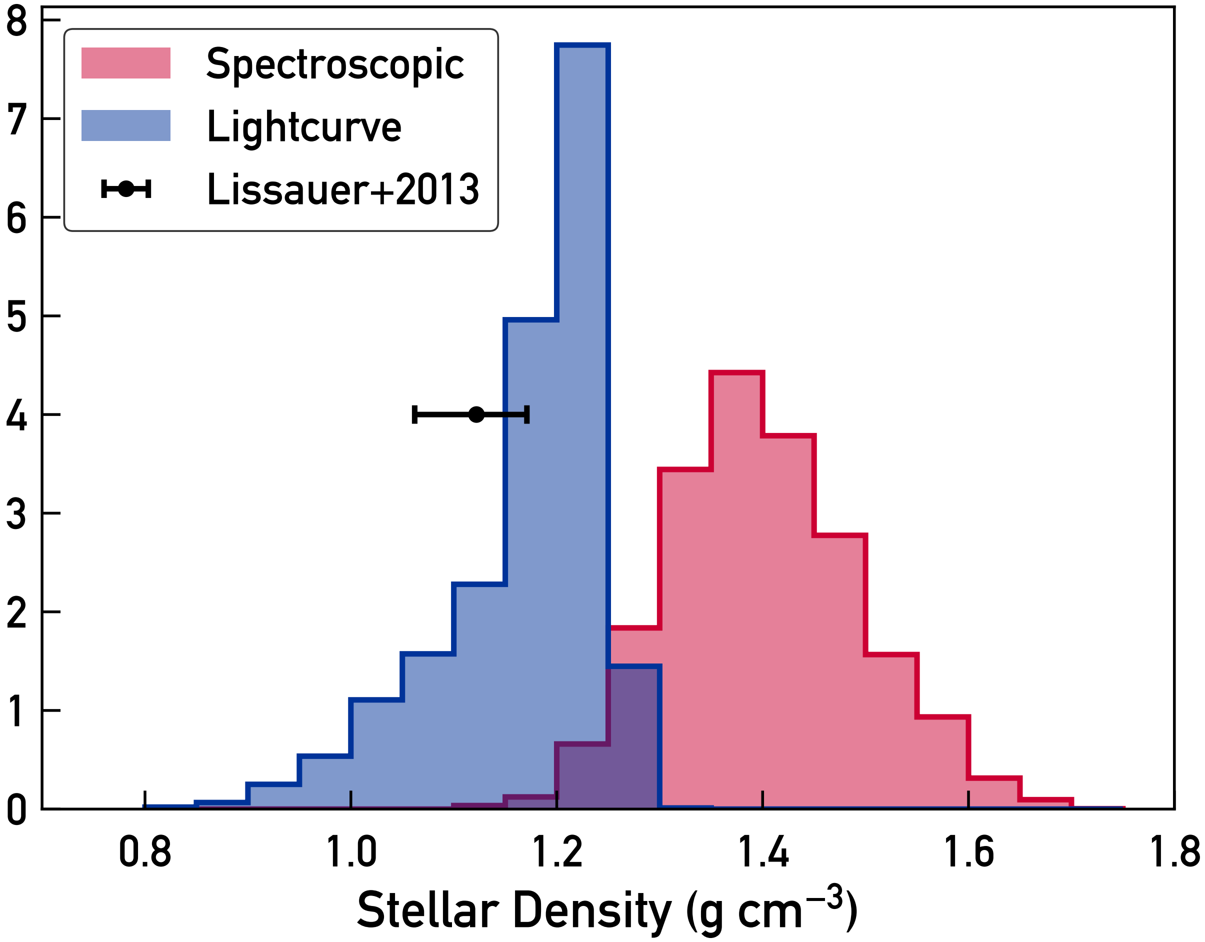

Figure 7.6 Posterior distributions for the stellar density from isochrone fits to the spectroscopic parameters (red) and from photodynamical modeling of the lightcurve (blue). The TTV-based stellar density from L13 is also plotted with one-sigma errors for comparison (black).

point of most models, increasing the accuracy of isochronal analysis. Moreover, multiple independent age determination methods support the result of a young, non-evolved age and therefore a solar-like density for Kepler-11.

An alternative hypothesis is that some bias in the transit analysis has resulted in an erroneously low inferred stellar density. As described by Kipping (2014), multiple effects can bias the density measured by transits, including stellar activity, blended background sources, and non-zero planet eccentricities. Bias due to an underestimated planet eccentricity is not a likely explanation in this case, since all five planets give a consistent stellar density. Also, the photodynamical modeling used in this analysis should be robust to the effects of transit timing or duration variations on the measured stellar density. This leaves two potentially viable explanations from Kipping (2014) for the density discrepancy: stellar activity (the "photospot" effect) or a background source (the "photoblend" effect).

Starspots effectively reduce the observed stellar flux, artificially raising stellar density inferred from the transit depth, which is the opposite of the effect we seek to explain. However, as a ∼3-4 Gyr Sun-like star, Kepler-11's activity may manifest mostly in the form of plages (Radick et al., 1998). Unocculted plages could potentially lower the observed stellar density by inflating the measured radii (Oshagh et al., 2014). Given the observed behavior of other main-sequence solar analogs and the lack of rotational modulation in the *Kepler* lightcurve, the filling factor for spots or plages on Kepler-11's surface should be of order a few percent at most (Meunier et al., 2010). This would yield a similarly small percent-level change in the observed stellar density (Kipping, 2014). Furthermore, the active region configuration would need to be relatively stable throughout *Kepler*'s four years of observations, which is unlikely at the high level of activity needed to have a large plage filling factor.

The final effect is blending of unresolved background sources, which can cause stellar density to be underestimated. Recently Wang et al. (2015) found two visual companions to Kepler-11 at separations of 1.36" and 4.9" using AO imaging. With brightness differences of

$\Delta K = 4.4$ mag and 4.7 mag respectively, these companions should contribute approximately 3% of the total flux in the Kepler bandpass. Using Equation 9 of Kipping (2014), this implies that the observed stellar density from transits should be ~99% of the true density. The known companions are therefore insufficient to explain the magnitude of the density discrepancy.

We are left with no obvious culprit for the discrepancy between the stellar densities measured from spectroscopic characterization and lightcurve modeling. Similar testing for other systems with measured TTVs is an important next step in determining whether this is a one-off event due to, e.g. underestimated uncertainties of stellar properties or unexpected stellar activity in the lightcurve, or if it is a systematic difference between these independent methods of analysis. If this is a systematic effect, it may be linked to the mass underestimation problem in TTV measurements relative to RVs found by Weiss & Marcy (2014).

7.7.2 Implications for the Planets

The adopted mass and radius of Kepler-11 has considerable repercussions for its planetary system. We can approximate the planet mass derived from TTVs as a linear function of the assumed stellar mass. The planet radius also has a linear dependence on stellar radius, since only the relative surface areas of planet and star can be measured by the transit depth. As shown in Table 7.2, fixing the stellar parameters at the spectroscopic values results in substantial changes in the planet properties which do not always follow the expected linear behavior. Because the $\mathcal{FSP}$ run did not yield a well-fitting result, as discussed in Section 7.6, we do not recommend adopting these values for the planet parameters. Instead, we use the well-fitting $\mathcal{NSI}$ results and scale the planet radii to the correct stellar values by multiplying by 0.95.

Compared to previously published planet parameters from L13, our newly derived values raise the planet masses and lower the planet radii substantially, resulting in an average bulk density increase of nearly 50%. The results are shown in Figure 7.7.

These parameter changes are in part a result of the new stellar mass and radius, which increased the density of the star (and thereby the inferred density of its planets) by 25%. The remainder of the change in planet density and in particular the tightening of the constraints on the planet masses arises from the method of TTV fitting. L13 adopt very conservative error bars which stretch across the 1-σ region of the results obtained by three independent transit time measurements. Our analysis, while less conservative, is fully self-consistent and makes use of all the available *Kepler* data through a full photodynamic process. Because we fit the entire lightcurve simultaneously, our model marginalizes over any uncertainties in the transit shapes and durations, which increases our confidence in the error estimates produced. Interestingly, of the three analyses presented in L13, our results are matched most closely by the analysis which uses no a priori assumption on the transit shape and applies minimal outlier rejection to the lightcurve, much like the choices made in our own modeling.

Our analysis most substantially raises the mean densities of the two innermost planets, Kepler-11 b and c, which undergo changes of 60% and 95% respectively. These increased densities, which imply a lower gas mass fraction in the planets' compositions, could make in-situ formation an increasingly viable explanation (see e.g. Lee et al., 2014).

7.7.3 Stellar Composition & Planets

While Kepler-11 is slightly more metal-rich than the Sun, its relative elemental abundances have a similar trend with T_{C} to the solar abundance pattern. Under the Meléndez et al. (2009) hypothesis that the Sun's photospheric composition reflects its planet-forming history, we could interpret Kepler-11's abundance pattern as a signature of the formation of rocky planets. Such a chemical signature of terrestrial planet formation has also been revealed in Kepler-10 host star, showing the depletion of refractory materials when compared to its stellar twins (Liu et al., 2016). It is, however, somewhat dangerous to draw conclusions about the abundance pattern of an individual system, as many other factors can affect stellar abundances at the few-percent level, including galactic chemical evolution and circumstellar disk physics (Gaidos, 2015).

The relatively large uncertainty on the condensation temperature trend underscores the importance of galactic chemical evolution effects in particular. Although we have achieved very high-precision stellar abundance measurements, more work remains to be done on disentangling potential planet formation signatures from stellar age-dependent effects. For an individual system, even a solar twin with an age within a couple Gyr of the Sun, the uncertain effects of GCE make it extremely challenging to draw conclusions about the significance of the stellar abundance pattern in the context of planet formation. Fortunately, large-scale surveys like APOGEE and GAIA-ESO will provide the large sample sizes needed to refine abundance-age relations.

Regardless, it is surprising that a star that is nearly indistinguishable from the Sun even with our most advanced characterization methods is orbited by a planetary system that is so different from our own. This result continues the theme of exoplanet discoveries pointing towards a much larger variety of outcomes from the planet formation and evolution processes than was predicted even just a few years ago.

7.8 Conclusion

Using an extremely high-quality spectrum of the multi-planet host star Kepler-11, we have measured the stellar fundamental parameters and abundances to percent-level precision. We have also used a photodynamical model to fit the full *Kepler* lightcurve. Our planet orbital parameters agree with past publications. However, we find that the host star is younger than previously thought by a factor of ∼3, with a higher $T_{\rm eff}$, $\log g$, and metallicity. Based on spectroscopic results, Kepler-11 and its planets are 20-95% denser than previously reported. These results stand in tension with the lightcurve results.

The five inner planets of the Kepler-11 system are key members of the exoplanet mass-radius diagram as examples of the surprisingly low densities found in some planetary systems. The substantial revision of their properties reported here underscores the importance of

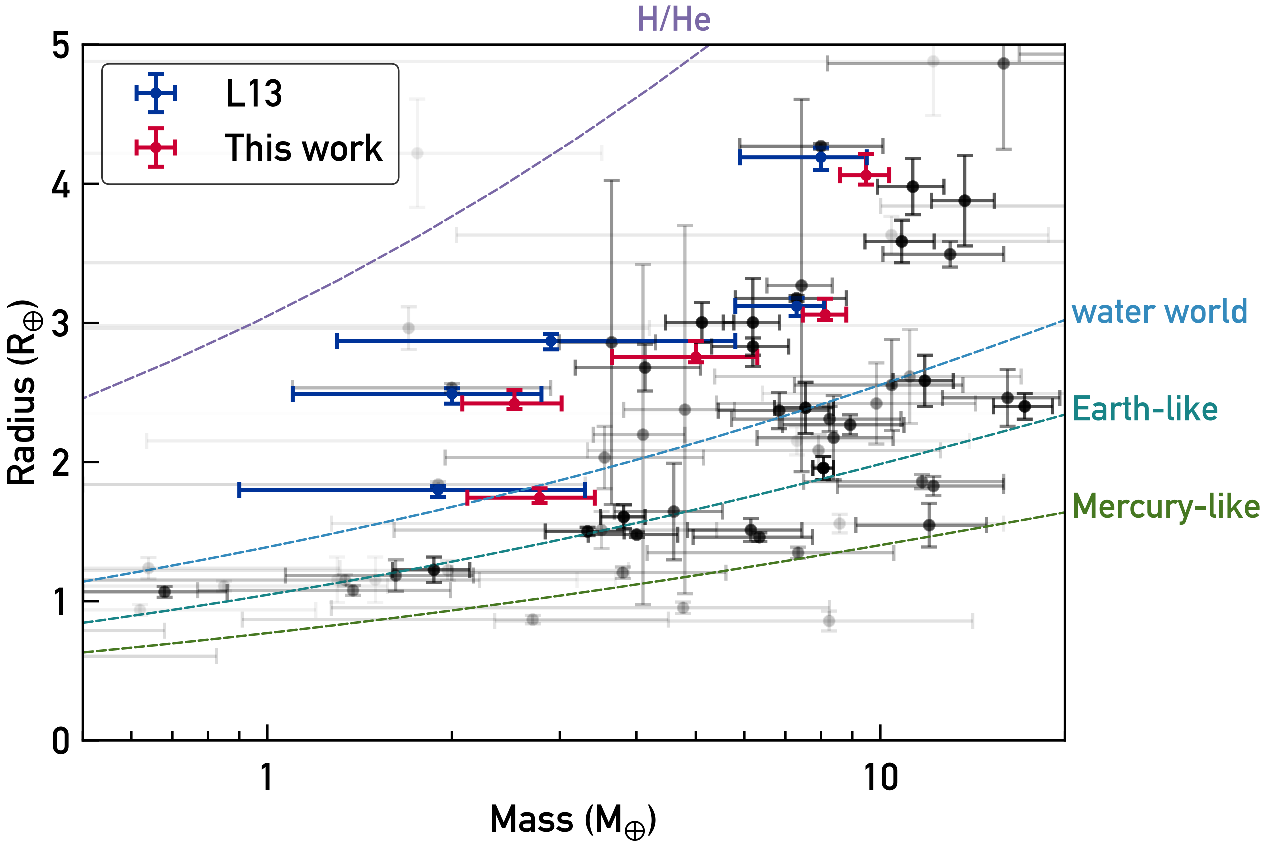

Figure 7.7 Exoplanets with measured masses and radii. Transparencies of the black points scale with the relative error on planet parameters. Kepler-11 a-e are plotted in blue (using the L13 values) and red (using the spectroscopically-adjusted TTV results derived by us, as described in Section 7.7.2). Dashed lines show models of different compositions from Seager et al. (2007).

detailed host star follow-up. As the community looks to exponentially increase the number of exoplanets with measured bulk densities through TESS and beyond, it is critical to prioritize securing high-quality spectra of the host stars to enable the determination of precise host star properties.

CHAPTER 8

CONCLUDING REMARKS

This thesis has demonstrated the power of twin-star spectroscopy in achieving detailed abundance measurements, and the promise of these abundances to reveal new information about planet properties. Much remains to be done, but the future looks bright for this work thanks to large surveys like *Gaia* and *TESS*. In the future, we look forward to major progress on two fronts: a greatly expanded sample size for more robust statistics, and the extension of planet detection sensitivity to encompass Earth-like worlds. These improvements will enable us to characterize the connection between even the smallest terrestrial planets and their host stars.

In this work, we have uncovered hints of intriguing planetary systems around Sun-like stars and investigated potential connections between exoplanets and their host stars. Most importantly, we have achieved extraordinarily precise constraints on the compositions of solar twin stars. These results place the Sun in context among its peers, and when combined with knowledge of stellar ages they reveal galactic chemical evolution patterns in unprecedented detail.

Such precise abundance measurements are not necessarily limited to solar twin stars. In principle the strictly differential equivalent width technique should work among groups of twin stars of any spectral type, with the caveat that the abundances achieved will be precise within the twin group but not necessarily accurate relative to stars of other spectral types. Indeed, this method has been used to achieve percent-level abundance measurements for small samples of twin stars in other regions of FGK stellar parameter space (e.g. Ramírez et al., 2014a; Teske et al., 2016a,b). Since the sample of bright nearby solar twins is intrinsically limited, an expansion of this work to similar surveys for other twin-star samples may be the best way forward. Independent samples of twins across the H-R diagram will validate and enhance the characterization of GCE and T_C trends with age and other stellar properties including planet host status.

Looking forward, several near-future surveys will enhance our ability to discover and characterize bright, spectroscopy-friendly twin stars. Chief among these in sample size is *Gaia*, which will measure parallaxes at precisions of a few microarcseconds for every bright star ($G < 20$) in the sky (Gaia Collaboration et al., 2016b). Smaller sample sizes but more well-characterized spectral typing will come from ground-based spectroscopic surveys like Gaia-ESO, RAVE, GALAH, and Funnel-Web (Gilmore et al., 2012; Steinmetz et al., 2006; De Silva et al., 2015; Lawson et al., 2016). The spectra taken by these surveys will generally be of insufficient quality for very precise abundance measurements, but the surveys themselves will be invaluable for identifying twin-star samples to follow up.

High-resolution, high-signal-to-noise spectroscopy of all of these twin stars will not be trivial to obtain; even for very bright stars with short integration times, telescope overheads add up quickly. Our work, however, has showcased an often-overlooked treasure trove of high-quality archival spectra: radial velocity surveys. The public archive of HARPS data contains excellent spectra of thousands of stars which can be co-added to achieve SNR on orders of hundreds to thousands. As shown in Figure 8.1, a preponderance of FGK dwarfs already exists among the overlap between the Tycho-Gaia sample and the HARPS archive. These stars carry the additional benefit of time-series RV information to place limits on their binary status, activity levels, and planetary systems.

In addition to the constraints from spectra, present and future photometric surveys will supply even more useful information about stars in the solar neighborhood. *K2* and *TESS* can uncover short-period planets and rotation signatures. The polar regions of *TESS*'s coverage will be especially valuable, since the year-long coverage will enable detection of longer-period signals including rotation periods of solar-age and older stars. *TESS* will also observe asteroseismic oscillations in a sub-sample of the brightest stars (Campante et al., 2016). In addition to their nominal missions of planet-hunting, then, *K2* and *TESS* can provide invaluable data on stellar properties through gyrochronology and asteroseismology.

Clearly we can look forward to obtaining a great deal of information about large sam-

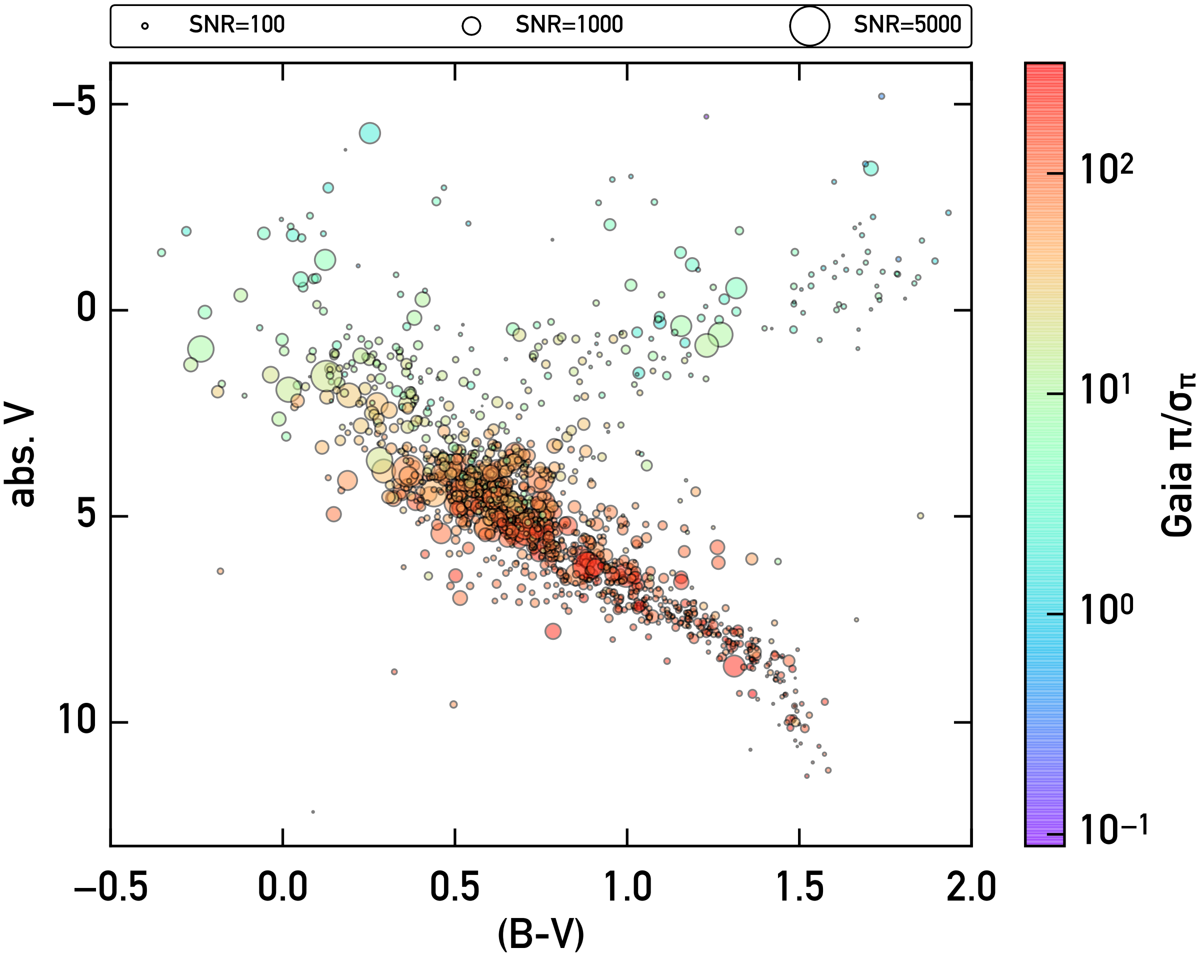

Figure 8.1 Stars from the Tycho-Gaia sample with HARPS archival spectra. Absolute magnitudes and colors come from *Gaia* DR1 (Gaia Collaboration et al., 2016a; van Leeuwen et al., 2017). Symbol sizes scale logarithmically with the expected SNR after all public HARPS spectra have been co-added. Color scales with the SNR of the *Gaia* DR1 parallax.

ples of bright stars in the next few years. What about making the link between stellar properties and planet formation? One of the chief limitations to this work is the difficulty of detecting terrestrial planets. While *Gaia*'s astrometry and various ground-based direct imaging programs are sensitive to massive planets on long-period orbits, and *TESS* will survey short-period transiting planets, radial velocities remain the most promising current method for the discovery of small planets on Earth-like orbits. It will require concentrated efforts by the community to obtain the required amounts of observations and develop the analysis techniques to extract planet signals from stellar astrophysical phenomena. Keen public interest in discovering "Earth 2.0" ensures that at least a few stars will be intensively monitored for terrestrial planet signals by the upcoming generation of RV instruments.

Ideally, statistics of terrestrial planet occurrence will emerge from near-future RV surveys. Backing out occurrence rates from these surveys remains highly challenging due to both uneven time sampling and varying activity behaviors across the samples. Great efforts are underway to tackle the activity issue from all sides, and hopefully equal observational coverage in blind planet searches will become standard as the field at large shifts from individual planet detections to recovery of robust statistics.

We wish to emphasize the importance of choosing planet search targets wisely, taking a holistic view of the system and aiming to maximize the information gained by the discovery of new planets. The quantity of time and resources required to detect small planets will necessarily limit the sample of monitored stars. While M dwarfs will certainly be a prime target for finding habitable worlds, Sun-like stars should not be overlooked. In particular, this thesis has laid out a case for the power of solar twins and has identified the most promising targets for future follow-up. The detection of terrestrial planets around these stars will hopefully shed light on the origins of our own world.

REFERENCES

Adibekyan, V., Santos, N. C., Figueira, P., et al. 2015, A&A, 581, L2

Adibekyan, V., Delgado-Mena, E., Figueira, P., et al. 2016, ArXiv e-prints, arXiv:1605.01918

Adibekyan, V. Z., Delgado Mena, E., Sousa, S. G., et al. 2012a, A&A, 547, A36

Adibekyan, V. Z., González Hernández, J. I., Delgado Mena, E., et al. 2014, A&A, 564, L15

Adibekyan, V. Z., Sousa, S. G., Santos, N. C., et al. 2012b, A&A, 545, A32

Aigrain, S., Pont, F., & Zucker, S. 2012, MNRAS, 419, 3147

Amarsi, A. M., Asplund, M., Collet, R., & Leenaarts, J. 2015, MNRAS, 454, L11

Ashwell, J. F., Jeffries, R. D., Smalley, B., et al. 2005, MNRAS, 363, L81

Asplund, M. 2005, ARA&A, 43, 481

Asplund, M., Grevesse, N., Sauval, A. J., Allende Prieto, C., & Blomme, R. 2005, A&A, 431, 693

Asplund, M., Grevesse, N., Sauval, A. J., & Scott, P. 2009, ARA&A, 47, 481

Baliunas, S. L., Donahue, R. A., Soon, W. H., et al. 1995, ApJ, 438, 269

Baranne, A., Mayor, M., & Poncet, J. L. 1979, Vistas in Astronomy, 23, 279

Baumann, P., Ramírez, I., Meléndez, J., Asplund, M., & Lind, K. 2010, A&A, 519, A87

Bazot, M., Ireland, M. J., Huber, D., et al. 2011, A&A, 526, L4

Bedell, M., Meléndez, J., Bean, J. L., et al. 2014, ApJ, 795, 23

—. 2015, A&A, 581, A34

Bedell, M., Bean, J. L., Melendez, J., et al. 2017, ApJ, 839, 94

Bensby, T., Feltzing, S., & Oey, M. S. 2014, A&A, 562, A71

Bernstein, R., Shectman, S. A., Gunnels, S. M., Mochnacki, S., & Athey, A. E. 2003, in Society of Photo-Optical Instrumentation Engineers (SPIE) Conference Series, Vol. 4841, Instrument Design and Performance for Optical/Infrared Ground-based Telescopes, ed. M. Iye & A. F. M. Moorwood, 1694–1704

Binzel, R. P., Bus, S. J., Burbine, T. H., & Sunshine, J. M. 1996, Science, 273, 946

Bodenheimer, P., & Lissauer, J. J. 2014, ApJ, 791, 103

Boisse, I., Bouchy, F., Hébrard, G., et al. 2011, A&A, 528, A4

Bouvier, J. 2008, A&A, 489, L53

Brewer, J. M., & Fischer, D. A. 2016, ApJ, 831, 20

Brewer, J. M., Fischer, D. A., Valenti, J. A., & Piskunov, N. 2016, ApJS, 225, 32

Buchhave, L. A., Latham, D. W., Johansen, A., et al. 2012, Nature, 486, 375

Burbidge, E. M., Burbidge, G. R., Fowler, W. A., & Hoyle, F. 1957, Reviews of Modern Physics, 29, 547

Butler, R. P., Vogt, S. S., Laughlin, G., et al. 2017, AJ, 153, 208

Campante, T. L., Chaplin, W. J., Lund, M. N., et al. 2014, ApJ, 783, 123

Campante, T. L., Schofield, M., Kuszlewicz, J. S., et al. 2016, ApJ, 830, 138

Carlos, M., Nissen, P. E., & Meléndez, J. 2016, A&A, 587, A100

Carter-Bond, J. C., O'Brien, D. P., Delgado Mena, E., et al. 2012, ApJL, 747, L2

Castelli, F., & Kurucz, R. L. 2004, ArXiv Astrophysics e-prints, astro-ph/0405087

Castro, M., Do Nascimento, Jr., J. D., Biazzo, K., Meléndez, J., & de Medeiros, J. R. 2011, A&A, 526, A17

Cayrel, R. 1988, in IAU Symposium, Vol. 132, The Impact of Very High S/N Spectroscopy on Stellar Physics, ed. G. Cayrel de Strobel & M. Spite, 345

Cayrel de Strobel, G. 1996, A&A Rev., 7, 243

Chambers, J. E. 2010, ApJ, 724, 92

Charbonnel, C., & Talon, S. 2005, Science, 309, 2189

Chiang, E., & Laughlin, G. 2013, MNRAS, 431, 3444

Dawson, R. I., & Fabrycky, D. C. 2010, ApJ, 722, 937

De Silva, G. M., Freeman, K. C., Bland-Hawthorn, J., et al. 2015, MNRAS, 449, 2604

Delgado Mena, E., Israelian, G., González Hernández, J. I., et al. 2010, ApJ, 725, 2349

—. 2014, A&A, 562, A92

Demarque, P., Woo, J.-H., Kim, Y.-C., & Yi, S. K. 2004, ApJS, 155, 667

DeMeo, F. E., Binzel, R. P., Slivan, S. M., & Bus, S. J. 2009, Icarus, 202, 160

Denissenkov, P. A. 2010, ApJ, 719, 28

Do Nascimento, Jr., J. D., Castro, M., Meléndez, J., et al. 2009, A&A, 501, 687

Donati, J.-F. 2003, in Astronomical Society of the Pacific Conference Series, Vol. 307, Solar Polarization, ed. J. Trujillo-Bueno & J. Sanchez Almeida, 41

Donati, J.-F., Semel, M., Carter, B. D., Rees, D. E., & Collier Cameron, A. 1997, MNRAS, 291, 658

dos Santos, L. A., Meléndez, J., do Nascimento, J.-D., et al. 2016, A&A, 592, A156 dos Santos, L. A., Meléndez, J., Bedell, M., et al. 2017, MNRAS submitted

Dotter, A., Chaboyer, B., Jevremović, D., et al. 2008, ApJS, 178, 89

Doyle, A. P., Davies, G. R., Smalley, B., Chaplin, W. J., & Elsworth, Y. 2014, MNRAS, 444, 3592

Dressing, C. D., & Charbonneau, D. 2013, ApJ, 767, 95

Dumusque, X., Boisse, I., & Santos, N. C. 2014, ApJ, 796, 132

Dumusque, X., Udry, S., Lovis, C., Santos, N. C., & Monteiro, M. J. P. F. G. 2011a, A&A, 525, A140

Dumusque, X., Lovis, C., Ségransan, D., et al. 2011b, A&A, 535, A55

Dumusque, X., Glenday, A., Phillips, D. F., et al. 2015, ApJL, 814, L21

Dumusque, X., Borsa, F., Damasso, M., et al. 2017, A&A, 598, A133

Duncan, D. K. 1981, ApJ, 248, 651

Epstein, C. R., Johnson, J. a., Dong, S., et al. 2010, The Astrophysical Journal, 709, 447

Figueira, P., Faria, J. P., Delgado-Mena, E., et al. 2014, A&A, 570, A21

Figueira, P., Santos, N. C., Pepe, F., Lovis, C., & Nardetto, N. 2013, A&A, 557, A93

Fischer, D. A., & Valenti, J. 2005, The Astrophysical Journal, 622, 1102

Foreman-Mackey, D. 2016, The Journal of Open Source Software, 24, doi:10.21105/joss.00024

Fossati, L., Ayres, T. R., Haswell, C. A., et al. 2013, ApJL, 766, L20

Freitas, F. C., Meléndez, J., Bedell, M., et al. 2016, A&A submitted

Gaia Collaboration, Brown, A. G. A., Vallenari, A., et al. 2016a, A&A, 595, A2

Gaia Collaboration, Prusti, T., de Bruijne, J. H. J., et al. 2016b, A&A, 595, A1

Gaidos, E. 2015, ApJ, 804, 40

Galarza, J. Y., Meléndez, J., & Cohen, J. G. 2016a, A&A, 589, A65

Galarza, J. Y., Meléndez, J., Ramírez, I., et al. 2016b, A&A, 589, A17

Gelman, A., & Rubin, D. B. 1992, Statistical Science, 7, pp. 457

Ghezzi, L., Cunha, K., Smith, V. V., & de la Reza, R. 2010, ApJ, 724, 154

Gilmore, G., Randich, S., Asplund, M., et al. 2012, The Messenger, 147, 25

Gonzalez, G. 1997, MNRAS, 285, 403

—. 2011, MNRAS, 416, L80

Gonzalez, G., Carlson, M. K., & Tobin, R. W. 2010a, MNRAS, 403, 1368

—. 2010b, MNRAS, 407, 314

González Hernández, J. I., Delgado-Mena, E., Sousa, S. G., et al. 2013, A&A, 552, A6

González Hernández, J. I., Israelian, G., Santos, N. C., et al. 2010, ApJ, 720, 1592

Gray, D. F. 2005, The Observation and Analysis of Stellar Photospheres

Gustafsson, B., Edvardsson, B., Eriksson, K., et al. 2008, A&A, 486, 951

Hall, J. C., Lockwood, G. W., & Skiff, B. A. 2007, AJ, 133, 862

Hands, T. O., Alexander, R. D., & Dehnen, W. 2014, MNRAS, 445, 749

Hardorp, J. 1978, A&A, 63, 383

Haswell, C. A., Fossati, L., Ayres, T., et al. 2012, ApJ, 760, 79

Hinkel, N. R., Young, P. A., Pagano, M. D., et al. 2016, ApJS, 226, 4

Høg, E., Fabricius, C., Makarov, V. V., et al. 2000, A&A, 355, L27

Hogg, D. W., Bovy, J., & Lang, D. 2010, ArXiv e-prints, arXiv:1008.4686

Howe, A. R., & Burrows, A. 2015, ApJ, 808, 150

Ikoma, M., & Hori, Y. 2012, ApJ, 753, 66

Israelian, G., Delgado Mena, E., Santos, N. C., et al. 2009, Nature, 462, 189

Jones, H. R. A., Butler, R. P., Tinney, C. G., et al. 2006, MNRAS, 369, 249

Kass, R. E., & Raftery, A. E. 1995, Journal of the American Statistical Association, 90, 773

Kharchenko, N. V., & Roeser, S. 2009, VizieR Online Data Catalog, 1280

King, J. R., Deliyannis, C. P., Hiltgen, D. D., et al. 1997, AJ, 113, 1871

Kipping, D. M. 2014, MNRAS, 440, 2164

Küppers, M., O'Rourke, L., Bockelée-Morvan, D., et al. 2014, Nature, 505, 525

Lawson, W., Murphy, S., Tinney, C. G., Ireland, M., & Bessell, M. S. 2016, in American Astronomical Society Meeting Abstracts, Vol. 228, American Astronomical Society Meeting Abstracts, 217.08

Lee, E. J., Chiang, E., & Ormel, C. W. 2014, ApJ, 797, 95

Lind, K., Asplund, M., & Barklem, P. S. 2009, A&A, 503, 541

Lind, K., Asplund, M., Barklem, P. S., & Belyaev, A. K. 2011, A&A, 528, A103

Lissauer, J. J., Fabrycky, D. C., Ford, E. B., et al. 2011, Nature, 470, 53

Lissauer, J. J., Jontof-Hutter, D., Rowe, J. F., et al. 2013, ApJ, 770, 131

Liu, F., Yong, D., Asplund, M., et al. 2016, MNRAS, 456, 2636

Lo Curto, G., Lovis, C., Wilken, T., et al. 2010, in Proc. SPIE, Vol. 7735, Ground-based and Airborne Instrumentation for Astronomy III, 77350Z

Lo Curto, G., Pepe, F., Avila, G., et al. 2015, The Messenger, 162, 9

Lodders, K. 2003, ApJ, 591, 1220

Lodders, K., Palme, H., & Gail, H.-P. 2009, Landolt Börnstein, arXiv:0901.1149

Lopez, E. D., Fortney, J. J., & Miller, N. 2012, ApJ, 761, 59

Lovis, C., & Pepe, F. 2007, A&A, 468, 1115

Lovis, C., Dumusque, X., Santos, N. C., et al. 2011, ArXiv e-prints, arXiv:1107.5325

Madhusudhan, N. 2012, ApJ, 758, 36

Mahajan, N., & Wu, Y. 2014, ApJ, 795, 32

Mamajek, E. E. 2009, in American Institute of Physics Conference Series, Vol. 1158, American Institute of Physics Conference Series, ed. T. Usuda, M. Tamura, & M. Ishii, 3–10

Mamajek, E. E., & Hillenbrand, L. A. 2008, ApJ, 687, 1264

Mayor, M., & Queloz, D. 1995, Nature, 378, 355

Mayor, M., Pepe, F., Queloz, D., et al. 2003, The Messenger, 114, 20

Mayor, M., Marmier, M., Lovis, C., et al. 2011, ArXiv e-prints, arXiv:1109.2497

Meléndez, J., Asplund, M., Gustafsson, B., & Yong, D. 2009, ApJL, 704, L66

Meléndez, J., Schirbel, L., Monroe, T. R., et al. 2014a, A&A, 567, L3

Meléndez, J., Bergemann, M., Cohen, J. G., et al. 2012, A&A, 543, A29

Meléndez, J., Ramírez, I., Karakas, A. I., et al. 2014b, ApJ, 791, 14

Meléndez, M., Bautista, M. A., & Badnell, N. R. 2007, A&A, 469, 1203

Meunier, N., Desort, M., & Lagrange, A.-M. 2010, A&A, 512, A39

Meunier, N., & Lagrange, A.-M. 2013, A&A, 551, A101

Migaszewski, C., Słonina, M., & Goździewski, K. 2012, MNRAS, 427, 770

Mills, S. M., Fabrycky, D. C., Migaszewski, C., et al. 2016, Nature, 533, 509

Monroe, T. R., Meléndez, J., Ramírez, I., et al. 2013, ApJL, 774, L32

Montalbán, J., & Rebolo, R. 2002, A&A, 386, 1039

Morton, T. D. 2015, isochrones: Stellar model grid package, Astrophysics Source Code Library, ascl:1503.010

Mulders, G. D., Pascucci, I., & Apai, D. 2015, ApJ, 814, 130

Mulders, G. D., Pascucci, I., Apai, D., Frasca, A., & Molenda-Żakowicz, J. 2016, AJ, 152, 187

Murray, N., & Chaboyer, B. 2002, ApJ, 566, 442

Naef, D., Mayor, M., Lo Curto, G., et al. 2010, A&A, 523, A15

Nissen, P. E. 2015, A&A, 579, A52

Noyes, R. W., Hartmann, L. W., Baliunas, S. L., Duncan, D. K., & Vaughan, A. H. 1984, ApJ, 279, 763

Önehag, A., Gustafsson, B., & Korn, A. 2014, A&A, 562, A102

Önehag, A., Korn, A., Gustafsson, B., Stempels, E., & Vandenberg, D. A. 2011, A&A, 528, A85

Oshagh, M., Santos, N. C., Ehrenreich, D., et al. 2014, A&A, 568, A99

Pál, A. 2012, MNRAS, 420, 1630

Pepe, F., Lovis, C., Ségransan, D., et al. 2011, A&A, 534, A58

Perryman, M., Hartman, J., Bakos, G. Á., & Lindegren, L. 2014, ApJ, 797, 14

Petigura, E. A., Howard, A. W., & Marcy, G. W. 2013, Proceedings of the National Academy of Science, 110, 19273

Petigura, E. A., & Marcy, G. W. 2011, ApJ, 735, 41

Pfalzner, S., Steinhausen, M., & Menten, K. 2014, ApJL, 793, L34

Queloz, D., Henry, G. W., Sivan, J. P., et al. 2001, A&A, 379, 279

Queloz, D., Bouchy, F., Moutou, C., et al. 2009, A&A, 506, 303

Radick, R. R., Lockwood, G. W., Skiff, B. A., & Baliunas, S. L. 1998, ApJS, 118, 239

Ramírez, I., Allende Prieto, C., & Lambert, D. L. 2007, A&A, 465, 271

—. 2013, ApJ, 764, 78

Ramírez, I., Asplund, M., Baumann, P., Meléndez, J., & Bensby, T. 2010, A&A, 521, A33

Ramírez, I., Fish, J. R., Lambert, D. L., & Allende Prieto, C. 2012a, ApJ, 756, 46

Ramírez, I., Meléndez, J., & Asplund, M. 2009, A&A, 508, L17

—. 2014a, A&A, 561, A7

Ramírez, I., Meléndez, J., & Chanamé, J. 2012b, ApJ, 757, 164

Ramírez, I., Meléndez, J., Cornejo, D., Roederer, I. U., & Fish, J. R. 2011, ApJ, 740, 76

Ramírez, I., Meléndez, J., Bean, J., et al. 2014b, A&A, 572, A48

Ramírez, I., Khanal, S., Aleo, P., et al. 2015, ApJ, 808, 13

Reddy, B. E., Lambert, D. L., & Allende Prieto, C. 2006, MNRAS, 367, 1329

Roberge, A., & Kamp, I. 2010, Protoplanetary and Debris Disks, ed. S. Seager, 269–295

Robertson, P., Mahadevan, S., Endl, M., & Roy, A. 2014, Science, 345, 440

Rowe, J. F., Bryson, S. T., Marcy, G. W., et al. 2014, ApJ, 784, 45

Saar, S. H., & Donahue, R. A. 1997, ApJ, 485, 319

Saar, S. H., & Fischer, D. 2000, ApJL, 534, L105

Sandquist, E. L., Dokter, J. J., Lin, D. N. C., & Mardling, R. A. 2002, ApJ, 572, 1012

Schuler, S. C., Cunha, K., Smith, V. V., et al. 2011a, ApJL, 737, L32

Schuler, S. C., Flateau, D., Cunha, K., et al. 2011b, ApJ, 732, 55

Schuler, S. C., Vaz, Z. A., Katime Santrich, O. J., et al. 2015, ApJ, 815, 5

Seager, S., Kuchner, M., Hier-Majumder, C. A., & Militzer, B. 2007, ApJ, 669, 1279

Shi, J. R., Gehren, T., Zeng, J. L., Mashonkina, L., & Zhao, G. 2014, ApJ, 782, 80

Siess, L., Dufour, E., & Forestini, M. 2000, A&A, 358, 593

Silburt, A., Gaidos, E., & Wu, Y. 2015, ApJ, 799, 180

Skumanich, A. 1972, ApJ, 171, 565

Sneden, C. A. 1973, PhD thesis, THE UNIVERSITY OF TEXAS AT AUSTIN.

Sotin, C., Grasset, O., & Mocquet, A. 2007, Icarus, 191, 337

Sousa, S. G., Santos, N. C., Israelian, G., Mayor, M., & Monteiro, M. J. P. F. G. 2007, A&A, 469, 783

Sousa, S. G., Santos, N. C., Israelian, G., Mayor, M., & Udry, S. 2011, A&A, 533, A141

Spina, L., Meléndez, J., Karakas, A. I., et al. 2016a, A&A, 593, A125

Spina, L., Meléndez, J., & Ramírez, I. 2016b, A&A, 585, A152

Spina, L., Palla, F., Randich, S., et al. 2015, A&A, 582, L6

Steinmetz, M., Zwitter, T., Siebert, A., et al. 2006, AJ, 132, 1645

Sullivan, P. W., Winn, J. N., Berta-Thompson, Z. K., et al. 2015, ApJ, 809, 77

Ter Braak, C. J. F. 2006, Stat. Comput., 16, 239

Teske, J. K., Ghezzi, L., Cunha, K., et al. 2015, ApJL, 801, L10

Teske, J. K., Khanal, S., & Ramírez, I. 2016a, ApJ, 819, 19

Teske, J. K., Shectman, S. A., Vogt, S. S., et al. 2016b, AJ, 152, 167

Théado, S., & Vauclair, S. 2012, ApJ, 744, 123

Tognelli, E., Prada Moroni, P. G., & Degl'Innocenti, S. 2016, MNRAS, 460, 3888

Tucci Maia, M., Ramírez, I., Meléndez, J., et al. 2016, A&A, 590, A32

Valenti, J., & Fischer, D. A. 2005, The Astrophysical Journal Supplement Series, 159, 141

Valenti, J. A., & Piskunov, N. 1996, A&AS, 118, 595

van Leeuwen, F., Evans, D. W., De Angeli, F., et al. 2017, A&A, 599, A32

Vogt, S. S., Marcy, G. W., Butler, R. P., & Apps, K. 2000, ApJ, 536, 902

Wang, J., Fischer, D. A., Horch, E. P., & Xie, J.-W. 2015, ApJ, 806, 248

Weiss, L. M., & Marcy, G. W. 2014, ApJL, 783, L6

Wright, J. T. 2005, PASP, 117, 657

—. 2016, ArXiv e-prints, arXiv:1603.08384

Xiong, D. R., & Deng, L. 2009, MNRAS, 395, 2013

Xu, S., Binzel, R. P., Burbine, T. H., & Bus, S. J. 1995, Icarus, 115, 1

Yan, H. L., Shi, J. R., & Zhao, G. 2015, ApJ, 802, 36

Zacharias, N., Finch, C., Girard, T., et al. 2010, AJ, 139, 2184

Zakamska, N. L., Pan, M., & Ford, E. B. 2011, MNRAS, 410, 1895

Zechmeister, M., & Kürster, M. 2009, A&A, 496, 577

Zechmeister, M., Kürster, M., Endl, M., et al. 2013, A&A, 552, A78